Towards gas-phase electron diffraction of novel species

Stuart Young

PhD

University of York

Chemistry

August 2015

Abstract

Novel additions have been made to the York time-averaged electron diffractometer with a view to the study of low volatility and more exotic species. The telefocus electron gun present in the apparatus has been improved and the resulting beam width reduced from 0.76 to 0.40 mm. The existing data collection system was fully tested and eventually replaced with a custom designed camera assembly to improve data quality; this was further improved by the addition of a liquid nitrogen cold trap.

For the study of lower-volatility compounds an air-heated nozzle assembly was built, which, paired with the high intensity of electrons produced from the telefocus gun and almost limitless data acquisition possible using the camera assembly, allows diffraction patterns to be collected from a smaller target density in the sample beam.

Molecular dynamics simulations have been performed using Newton-X to provide vibrational corrections for refinements. These corrections allow a better description for large-amplitude and anharmonic motions, which are badly accounted for using current methods. These will be especially useful for the more complex molecules the apparatus has been designed to study.

To extract and handle the diffraction data collected, custom software has been developed and tested. This software, combined with the improvements and additions to the apparatus, was used to refine the structure of 4-(dimethylamino)benzonitrile.

The combination of these improvements to the apparatus and the custom software, will allow the structure determination of species such as carbon suboxide (C_3O_2), and silyl chloride (SiH_3Cl) dimers.

Contents

List of figures

List of tables

List of accompanying material

The appendices A−D to this thesis contain technical drawings, tables and code pertinent to the work undertaken. The content runs to several hundred pages and is, therefore, presented as a DVD attached to the inside back cover of this book.

Appendix A − Technical drawings of the additions made to the York time-averaged electron diffractometer.

Appendix B − Related computational programs and code.

Appendix C − Models and parameters relating to the gas electron diffraction refinement of $C(SiXMe_2)_4$ (X = H, F, Cl, Br).

Appendix D − Refinement of collected data for benzene and 4-(dimethylamino)benzonitrile (DMABN).

Acknowledgements

I would like to thank the following people, without whom this PhD would not have been as rewarding and enjoyable:

Firstly my supervisor, Dr Derek Wann, for allowing me to undertake this project, and for his patience and guidance throughout the various stages of the project.

The rest of the Wann group: Dr Paul Lane, Dr Matthew Robinson, Pedro Nunes and Conor Rankine for the good advice and stimulating working environment.

For acting as my secondary supervisors in Edinburgh and York, Professor Anita Jones and Dr Martin Cockett, respectively, as well as Dr Carole Morrison and Dr Michał Kochman for their lessons and advice in computational chemistry at the beginning of this PhD.

Discussions with Dr Stuart Hayes of DESY, Hamburg, relating to the York time-averaged electron diffractometer and the EDSTRACT code, were invaluable in gaining an understanding of both the apparatus and the past work carried out on it.

Many custom components have been added to the apparatus and I would like to thank the mechanical, glass-blowing and electronics workshops in both Edinburgh and York for their excellent advice in the design stage, and their work to produce the components described in this thesis.

I thank our collaborator Dr Will Bryan, of Swansea University, for the opportunity to undertake experiments with him at the Central Laser Facility, broadening my knowledge of lasers, and to experience a different research project.

Throughout this PhD, a sustained stream of cake has been provided by the members of the computational cake group and room 203 in Edinburgh, and office A057 in York. Many thanks for this.

I would also like to thank the University of Edinburgh, University of York,

And finally, to my Mum for her willingness to listen to me talk about this project, whilst having no interest in it at all.

Declaration

The research contained within this thesis was carried out between September 2011 and August 2013 at the University of Edinburgh, and between September 2013 and August 2015 in the Department of Chemistry at the University of York.

Except where reference is made to other work, this research is original and my own.

Work carried out during my PhD has led to the publication of one article, published in a peer reviewed journal.

Publication:

Structures of Tetrasilylmethane Derivatives C(SiXMe$_2$)$_4$ (X = H, F, Cl, Br) in the Gas Phase and their Dynamic Structures in Solution - D. A. Wann, S. Young, K. Bätz, S. L. Masters, A. G. Avent, D. W. H. Rankin and P. D. Lickiss, *Z. Naturforsch. B*, 2014, **69**, 1321-1332, DOI: 10.5560/ZNB.2014-4147

Chapter 1

Introduction

1.1 Motivation for performing electron diffraction experiments

Diffraction studies allow precise, direct observations of chemical structures to be made, facilitating greater understanding of links between experimental results and the molecular architectures responsible for them. Diffraction is, therefore, of paramount importance in many areas of chemistry. For example, X-ray diffraction is routinely used to characterise the structures of crystalline solids, giving insights into novel properties such as single-molecule magnetism.[1]

X-rays, however, are a relatively inefficient probe of gas-phase structure due to the low target density in a gaseous sample and the prohibitively high flux of X-rays consequently required to observe diffraction. Electrons serve as a far better diffraction probe for gas-phase samples: the high collision cross sections of electrons relative to X-rays make diffraction more easily acquirable, while their negative charges are scattered by nuclei rather than electron density as is the case for X-rays.[2] Electron diffraction can yield atomic positions with a high degree of precision, independent of the electronic environment of the molecule. Such gas-phase experimental structures are closely comparable to calculated isolated molecule structures, as the distances between gaseous molecules allows the assumption to be made of isolation from intermolecular forces.

Chemistry has always been driven forward through experimentation, with many syntheses being perfected by multiple trial and error experiments. In recent years, however, theoretical calculations have become a powerful tool, not only helping chemists to optimise their experiments, when experimental data are unclear or ambiguous, but also leading researchers towards more likely or profitable synthetic routes. This is only possible if the calculations used are accurate and realistic, which requires benchmarking with experimentally observed structural data.

Continued development of the electron diffraction technique is required to

increase the variety of species that can be studied and, therefore, maintain the significance of the discipline. To this end, improvements have been made to the Gas Electron Diffraction (GED) apparatus in York as part of this PhD: improved focussing of the electron gun has been achieved leading to better spatial resolution; the choice of inlet system has been extended to include a heated nozzle assembly paired with a cold trap; a new camera assembly has been built; and novel extraction code has been written to allow data collected using this detector to be manipulated for use in GED refinements.

1.1.1   History of GED

Thomas Young's double-slit experiments, performed in the early nineteenth century, used two parallel slits to diffract coherent light.[3] Following diffraction, the wave-like behaviour of the light leads to an interference pattern which can be used to determine both the distance between, and the widths of, the slits. This is the basis for all diffraction experiments, with the diffracting medium acting like a series of slits producing interference patterns from the incoming waves.

In the early 1920s quantum theory described the basis of wave-particle duality,[4] demonstrating that electrons could behave both as particles and as waves. Diffracted electrons could, therefore, produce interference patterns just as the light had done in Young's experiments. Combined with the negative charges of the electrons, which interact with charge gradients at the edges of nuclei; this makes electrons a perfect diffraction probe for molecules. Diffraction occurs most strongly when the probe wavelength is comparable to the width of the 'slit'. Each of the atoms in a molecule acts as a slit, with each slit separated from the next by some few Ångstrøms.

De Broglie related the wavelength, λ, to the momentum of an object, as shown in Equation 1.1:[4]

$$\lambda = \frac{h}{mv} \quad , \tag{1.1}$$

where h is the Planck constant and mv is the momentum of the electron.

Davisson and Germer, in the late 1920s,[5] confirmed that diffraction of electrons was possible by obtaining scattering patterns from crystalline solids that agreed with Bragg's laws of diffraction.[6] Work by Debye, ten years earlier, to show that X-rays could be diffracted using a gaseous sample,[7] combined with the proof that electrons could be used as a diffraction probe led to the work of Mark and Wierl,[8] who collected the first gas electron diffraction patterns soon after the seminal work of Davisson and Germer.

Figure 1.1 shows a diffraction pattern recorded during an experiment carried out using the former Edinburgh time-averaged GED apparatus, which is now in the University of Canterbury, Christchurch, New Zealand.[9] The concentric rings observed represent variations in intensity caused by constructive and destructive interference of diffracted electrons, which have been made more uniform in intensity through the use of a rotating sector (more details are given later). In the early days of GED, data were interpreted using a visual estimation of those raw intensities and ring spacing within the interference patterns. Unfortunately, in these early experiments performed without a rotating sector, the intensities in the diffraction pattern decreased sharply with distance from the centre of the pattern.[2] Moreover, the perception of intensity by the human eye is not consistent, often correcting for the reduction in intensity of the pattern, leading to inaccurate structures. Pauling and Brockway proposed measuring the optical density of the photographic plate using a photometer to eliminate this problem.[10] Unfortunately, the quality of the data at the time was insufficient for the photometer method and so a visual interpretation of intensities persisted.
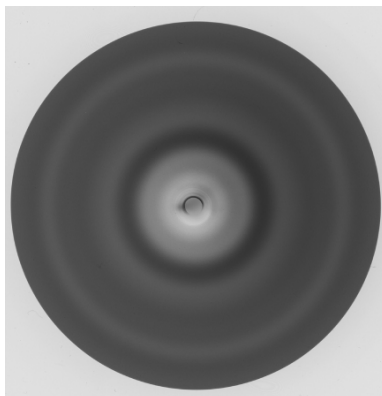
Figure 1.1 – Scanned photographic film, showing the GED diffraction pattern of benzene. This image was collected using the former Edinburgh GED apparatus that is now in New Zealand.

To reduce the impact of the sharply falling intensity and to acquire higher quality data at wider scattering angles, a rotating sector (Figure 1.2)[11] was independently suggested by Finbak[12] and Debye.[13] A shaped metal disk is spun in front of the photographic plate to alter exposure to electrons relative to the distance from the centre of the pattern. In the 1950s the combination of the rotating sector and an improved method for the use of a photometer, known as the sector-photometer method, became commonplace.[14, 15] Figure 1.1 is an example of a pattern obtained using a rotating sector. Peaks and troughs in intensity can be observed to wider scattering angles than would have been the case without a sector.
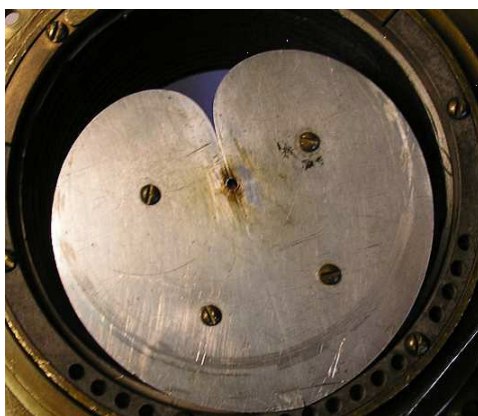
Figure 1.2 – Image of the rotating sector from the former Edinburgh GED apparatus that is now in New Zealand.[11]

GED often employs well-established and well-understood detection media such as image plates[16] or photographic film.[17] This is due to their high dynamic ranges and reproducibility, allowing high-quality data to be recorded. Unfortunately, the number of images that can be acquired using these media is limited as they must be present within the vacuum and breaking the vacuum to replace the photographic media is time-consuming.

It is worth noting at this point that two distinct branches exist in GED: time-averaged electron diffraction, in which a continuous electron beam is used to acquire data over a relatively long time period, and time-resolved electron diffraction, which uses pulses of electrons to study dynamics of molecules through observation of structural changes over very short periods of time. The two techniques can be understood using a photographic analogy. Time-averaged ED yields results that are analogous to a camera with a slow shutter speed, leading to a long exposure time, while time-resolved ED, is more like taking a snapshot. Figure 1.3 shows two images of a dynamic subject; the time-averaged image [Figure 1.3(a)] is blurred as it comprises all of the motion over the exposure time. The time-resolved image [Figure 1.3(b)] is well resolved as the short exposure time collects a near instantaneous image. The two techniques, and some apparatus associated with them, are outlined further in Sections 2.2.1 and 2.2.2, respectively.
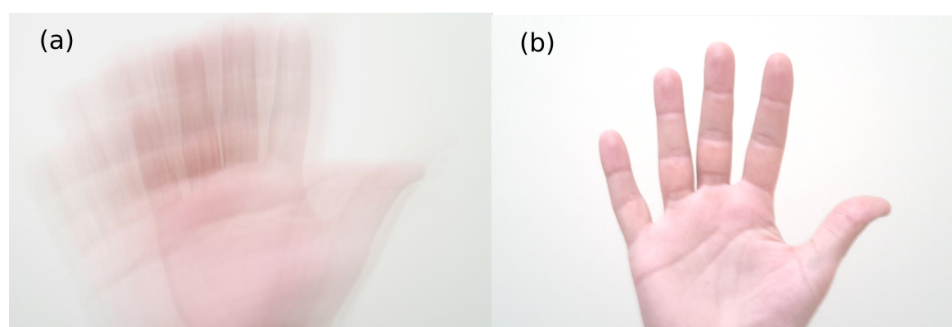
Figure 1.3 – Images of a moving hand depicting (a) a long exposure time and (b) a short exposure time.

Developments in modern electron diffraction, such as those described in this thesis, aim to extend the reach of the time-averaged technique to a wider range

of samples or to move towards the use of electrons as a time-resolved probe to view directly atomic movement during a chemical process. In order to obtain high-quality data to validate these techniques, multiple diffraction images are often required to improve the signal-to-noise ratio. The traditional photographic media cannot easily be used in this way, as they must be removed from the vacuum to be developed. A limited number of images can be recorded during each experiment, and the quality of those images can only be checked after the experiment has been finished. In the 1980s a new data collection method was pioneered by Ewbank *et al.*,[18] utilising a photodiode array paired with a phosphor screen; images could then be viewed almost instantly on a computer. Charge-coupled device (CCD) detectors have since replaced photodiodes in GED applications as the the higher charge-to-voltage conversion makes CCD detectors more suitable for low-light-level detection,[19] acting just like a digital camera, offering almost limitless data acquisition without the need to break vacuum and allowing instant checking of data quality. A CCD, like the photodiode, can only detect electromagnetic radiation, and so cannot detect the electrons directly. Instead, a phosphor screen scintillates when an incident electron strikes it producing light which is subsequently detected.

Advances have not only been made in the hardware for electron diffraction but also in the theory of refinement of structures. Early experiments compared a number of theoretical intensity curves (explained further in Section 1.2.2) against the extracted data, with the closest fit revealing the final structure.[2] Realistically, limited numbers of theoretical structures can be compared, and a subjective choice of the best fit introduces the potential for inaccuracy into the structure determination.

The advent of digital computing allowed more sophisticated fitting procedures to be undertaken. Initially computers were only used to calculate molecular-intensity and radial-distribution curves;[20, 21] however, from the late 1950s computers were used to perform least-squares refinements.[22, 23] Generally a computational model of the molecule of interest is constructed using a

number of geometric parameters (*e.g.* bond lengths and angles) to describe the three-dimensional structure of the molecule. These parameters are then varied during the refinement process to achieve the best fit to the experimental data, removing the subjective choice of theoretical curve and eliminating the reliance on the visual quality of the fit. The refinement process, with examples, is explained more fully in Section 1.2.2.

Increases in computational power available to research groups have led to more accessible, reliable *ab initio* structures (explained further in Section 1.3). These calculated structures were used in conjunction with GED data in the molecular orbital constrained electron diffraction (MOCED) method,[24] in which structural features poorly described by GED (*e.g.* light atoms) were instead fixed to calculated values. Including these 'supplementary data' from theory allowed larger, more complicated structures to be refined. However, fixing structural parameters within a refinement does not allow variation in the value, so if that value is incorrect, the structure obtained from the refinement will also be incorrect. This was one of the problems with the MOCED approach; another was that any refined structural parameters that are strongly correlated to the fixed parameter will have artificially small associated uncertainties. This is due to the implicit 'correctness' of the calculated structure, which has an error of zero.[25]

SARACEN (Structural Analysis Restrained by *ab initio* Calculations for Electron diffractioN)[25] improves upon both of the problems associated with the MOCED method. In SARACEN a series of calculations are performed using different methods and basis sets, explained in Section 1.3. The variation in a given structural parameter between calculations is then used as an approximate error. During the refinement that parameter is then constrained using this error value allowing a refined parameter, realistic error and reliable structure to be obtained. Further information on the methods used to overcome the limited data available from GED is given in Section 1.2.3.

1.2 GED theory

All gas electron diffractometers require three main components: a source of well-collimated electrons, an inlet system for the introduction of samples, and a detector to image the interference patterns of the diffracted electrons. It is commonly these components, which tend to be custom-made due to the specialist nature of the discipline, that dictate the experiments that can be undertaken. A simple diagram of these components forming a GED set-up is shown in Figure 1.4.
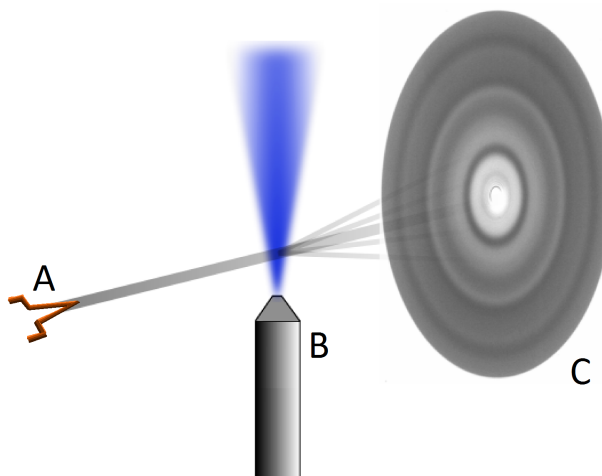
Figure 1.4 – Schematic diagram showing a basic gas electron diffraction set-up. The tungsten filament (A) produces a continuous electron beam, intersecting a jet of gas from the effusive nozzle (B). The scattered electrons form a diffraction pattern recorded at the detector (C).

1.2.1 Diffraction of electrons

The incident beam consists of a number of electrons travelling with the same velocity, with each incident electron travelling on trajectory, $\mathbf{k}_0$. The charge gradients at the edges of the atomic nuclei act like the slits in Young's experiments, elastically scattering the electrons. After the scattering event the

trajectory of a given electron is termed $\mathbf{k}$. The vector describing the change in trajectory, $\mathbf{s}$, is dependent upon the scattering angle, θ, and has magnitude, s. The three vectors are shown schematically in Figure 1.5. The scattering event is assumed to be elastic, with the magnitude (k) of vectors $\mathbf{k}$ and $\mathbf{k}_0$ equal to $\frac{2\pi}{\lambda}$. The formula for the magnitude, s, of scattering vector, $\mathbf{s}$, is given in Equation 1.2:

$$ s = \frac{4\pi \sin(\frac{\theta}{2})}{\lambda} \quad . \tag{1.2} $$

The pattern obtained from Young's experiment provided information on the distances between the slits, and the same is true of the GED experiment, with the diffraction pattern giving information on the interatomic distances in the molecule.
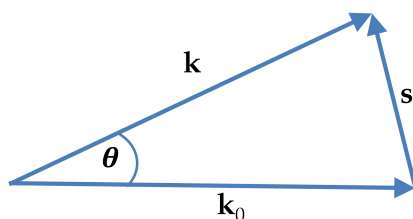
Figure 1.5 – Schematic depiction of the scattering vector, $\mathbf{s}$. The incoming electron is described by wavevector $\mathbf{k}_0$, while the scattered electron is described by wavevector $\mathbf{k}$.

1.2.2 From data collection to structure determination

In this section, both the theory and procedure for determining the molecular structure from the diffraction patterns will be discussed. All examples have been taken from the structure determination of the bromine-containing tetrasilylmethane derivative $C(SiBrMe_2)_4$ (Figure 1.6), performed during the first year of my PhD.[26] The scientific paper relating to the GED studies of this and other related derivatives can be found in the associated publications section of this thesis.
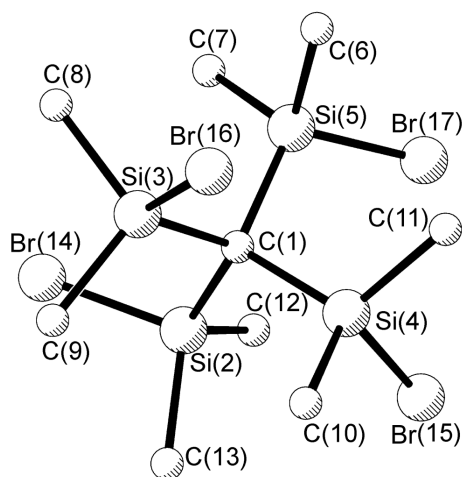
Figure 1.6 – Representation of the general structure of $C(SiBrMe_2)_4$ with atom numbering. Hydrogen atoms have been removed for clarity.

Concentric rings are seen in GED diffraction patterns because molecules in the gas phase are present in all possible orientations. As the image is circular, the data in all directions from the centre of the image to the edge are equivalent, so the intensities are averaged around the image to produce the final experimental intensity curve.

The image acquired at the detector represents a combination of all diffraction that has occurred. Interference of diffracted electrons gives information that is useful for structure determination, but atoms can also scatter electrons that do not interfere. No information about the structure of the molecule can be obtained from these scattering events and so their removal from the pattern is necessary. Atomic scattering is, fortunately, well understood and predictable.[2]

Each pair of atoms, if isolated, would lead to an intensity curve that is roughly sinusoidal in form, with a series of peaks and troughs. The superposition of these curves for every pair of atoms in the molecule produces the intensity pattern observed after atomic scattering is removed. Atoms with larger nuclei have larger scattering cross sections and, as a result, will scatter electrons more strongly. The sine curves related to scattering from distances to these heavier atoms will

contribute a greater proportion of the total intensities collected.[2]

The magnitude of the scattering vector, s, can be expressed as in Equation 1.3; this is the same variable used in Equation 1.2 though the scattering angle, θ, is now expressed in terms of the following apparatus-specific experimental variables:[27] the wavelength of the incident electrons, λ, the nozzle-to-camera distance, r_{cam}, and the distance from the centre of the pattern, r. This is very important as, due to the nature of the discipline, most diffractometers are custom-made creating a wide variety in the variables present in Equation 1.3:

$$s = \frac{4\pi}{\lambda} \sin\left[\frac{1}{2}\tan^{-1}\left(\frac{r}{r_{cam}}\right)\right] \quad . \tag{1.3}$$

The wavelength of electrons used is related to the s value obtained for each data point as described in Equation 1.3. Precise knowledge of the wavelength is, therefore, vitally important. But Equation 1.1 fails to describe electrons that approach the speed of light, which will occur when using large accelerating potentials. The mass of the electron will increase markedly when approaching the speed of light, requiring a relativistic description. The rest mass of an electron, m_e, is related to the wavelength, λ, by the accelerating potential, V, as shown in Equation 1.4:

$$\lambda = \frac{h}{\sqrt{2m_e Ve\left(1 + \frac{Ve}{2m_e c^2}\right)}} \quad . \tag{1.4}$$

Some typical diffraction patterns are shown in Figure 1.7. The one-dimensional data, extracted from the centre to the edge of the diffraction pattern, are represented as a graph of s against the intensity of scattered electrons detected. This is referred to as a molecular intensity curve (MIC), with an example shown in Figure 1.8.
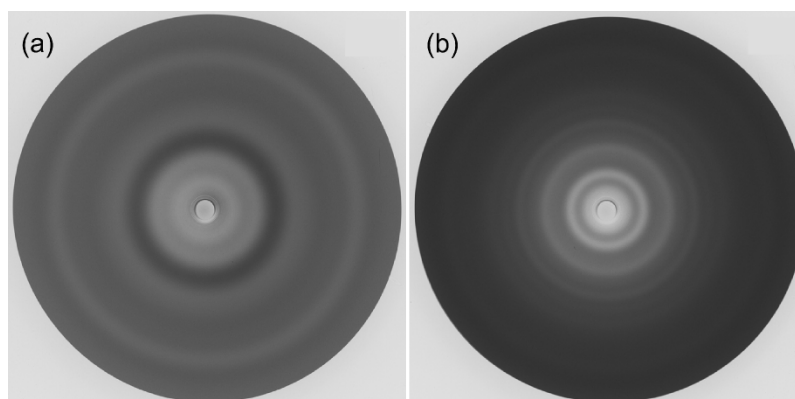
Figure 1.7 – Scanned photographic films collected for $C(SiBrMe_2)_4$ at (a) a long and (b) a short nozzle-to-camera distance.
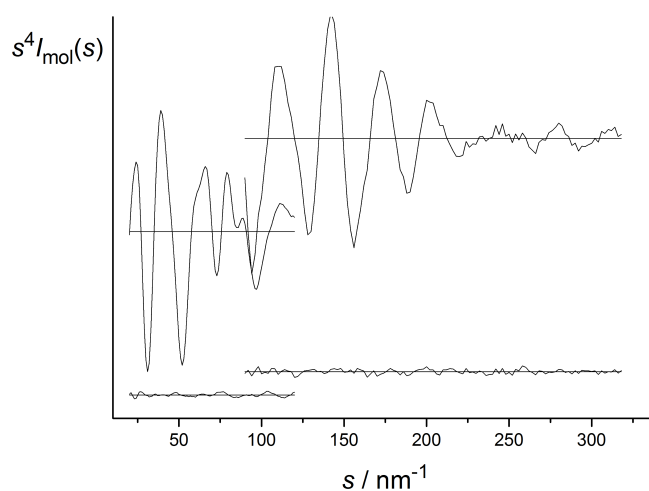
Figure 1.8 – Experimental and difference (experimental-minus-theoretical), molecular intensity curves for $C(SiBrMe_2)_4$. The upper curve is collected at a short nozzle-to-camera distance, while the lower curve is collected at a long nozzle-to-camera distance.

To maximise the data collected, images are recorded at different nozzle-to-camera distances, which allows a larger s range to be sampled. The MICs for different nozzle-to-camera distances overlap, allowing data quality to be checked. Non-matching peaks within the MIC can be identified and poor quality data near the edge of the pattern removed. Short nozzle-to-camera distances (approximately 90 mm for 40 kV) provide data to wider scattering angles (larger s values), while longer nozzle-to-camera distances (approximately 250 mm for 40 kV) sample the lower end of the s range. Figure 1.7 shows experimentally collected diffraction patterns for $C(SiBrMe_2)_4$ at two separate nozzle-to-camera distances.

Theoretical curves, against which the experimental data are compared, are constructed using the scattering equations. The original 'Wierl equation' (Equation 1.5) illustrates the relationship between the intensities and the bond distances, r_{ij},[8] which can be rewritten in terms of the scattering function for each atom, F_i (Equation 1.7), shown in Equation 1.6.[28] The scattering function is defined as the atomic number, Z_i, minus the X-ray scattering factor, f_i.

$$I(s)_{apparent} \approx \frac{I(s)_{molecular}}{I(s)_{atomic}} \approx \sum_{i}^{N} \sum_{i \neq j}^{N} Z_i Z_j \frac{\sin s r_{ij}}{s r_{ij}} \tag{1.5}$$

$$I(s) = \sum_{i}^{N} \sum_{j}^{N} F_i(s) F_j(s) \frac{\sin s r_{ij}}{s r_{ij}} \tag{1.6}$$

$$F_i(s) = \frac{2(Z_i - f_i)}{a_0 s^2} \tag{1.7}$$

The Wierl equation is useful as it allows the scattering equation to be written in terms of s. For the purposes of any GED experiments carried out in this work, and as is the case in the Wierl equation, only two-atom scattering is considered. The probability of three-atom and higher-order scattering events occurring for a

given electron is sufficiently small that they need not be considered in most cases. Only in special cases, such as molecules containing both right angles between bonds, and containing heavy atoms, does multiple scattering need to be taken into account.[29]

As experimental data collection was improved with the sector-photometer method,[14,15] it became clear that the Wierl equation was insufficient to fully describe the electron diffraction experiment.[30] The assumption within Equation 1.5 is of a static distance between the atoms equal to r. Vibrations in the molecule fluctuate the interatomic distance requiring a probability function be introduced to describe the probability, $P_{ij}(r)$, of the interatomic distance being equal to r. A harmonic assumption of bond vibrations produces a Gaussian distribution in $P_{ij}(r)$, using either a quantum-mechanical ground-state wavefunction or a classical Boltzmann population. Simplifying Equation 1.8 to Equation 1.9 allows the intensities to be written in terms of the root-mean-squared amplitudes of vibration, u_{ij}:[30]

$$I(s) = \sum_i \sum_j F_i(s)F_j(s) \int P_{ij}(r)\frac{\sin sr_{ij}}{sr_{ij}} \quad , \tag{1.8}$$

$$I(s) = \sum_i^N \sum_j^N F_i(s)F_j(s) \exp\left(-u_{ij}^2\frac{s^2}{2}\right)\frac{\sin sr_{ij}}{sr_{ij}} \quad . \tag{1.9}$$

Exceptions have been found that required a further improvement to the scattering equation. Refinement of data collected for UF_6 using Equation 1.9 incorrectly proposes two separate $U-F$ distances. The vast difference in nuclear charge between fluorine and uranium atoms in UF_6 causes a breakdown in the Born approximation, contracting the wavelength of the electron as it approaches the heavy atom and causing a shift in the electronic wavefunction.[31] This shift is taken into account in Equation 1.10, where η_i is the phase shift from atom i:

$$I(s) = \sum_i^N \sum_j^N |F_i(s)||F_j(s)| \cos\left(\eta_i - \eta_j\right) \exp\left(-u_{ij}^2 \frac{s^2}{2}\right) \frac{\sin sr_{ij}}{sr_{ij}} \quad . \tag{1.10}$$

Equation 1.10 produces theoretical intensity curves for most diffraction experiments very well, although it is based on the assumption of harmonicity in intermolecular vibration. In reality, interatomic bonded distances exhibit a more anharmonic vibration. A ground-state Morse oscillator, shown alongside a harmonic curve in Figure 1.9, used as the basis of the $\int P_{ij}$ values, alters the probability, as shown in Equation 1.11, allowing the anharmonicity of a bond vibration to be taken into account:[32]

$$\int P_{ij} \frac{\sin sr}{sr} dr \approx \exp\left(-u_{ij}^2 \frac{s^2}{2}\right) \frac{\sin\left[s\left(r_{ij} - \kappa_{ij}s^2\right)\right]}{sr_{ij}} \quad , \tag{1.11}$$

where

$$\kappa_{ij} \approx \frac{au_{ij}^4}{6} \quad . \tag{1.12}$$
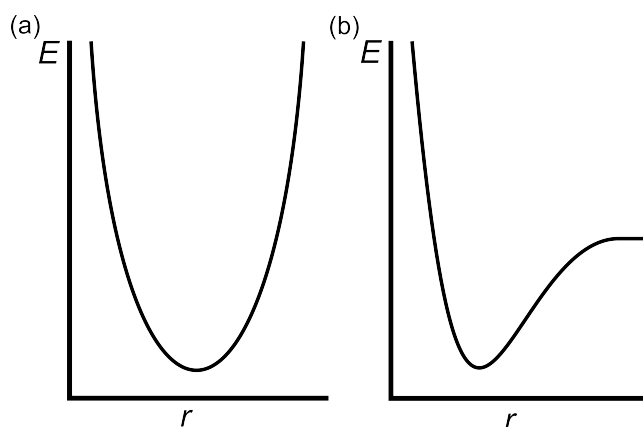
Figure 1.9 – Diagrammatic representation of potential energy curves for (a) a harmonic oscillator and (b) a Morse potential.

The asymmetry coefficient in Equation 1.12, a, is often replaced using a tabulated value; for non-bonded distances the probability is assumed to be harmonic ($a = 0$), and to be approximately 20 nm^{-1} for bonded distances.

Other assumptions made in the treatment of data include: that there is a single point of interaction between the sample beam and incident electrons, that all molecules within the beam are at the same temperature, and that the beam is considered a point, rather than the approximately 0.5 mm full width at half maximum (FWHM) value, which it has in reality. If the beam was excessively wide it would lead to broadening of peaks and a reduction in the spatial resolution of the experiment.[28]

Although experiments are carried out in high-vacuum conditions (pressures of 10^{-5} mbar or lower), gas molecules still exist in the vacuum chamber and can scatter the beam, forming part of the background that is subtracted from the collected data. This background consists not only of this extraneous scattering, but also any light produced from the filament, as often the detector is photosensitive.

Background patterns collected using the same beam intensity and duration as the experiment are, therefore, subtracted from the data, as well as a correction for any sector or filter used. The data now are a combination of the atomic and molecular scattering. As mentioned previously, the molecular scattering is the only information of interest, and therefore the atomic scattering is removed before further analysis of the data.

1.2.2.1 Radial distribution curve

A Fourier transform of the MIC, from s to r, yields the radial distribution curve (RDC), introduced by Pauling and Brockway in 1934.[10] At that time, the data quality was poor, leading to its use only as an indicator of starting geometry for further refinement. As data quality improved, and alongside improvements in the scattering equations, the RDC served as a useful visual interpretative tool.

If the molecules were static, the transform of the MIC would yield a series of sharp peaks, with each maximum representing an interatomic distance. Due to the time-averaged nature of all diffraction experiments, molecular vibrations over the course of the acquisition period vary the distances. As a result the output is a number of broader peaks, yielding information about amplitudes of vibration for pairs of atoms. The RDC serves as a visual tool, not only to allow understanding of the MIC more easily, but also to show quickly which distances in the molecule are poorly described when comparing the experimental and theoretical curves.[2]
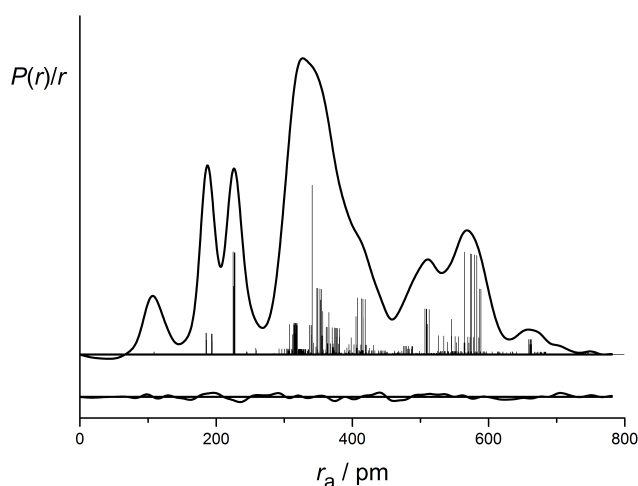
Figure 1.10 – Experimental and difference (experimental-minus-theoretical) radial distribution curves, $P(r)/r$, from the GED refinement of $C(SiBrMe_2)_4$. Before Fourier inversion, data were multiplied by $s \exp \left(\frac{-0.00002s^2}{(Z_C - f_C)(Z_{Br} - f_{Br})} \right)$.

The experimental MIC exists over a finite range of approximately 30 to 250 nm^{-1} for both the apparatus formerly in Edinburgh and the apparatus in York. This creates a problem in the Fourier transform which assumes a wave starting at $s = 0$ nm^{-1} and extending infinitely. For the purposes of this work the MIC is, therefore, supplemented by a dampening equation at s values below and above the limits of the experiment, allowing a Fourier transform to be performed. An example of the equation used to calculate the Fourier transform is shown in Equation 1.13:

$$\frac{P(r)}{r} = A \int_0^\infty \frac{sI_{\mathrm{mol}}(s)}{|F(s)|^2} sin(sr)ds \quad , \tag{1.13}$$

where A is a scaling constant, and $F(s)$ the weighted scattering factor.[33] The weighted scattering factor used for all refinements in this work is the combination of scattering factors from the two most significant scatterers in the molecule. For the refinement of $C(SiBrMe_2)_4$, those two atoms are carbon and bromine. This choice does not affect the refinement of the structure, but changes the appearance of the radial distribution curve.

The desired structure obtained from GED, or any other structural technique, is the lowest energy structure, referred to as the equilibrium structure (r_e). Data from time-averaged GED experiments give average positions of the atoms during the experiment (r_a). Unfortunately, due to the vibrations of the molecule these distances are not equivalent and the correction to achieve r_e from r_a cannot be known exactly; only approximations to bring the refined structure as close as possible to r_e can be made. Correcting this structure, to produce a good approximation of the equilibrium form, requires vibrational corrections to be applied; these are described further in Section 1.4.

The computational model mentioned earlier is written in Fortran, and refined using customised software called ed@ed.[34] Each parameter in the model, written for the molecule of interest, is refined against the experimental data, in a stepwise manner, until the best fit is achieved. The amplitudes of vibration for pairs of atoms within the molecule can also be refined.

1.2.3 Complementary data and the SARACEN method

GED structure determination is, as we have already seen, limited by the amount of data acquirable from the 1-D diffraction patterns yielded by experiment. More complex, and less symmetric, molecules often require supplementary data to be utilised to allow the structure to be fully refined. As the vibrations

of the atoms during the refinement broaden the peaks seen in the RDC, similar distances are found under the same peak and cannot all be individually refined. To obtain the most accurate structure with the data available, a series of simultaneous equations is employed. For example, in the refinement of $C(SiBrMe_2)_4$ (see Figure 1.6 for atom numbering), the central carbon-to-silicon bonded distance, $C(1)-Si(2)$ (A) ≈ 191 pm, and silicon-to-methyl-carbon bonded distance, $Si(2)-C(12)$ (B) ≈ 186 pm are of a similar magnitude, and are found under the same peak in the RDC (see Figure 1.10). The weighted average based on the number of each type of distance, and the difference between the distances was used to describe A and B in terms of two parameters; Equation 1.14 shows the weighted average (p_1) and difference (p_2):

$$p_1 \approx \frac{2B}{3} + \frac{A}{3} \qquad p_2 = B - A \quad . \tag{1.14}$$

Distances A and B are then reconstructed as:

$$A = p_1 - \frac{2(p_2)}{3} \quad \text{and} \quad B = p_1 + \frac{p_2}{3} \quad , \tag{1.15}$$

respectively.

As mentioned in Section 1.1.1 *ab initio* calculations can be used as a source of extra data. Optimised structures give a good estimate of the likely true structure and can be used as a basis for the design of the refinement model. In addition to this, the SARACEN (Structural Analysis Restrained by *ab initio* Calculations for Electron diffractioN) method,[25] briefly described in Section 1.1.1, can be used.

For the parameters in Equation 1.14 used in the example refinement, the average value (p_1) refines well from experimental data alone, while the difference parameter (p_2) requires a SARACEN restraint to be imposed, to prevent an unrealistic value being found.

Various sources of experimental data can also be included in GED structure refinements. Previous examples have involved the use of data from X-ray crystallography,[35] liquid-crystal NMR,[36] or rotational spectroscopy.[37] The combination of experimental electron diffraction data with data from other experimental techniques is known as the STRADIVARIUS (STructure Analysis using DIffraction and VARIoUS other data) method.[37]

Although useful for some classes of compounds, there are some problems with the use of experimental data from other experiments. Rotational spectroscopy, or microwave spectroscopy as it is sometimes known, can provide accurate molecular structures for simple molecules. However, it only provides information relating to three moments of inertia, restricting the ability to extract detailed structural data without resorting to systematic isotopic substitution; this can be laborious, as well as synthetically complicated. Meanwhile, X-ray diffraction yields positions of high electron density and so cannot be directly compared to electron diffraction, although it can often be of use after refinement as a comparison of the differences between gas-phase and crystalline structures.

1.3 *Ab initio* quantum theory

The complementary relationship between calculated molecular properties and experiment is increasingly important as the quality of calculated values improves. This is only possible through the continued work on improving theory, improvement of facilities to carry out calculations, and the continual benchmarking of basis sets and theory against experimental data. The latter is of great importance as it validates calculations and informs choices when studying related compounds or structural features. GED, along with other gas-phase techniques, provides reliable structures, against which calculations can be compared, and is often used for such benchmarking.

The theory pertaining to the evaluation and understanding of *ab initio*

calculations is briefly outlined in this section.

1.3.1 The Schrödinger equation

The derivation of molecular properties from first principles is the goal of *ab initio* calculations, and this is done by solving the time-independent Schrödinger equation (SE), shown in Equation 1.16:[38]

$$\hat{H}\Psi = E\Psi \quad , \tag{1.16}$$

where E is the energy of the molecule, $\hat{H}$ is the Hamiltonian operator, and Ψ is the wavefunction, which describes the quantum state of the molecule. The entire molecule is represented by this single wavefunction. The solution of this equation provides the molecular properties of interest.

Five separate terms comprise the operator: both the kinetic energies of the nuclei ($\hat{T}_n$) and the electrons ($\hat{T}_e$) within the molecule, the potential energy of the electronic repulsion ($\hat{V}_{ee}$), nuclear repulsion ($\hat{V}_{nn}$) and the nuclear-electronic attraction ($\hat{V}_{ne}$). This is shown in Equation 1.17:

$$\hat{H} = \hat{T}_e + \hat{T}_n + \hat{V}_{ne} + \hat{V}_{nn} + \hat{V}_{ee} \quad . \tag{1.17}$$

To solve this, for all but single electron systems, is impossible, requiring approximations to be employed. The Born-Oppenheimer approximation states that due to the difference in mass between nuclei and electrons, nuclei can be considered stationary with respect to the electrons. The stationary nuclei therefore have a kinetic energy of zero, and a constant potential energy between the nuclei. The components of the resulting Hamiltonian operator are shown in Equation 1.18.

$$\hat{H}_{el} = \hat{T}_e + \hat{V}_{ne} + \hat{V}_{nn} + \hat{V}_{ee} \quad , \tag{1.18}$$

After invoking the Born-Oppenheimer approximation, the system can still only be solved for one-electron systems as the increase in complexity upon addition of interelectronic effects does not allow an exact solution to be found. For it to be possible to solve an approximation for multi-electron systems, it is assumed that the electrons are independent of each other, allowing the combination of one-electronic wavefunctions to create the full electronic wavefunction (Equation 1.19).[39]

$$\Psi(r_1, r_2, r_3, \ldots, r_N) = \psi(r_1)\psi(r_2)\psi(r_3)\ldots\psi(r_N) = \prod_{i=1}^{N} \Psi_N(r_i) \quad . \tag{1.19}$$

The electrons do however interact, and failure to incorporate this into calculations leads to vastly incorrect energies. Hartree-Fock theory is one method used to account for this.

1.3.2 Hartree-Fock self-consistent field theory

The approximation central to Hartree-Fock theory (HF) is that the electrons exist within an average electric field, with each electron feeling the effect of $(n-1)$ electrons (n = number of electrons), allowing the SE for each electron to be solved individually for the stationary nuclei.[39]

An approximate guess at the form of the wavefunction is computed and the result is the input for the next calculation. This progresses iteratively until the result of the calculation is sufficiently similar to the input wavefunction, at this point the calculation is converged. Once this occurs the electrons are referred to as self-consistent, leading to the alternative name for Hartree Fock: self-consistent field theory. The nuclei are then moved and the calculations repeated; this process

is continued until a potential minimum is found. One advantage of HF theory is that it accounts exactly for the electron-exchange energy, which is caused by the change in sign of the wavefunction of the electron when it is exchanged; this change in sign is due to the fermionic properties of the electron. HF theory utilises a Slater determinant to obtain this exactly.

HF theory can produce energy values to within about 1% of experimental values, although this missing 1% is of vital importance. This lack of accuracy is due to electronic interactions, which are not sufficiently described using a static field. This is called electron correlation and becomes more pronounced within areas of high electron density, where repulsion is far greater than is accounted for in HF. A number of methods for obtaining structures and energies closer to the true values exist, often referred to as post-HF methods. Coupled Cluster (CC) theory, Complete Active Space Self-Consistent Field (CASSCF) theory,[40] and Møller Plesset (MP) perturbation theory[41] are examples of these. Only MP is discussed here as that is the theory utilised in this work.

1.3.3 Møller-Plesset perturbation theory

The work of Møller and Plesset proposed that HF was a zero-order approximation of the exact solution, with an infinite number of terms in the series required to reach the exact solution.[41] Although this is obviously impossible to carry out, each further term in the series should bring the calculated energy closer to the exact value. Increasing the number of terms increases the accuracy of the calculation, but also increases computational time. A compromise between computational time available and degree of accuracy required will always be needed; this is common to all computational techniques.

In this work MP2[42] (2 is the order of the perturbation) is used as this gave the best compromise between speed and accuracy for the required calculations; however, higher numbers of perturbations can also be used (*e.g.* MP3[43], MP4[44]). To reduce the computational time even further MP theory is often only performed

upon valence electrons using a pseudopotential to approximate the effect of the core orbitals. The electrons in these low-lying orbitals are not involved in any chemistry, but failure to model them leads to a poor description of the more important valence electrons as the electron-electron repulsions are neglected. To model these core electrons explicitly a large number of orbitals would be needed and this is computationally expensive. The pseudopotential considers all of the core electrons collectively, rather than treating each electron explicitly, which will still provide good results but at a reduced cost.[39]

1.3.4 Basis sets

A basis set is a set of functions used to create molecular orbitals (MO). A MO describes the electronic behaviour within a molecule. This description is complete if using an infinite number of functions, called a complete basis set, which is impossible. However, for the purposes of any calculation an approximate MO can be created using certain sets of functions. The selection of basis set is dependent upon the atoms within the studied molecule, as well as the accuracy required.

The majority of functions used to describe these atomic orbitals are Gaussian, as these are computationally simple, and therefore aid in the reduction of computational time. The combination of a number of different Gaussian peaks is used to approximate each AO and ultimately the full MO.

Several different basis set types were used in this work, such as 6-311++G**, LANL2DZ and aug-cc-pVDZ. Each has its own merits, as will be outlined below; the basis sets chosen often depend on the system being studied.

1.3.4.1 Pople-type basis sets

Split-valence basis sets separate the orbitals into core and valence parts. This is common to many basis-set types, but in Pople-type basis sets, the core orbitals

are described by some number of basis functions, with the more important valence orbitals described by other basis functions. 6-31G[45,46] is an example of a Pople-type basis set, where one constructed Gaussian set is used to describe the core orbitals, consisting of 6 Gaussians held at fixed ratios (contracted). The valence orbitals are described by two different constructed Gaussians, one of 3 contracted Gaussians and the other of 1 contracted Gaussian.

The basis set 6-311+G*[47,48] has been used for molecular dynamics (MD) simulations later in this work. The + sign denotes that diffuse functions are included, increasing the volume of space considered in which electrons can exist. This is especially useful when dealing with anions or electron-rich areas. The * denotes polarisation, which is the addition of extra orbitals of higher angular momentum.

1.3.4.2 Dunning-type basis sets

Mentioned earlier, aug-cc-pVDZ[49,50] is an example of a Dunning-type basis set. These basis sets are more flexible than Pople-type ones due to the use of separate exponents for the s and p orbitals, but are computationally more expensive because of this. As with the Pople-type basis sets, the Dunning-type basis sets are split-valence.[39]

These basis sets contain successive, increasing shells of polarisation functions, resulting in the Hartree-Fock energy converging as the number functions increases. For example, the minimum basis required to describe a 1s, 2s and 2p orbital is five functions. A double zeta (DZ) basis set would use 10 functions, a triple zeta (TZ), 15. This presents the opportunity to extrapolate to a theoretical infinite basis set from calculations run at, for example, TZ,[49,50] QZ[49,51] and 5Z,[52] representing 3, 4 and 5 times the number of functions in the minimum basis, respectively.

1.3.5 Density functional theory (DFT)

DFT utilises electron density as its main description of molecular structure. First proposed by Hohenberg and Kohn in the early 1960s,[53] it is dependent on three spatial variables (x, y and z) describing the density of electrons. Compared to $3N$ degrees of freedom in true *ab initio* calculations, the need to describe only three parameters results in shorter computing times.

Theoretically, DFT should be able to produce exact representations of ground-state parameters for any system by utilising a functional to describe the electron density. However, this functional is not known and all DFT calculations are based on approximations of the exchange-correlation potential. As a result, DFT approximates electron correlation as well as electron exchange, which HF theory obtains exactly. Luckily even simple approximations such as the Local Density Approximation (LDA)[53] will, for most cases, yield good results for this exchange-correlation potential. Within LDA the Hamiltonian operator is replaced by another operator, which involves the kinetic energy of a homogeneous gas cloud. This is a good approximation for systems such as metals which contain a sea of electrons.

For molecular systems, however, LDA does not give such good results. The Generalised Gradient Approximation (GGA) provides a better fit. GGA calculates an approximation from the density at the coordinate of interest, but also considers the gradient of the density at that point.[54, 55]

1.3.5.1 Time-dependent density functional theory

Time-dependent DFT (TD-DFT)[56] is a variation of DFT used to evaluate processes occurring over time. A large proportion of spectroscopy involves exciting molecules from their ground states, studying the absorption or emission of radiation. The pathways of relaxation after excitation can be considered using TD-DFT, evaluating the response of electron density to excitation over time. In

Chapter 5 of this thesis, TD-DFT is used to study the dynamics of a system over a few picoseconds.

1.3.5.2 Hybrid DFT

While the ability of DFT to reduce computational time is highly desirable, the need to approximate electron exchange is a significant drawback. Similarly, while the ability of HF theory to obtain electron exchange exactly is useful, it ignores electron correlation. The combination of parts of both theories can provide a best-of-both-worlds situation, where the computation time is comparable to that of HF alone, but the results are more accurate than for pure DFT alone. These combinations are known as hybrid DFT. Hybrid DFT combines weighted parts of each of HF, LDA and GGA theories. The weightings are determined empirically from sets of test molecules.

DFT is a semi-empirical method as the only way to test the effectiveness of a functional is to compare to sets of test molecules already experimentally determined. One method, for which this has been done extensively, is B3LYP.[57,58,59] An example of a hybrid DFT functional, B3LYP is the most used functional, due to its relatively low computational cost; it has been benchmarked so often that credible results are more likely.

1.3.6 Molecular dynamics

Atomic movement in molecules can be modelled using molecular dynamics simulations. Propagating a molecule in set time increments, computing forces at each step, allows molecular motion to be simulated.[60]

As described in Section 1.2 the gas electron diffraction data we collect are a representation of the time-averaged structure of the molecule being studied. Molecular dynamics (MD) simulations use Newtonian mechanics to determine the positions of atoms within the molecule over time. The resulting trajectory can,

therefore, be used to obtain time-averaged theoretical atomic positions which are closely comparable to the results of GED experiments. The field of molecular dynamics is varied and the approach taken is dependent upon both the size of the species being studied, and the accuracy desired from the simulation. For the purposes of this work, isolated molecules with a small number of atoms are studied and so time-dependent density functional theory (TD-DFT) can be used. At each time step a single-point energy calculation computes the forces acting upon the atoms of the molecule. A separate molecular dynamics code propagates the molecule over the defined time step based on these computed forces. This idea is explored further in Chapter 5, where molecular dynamics simulations are used to calculate distance corrections for GED experiments, allowing equilibrium structures to be approximated.

1.3.7 *Ab initio* packages used

To be able to carry out the types of calculations mentioned, commercial quantum chemical packages are used. Gaussian 09[61] is used because it can perform a wide range of calculation types (HF, DFT, CASSCF, *etc*.). In this PhD, Gaussian has been used for all *ab initio* calculations. It has been used to identify lowest energy conformations, to calculate frequencies of vibration of interatomic distances, and to perform single-point TD-DFT calculations in conjunction with the molecular dynamics package Newton-X.

1.4 Vibrational corrections

As already discussed, structural parameters from GED and from *ab initio* calculations are not immediately comparable as electron diffraction gives a time-averaged structure, while computational studies yield minima on the potential-energy surface. In an equilibrium structure bond lengths often differ from those observed in ED. The bond may be longer or shorter, depending on

the nature of the bonding, and the complexity of the vibration.[62, 63] In Figure 1.11 a "shrinkage" of the bond distance can be seen for a linear triatomic molecule. The equilibrium structure is a linear arrangement of the atoms; however, when the molecule bends, the distance between the outermost atoms is shorter than the sum of the two bonded distances. This is true in every instance apart from when the molecule is linear. The average distance (r_a) is therefore shorter than the equilibrium distance (r_e).
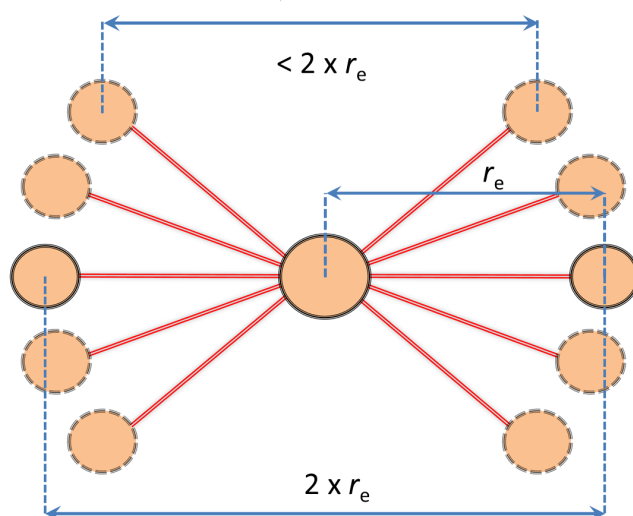
Figure 1.11 – Apparent contraction of triatomic non-bonded distance. For the symmetric bend shown, the interatomic distance between two outside atoms is less than $2r_e$ for all points except when linear. Resulting average non-bonded distance r_a is shorter than r_e.

Corrections can be calculated and applied to the GED structure to produce an approximate equilibrium structure from the experiment. Such corrections are usually obtained using equations of motion coupled to force constants calculated using *ab initio* methods. Although effective for the majority of species studied, failings in the approach are found in the event of large-amplitude or anharmonic vibrations, which are poorly described as they move far from equilibrium.[64] Further discussion, as well as an alternative method of calculating vibrational corrections utilising MD simulations, is covered in Chapter 5.

1.5   Supersonic expansion

Traditional GED experiments study the structures of molecules at room temperature or at the temperature to which the sample is heated. An effusive nozzle, that is one with a Knudsen number > 1, is used. The Knudsen number is the ratio between the mean-free path of the sample molecule to the orifice diameter of the nozzle in this case. Introducing a sample through an effusive nozzle does not appreciably impact the temperature of the sample, as relatively few collisions occur as the sample travels through the nozzle orifice. Molecules introduced in this way, unless they possess very strong intermolecular attraction ($>$ approximately 10 kJ mol^{-1}), experience little-to-no force from surrounding molecules. As relatively few collisions occur, the energetic spread of the molecules is large, with a Boltzmann distribution of states.

Supersonic expansion, a schematic of which is shown in Figure 1.12, impacts the temperature of the sample by adiabatic expansion from a relatively high-pressure to a low-pressure environment.[65] A small orifice, less than the mean free path of the molecules, causes a large number of collisions thereby increasing the velocity homogeneity of the molecules. Figure 1.13 shows the velocity distributions of both an effusive and a supersonic beam. The increase in velocity is due to the adiabatic expansion, with the collisions producing a translationally cooled beam. This means that the molecules are moving in the same direction with similar speeds. A skimmer, as shown in Figure 1.12 selects the central section of the beam, to intersect with the probe, which in the case of GED is a beam of electrons.
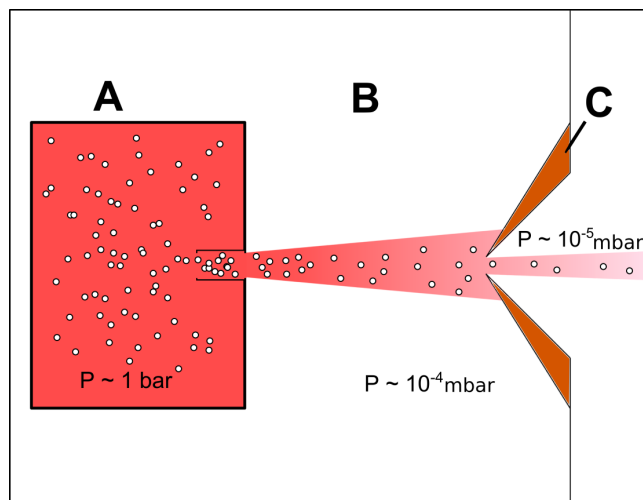
Figure 1.12 – Schematic diagram of a supersonic nozzle assembly. Gas in the reservoir (A) has a Boltzmann distribution of velocities; however, upon adiabatic expansion into a low-pressure environment (B), through a small aperture, the translational temperature is reduced and velocity distribution narrowed. The most translationally cooled part of the beam is selected using the skimmer (C).
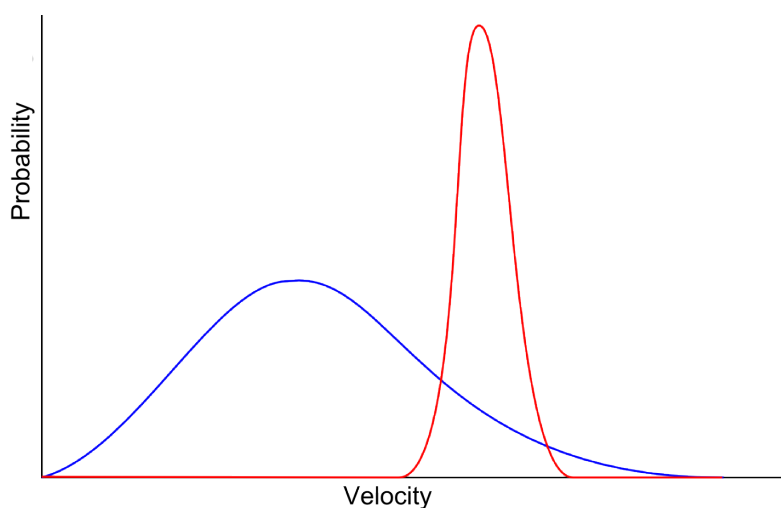
Figure 1.13 – Graph showing the velocity distributions of an effusive beam (blue) and a supersonic expansion beam (red).

Chapter 2

Electron diffraction apparatus

2.1 Introduction

Although the work in this thesis is concerned with the study of samples using a time-averaged gas electron diffraction apparatus, it is important to understand the context of such equipment in the broader field of electron diffraction and in the study of molecular structure in general.

As mentioned in Section 1.1, the majority of molecular structures determined by chemists come from X-ray crystallography, where the large amount of data that can be collected allows complicated structures to be determined using experimental data alone. Gas-phase structure determination cannot match this. The rigidity of the solid comes from intermolecular forces packing the molecules in lattice structures allowing data collected at multiple orientations to be combined (3-D data). Gases are 'free' from these forces allowing the assumption that each molecule exists independently. Although this allows for greater comparison with *ab initio* structures, the lack of an orienting force leads to free rotation of the molecules. Data from GED experiments are, therefore, only one dimensional, requiring additional data to refine more complicated structures.

Some limitations of GED are due to the equipment used and, as such, the design and implementation of apparatus is paramount to the discipline. The York apparatus has been equipped with novel additions to increase the number and variety of species that can be studied: a telefocus electron gun, heated effusive nozzle assembly, supersonic nozzle assembly, and charge coupled device (CCD) camera.

Each of these additions has been utilised in electron diffraction apparatus previously, but not all in one apparatus. In this chapter an overview of the features of the York GED apparatus will be given and compared to electron diffraction apparatus in use by other groups. Improvements will also be discussed that will lead to the results presented in the following chapters.

2.2   GED apparatus

Electron diffraction experiments can generally be divided into two categories: those that use continuous electron beams and those that use pulsed electron beams. Continuous-beam experiments provide information on the time-averaged structures of molecules. Pulsed electron beams, producing bunches of electrons as short as tens of femtoseconds in duration, can be used to take snapshots of molecular structures. Such time-resolved experiments provide information on the dynamics of atoms within the molecules allowing 'molecular movies' to be pieced together.[66]

The University of York is unique in housing both a time-averaged and time-resolved apparatus within the Wann group. Expertise in structure determination from time-averaged experiments, as well as experience in designing custom experimental apparatus within the group aided the design and assembly of a time-resolved electron diffraction (TRED) apparatus as part of another student's PhD thesis.[67] The two apparatus are complementary; samples can be tested for suitability using the time-averaged ED apparatus, allowing optimisation in terms of sample preparation and delivery, and the ground-state structures of molecules of interest can be determined. In determining the suitability of samples, the time-averaged electron gun, when operated at a low beam current (0.1 μA), produces approximately $10^9 \, \mathrm{s}^{-1}$ more electrons than the time-resolved set-up. Samples of gas require high intensities of electrons to allow sufficient scattering to quickly visualise a diffraction pattern. If a high-quality image requires a long exposure time ($\sim 20 \, \mathrm{s}$) using the time-averaged apparatus, it could require a prohibitively lengthy data collection using the TRED apparatus.

This section presents a summary of the experimental apparatus being used presently, as well as descriptions of past assemblies that have served to inform alterations made to the York time-averaged apparatus. Worldwide, the main centres of excellence in time-averaged electron diffraction are in Bielefeld,[68] Christchurch,[69] Ivanovo,[70] and Moscow,[71] and the apparatus used two of these

groups are summarised here.

2.2.1 Time-averaged ED set-ups

The apparatus used in Bielefeld, Germany is the most closely comparable to the York apparatus. It is a modernised Balzers Eldigraph KD-G2 gas electron diffractometer (Figure 2.1),[68] that was originally housed in Tübingen. A telefocus electron gun is used as a source of electrons, and is similar in construction to that used in this work. Gaseous samples are introduced using a heated nozzle assembly, upon which the design for the nozzle built during this PhD, and described in Section 2.3.3.2, is based. The nozzle assembly in York has had to be made smaller to accommodate itself within a 2.75" flange translator used here. The Bielefeld apparatus uses image plates as the detection medium, coupled with a rotating sector. High-quality data have been routinely acquired on this apparatus since it was modernised in 2010.[16, 68]

Figure 2.1 – Photograph of adapted Balzers Eldigraph KD-G2, gas electron diffractometer in Bielefeld, Germany.[68]

The apparatus at the University of Canterbury, Christchurch, New Zealand

(previously the Edinburgh GED apparatus),[69] shown in Figure 2.2, is currently being updated to include a CCD detector as well as the introduction of a very-high-temperature nozzle to study the fragmentation of molecules. Coupling the nozzle with a mass spectrometer allows data collected at the electron detector to be refined with a comprehensive knowledge of the constituent parts of the molecular beam.[70] A similar pairing is possible in York as a mass spectrometer is present alongside a supersonic nozzle assembly outlined in Section 2.3.3.1. Electrons are produced from a tungsten filament, as in the York apparatus; however, the well-collimated beam used for diffraction in Christchurch is achieved using apertures, resulting in a loss of beam intensity. As described in Section 2.3.1 the York apparatus uses a telefocus electron gun without apertures.
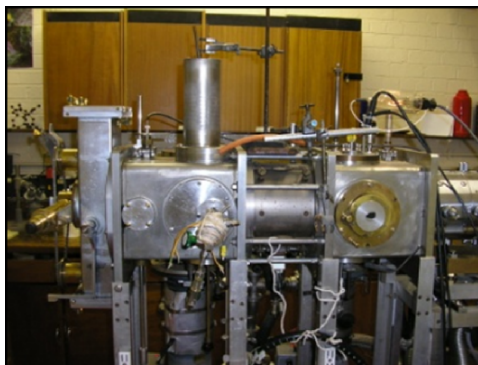
Figure 2.2 – Photograph of the gas electron diffractometer used at the University of Canterbury, Christchurch, New Zealand.

2.2.1.1   GED of clusters

In Orsay, France, an apparatus was designed to probe the structure of clusters produced from a supersonic nozzle using GED.[72] Clusters of argon atoms were produced within the cooled beam produced from the supersonic nozzle; the size and structure of the clusters were determined. This apparatus is shown in Figure 2.3.
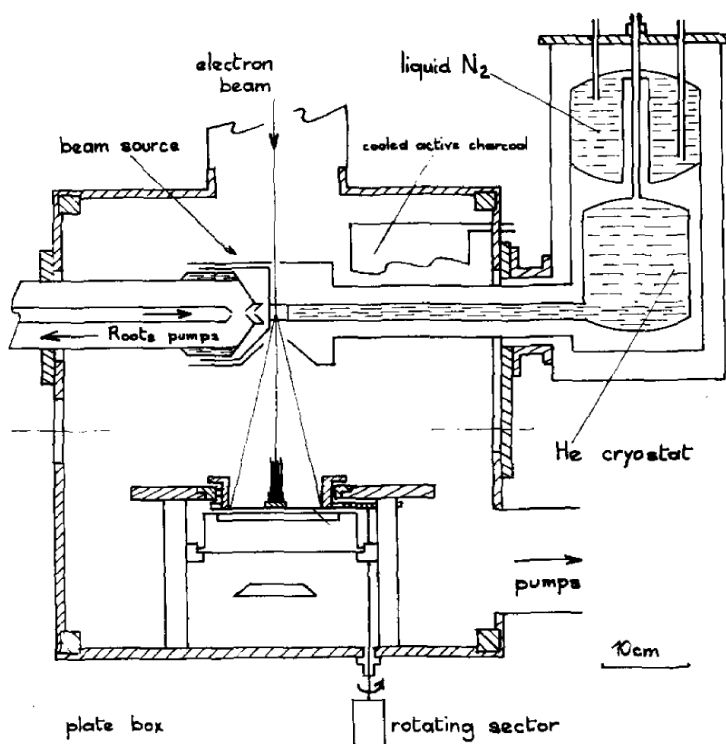
Figure 2.3 – Simple schematic of gas electron diffractometer used in Orsay, France.[72]

Other groups have carried out further experiments using supersonic expansion nozzles, using the technique to study small-molecule clusters such as SF_6 and H_2O.[73] The group of Stein, after collecting data using photographic detection and a rotating sector, altered their apparatus to utilise an electron-counting detector.[74]

Clusters produced from a supersonic nozzle often vary in size and structure within the beam.[73] Although control of experimental parameters, such as orifice size or pressure behind the nozzle, can be used to tune the structures obtained, the production of a consistent size or shape of cluster is unlikely. Park *et al.*,[75] solved this problem using a Paul radio frequency (RF) trap. Mass selected within the trap, a beam of consistently sized clusters can be produced, allowing far more accurate structure determination.

Further to this work, the structures of metal clusters (*e.g.* Ag_n^+) have been determined using an RF trap in Karlsruhe, Germany.[76] Figure 2.4 shows a schematic of the experimental set-up used. Ions created in the magnetron cluster

source are steered into the ion trap, through which the electron beam travels. Approximately 400 images are required, each of 30 s exposure time to produce a high-quality diffraction pattern.[77] The CCD camera behind a phosphor screen allows this acquisition.
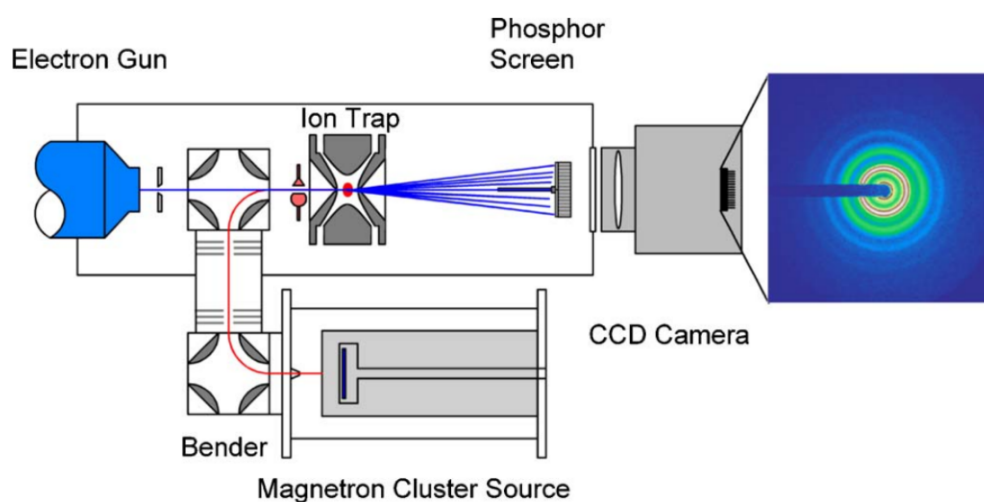
Figure 2.4 – Simple schematic of gas electron diffractometer used in Karlsruhe, Germany.[77]

2.2.1.2 Alignment of molecules

As mentioned in Chapter 1.1, the data obtained from GED are 1-D because of the free rotation of molecules in the gas phase. One solution to this problem is to orient the molecules allowing 2-D data to be collected. Alignment of molecules to maximise the available data has been performed by the Centurion group in Nebraska.[78] Femtosecond laser pulses are used to excite a superposition of rotational states of the sample molecules. In the initial study CF_3I was chosen; a 'spinning top' molecule, containing a heavy atom and three light atoms in a carbon-centred tetrahedral structure. The orienting pulse aligns the molecules along the axis through the central atom and heavy atom, allowing 2-D data to be obtained. Pulses from the same laser are then used to produce packets of electrons to probe the structure. The time delay between excitation and probe is varied

until the most asymmetric pattern is obtained. An example of the diffraction patterns obtained, and its theoretical counterpart is shown in Figure 2.5.
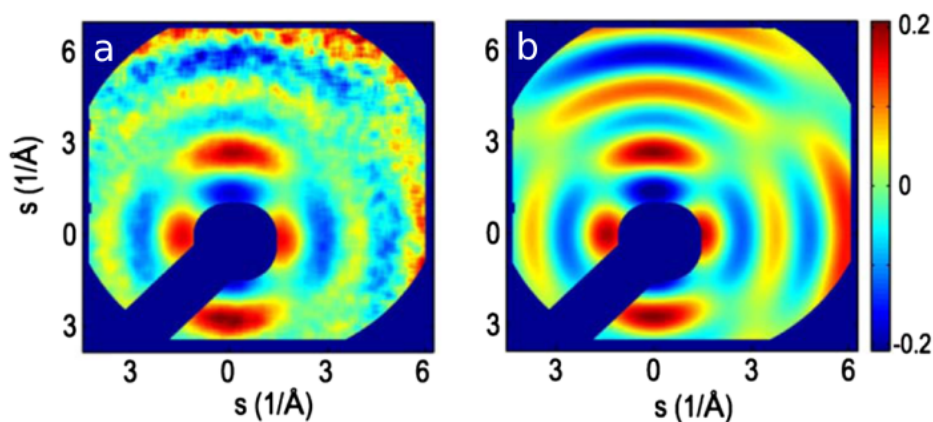
Figure 2.5 – Diffraction patterns for CF_3I depicting (a) experimental and (b) theoretical data, with an alignment of $60°$ relative to the electron beam.[78]

Although carried out using a pulsed electron beam as the structure probe, the output is a static image of the ground state of the molecule, more comparable with traditional GED than a time-resolved experiment.

2.2.2 Time-resolved ED set-ups

Time-resolved electron diffraction (TRED) has evolved as a separate field, motivated by a desire to understand the structures of molecules changing over time. Initially, mechanical chopping of the beam was performed using rotating blockers to produce shorter pulses from continuous electron sources. This was superseded by a 'stroboscopic beam' approach, where a continuous electron beam was electromagnetically deflected to give microsecond pulses, which were used to identify the trifluoromethyl (CF_3) radical produced from multiphoton photolysis of trifluoromethyliodide (CF_3I).[79] This technique became unsatisfactory as shorter pulses were required; laser excitation has become the standard approach to producing femtosecond electron bunches to probe structure.[80, 81]

Unlike experiments that use a continuous electron source, the goal of TRED is the determination of 'snapshots' of a molecular structure as it changes over time. Combining such data together yields a 'molecular movie' of the structural dynamics. The dynamics of interest in the molecules are normally studied using a pump-probe approach.[82] A change in structure is initiated using a laser pulse (pump), which is then probed using a pulse of electrons. By varying the delay between the pump and the probe the structure at different points in time can be studied.[83]

The work of Ahmed Zewail improved the time resolution of the technique from the nanosecond to the femtosecond regime through the use of a number of time-resolved diffractometers.[84, 85] Figure 2.6 shows Zewail's UED-3 apparatus. Improvements were not only in the apparatus used, but also in the theory underpinning TRED.[86]

The main benefit of TRED is that dynamics can be, after data refinement, 'observed' rather than inferred as with spectroscopic techniques; the data collected giving information on the movement of the atoms within the molecule. Electron bunches of femtosecond duration can now be produced, presenting the exciting possibility of viewing chemical reactions and the resulting structural changes. For a more in-depth summary of time-resolved electron diffraction see the review of Sciaini and Miller.[66]
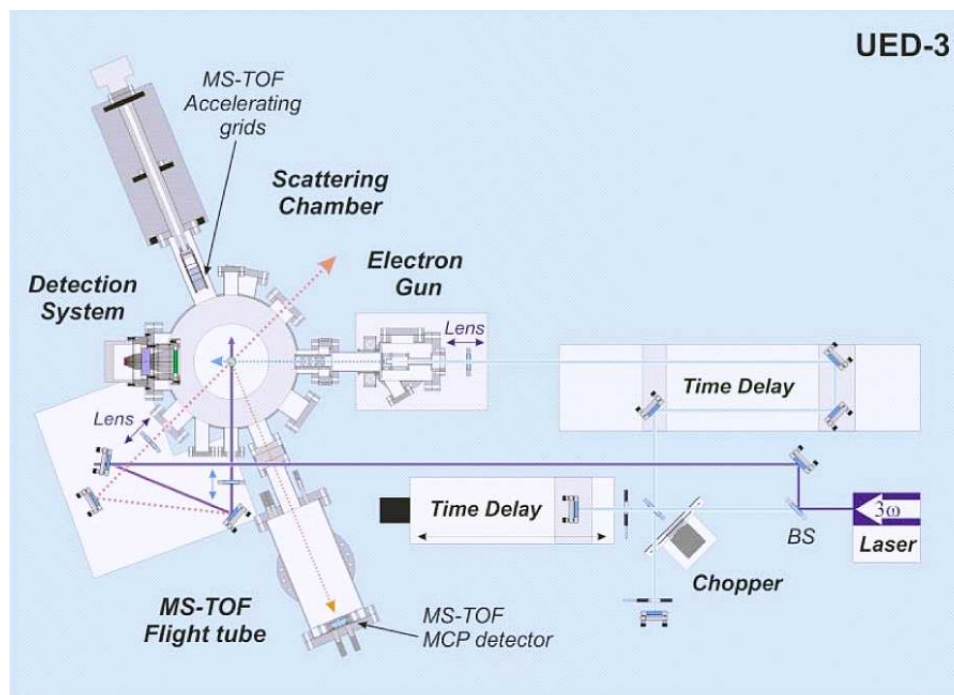
Figure 2.6 – Schematic of Zewail's UED-3 apparatus, used to probe structural changes on the femtosecond time scale.[87]

2.3   York gas electron diffractometer

The York time-averaged GED apparatus is described in this section. In addition to more detail concerning the novel additions that have been mentioned previously, a comprehensive outline of the apparatus as a whole is also provided. The work presented here builds on that of previous PhD students who have contributed to the apparatus.[11, 88, 89]

As mentioned earlier, the main purpose of adapting this apparatus is to increase the variety of species that can be studied using the GED technique. The electron gun in York produces a larger number of electrons, as a narrow and well-collimated beam, than a conventional GED electron gun, as used in Christchurch; because of this, more diffraction events occur for the same density of sample molecules. The camera assembly, meanwhile, offers real-time and almost limitless data acquisition, allowing quick optimisation of experimental parameters, as well as the combination of multiple images which effectively

66

increases the dynamic range of the detection medium. Together these factors allow a greater data output from low-target-density samples.

Two nozzle assemblies are used within the York apparatus. One allows the introduction of samples with low vapour pressures (heated effusive nozzle), while the other allows adiabatically cooled samples to be introduced (supersonic nozzle). Both nozzles are described in more detail in Section 2.3.3. Using the supersonic pulsed nozzle requires a carrier gas to achieve the necessary cooling effect, meaning the sample of interest is often the minority constituent of the molecular beam. The resulting low target density of gas requires a high flux of electrons to enable an appreciable diffraction pattern to be collected. The high-intensity electron beam produced using the York telefocus electron gun should allow these sample beams to be probed more easily.

A schematic of the York apparatus is shown in Figure 2.7. The apparatus is made up of four separate vacuum chambers, with approximate pressures of 10^{-6} mbar, 10^{-5} mbar, 10^{-7} mbar, and 10^{-7} mbar, for the electron gun (A), diffraction chamber (B), and detector chambers (C and D), respectively. The detector can be moved within chambers C and D to acquire different nozzle-to-camera distances. Each of the chambers is pumped using a diffusion pump, with the pumps for chambers A, C and D connected to $N_2(l)$ baffles to maintain an oil-free electron beam path. The diffusion pump in the diffraction chamber lies far from the beam line and so is attached to a water baffle. Chambers A-C are backed by an Edwards E2M80 rotary pump, with D backed by an Edwards E2M30 rotary pump. Between chambers C and D a gate valve allows the vacuum to be maintained in A-C, when chamber D is at atmospheric pressure. The ability to isolate different parts of the apparatus allowed the electron gun to be kept under vacuum when working with the camera assemblies during the calibration experiments described in Section 4.3.
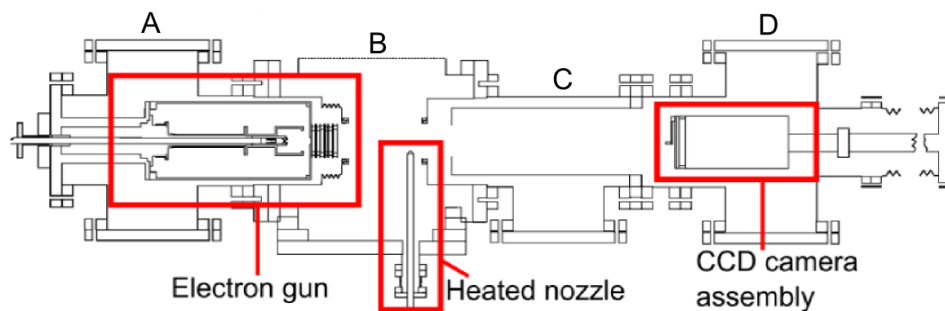
Figure 2.7 – Schematic of the York time-averaged apparatus. Image shows experimental assembly used for effusive sample introduction. Separate chambers of the apparatus are labelled A-D.

2.3.1 Telefocus electron gun

The main components of the York telefocus electron gun are depicted and labelled in Figure 2.8.
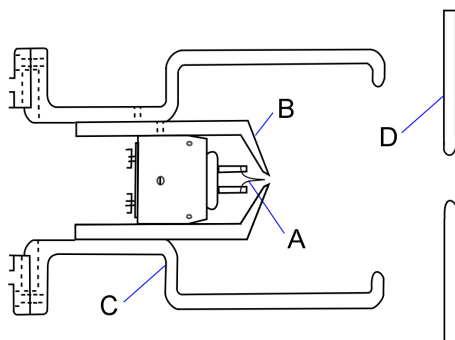
Figure 2.8 – Schematic of the main parts of the telefocus electron gun in the York time-averaged apparatus, showing the tungsten filament (A), the copper Wehnelt cap (B), the Wehnelt cylinder (C), and the anode (D).

A tungsten filament (A; Siemens AGA052) is housed within an oxygen-free copper Wehnelt cap (B). A current of 2.3 A causes thermionic emission of electrons from the filament, which is held at potentials up to -40 kV; the electrons are accelerated towards the grounded anode (D). To control the emission of electrons, a bias potential is applied between the filament and the Wehnelt cap.

This potential can be varied from zero to 150 V, controlling the emission of electrons. Figure 2.9 shows a triode system with a set-up comparable to that used in our apparatus.
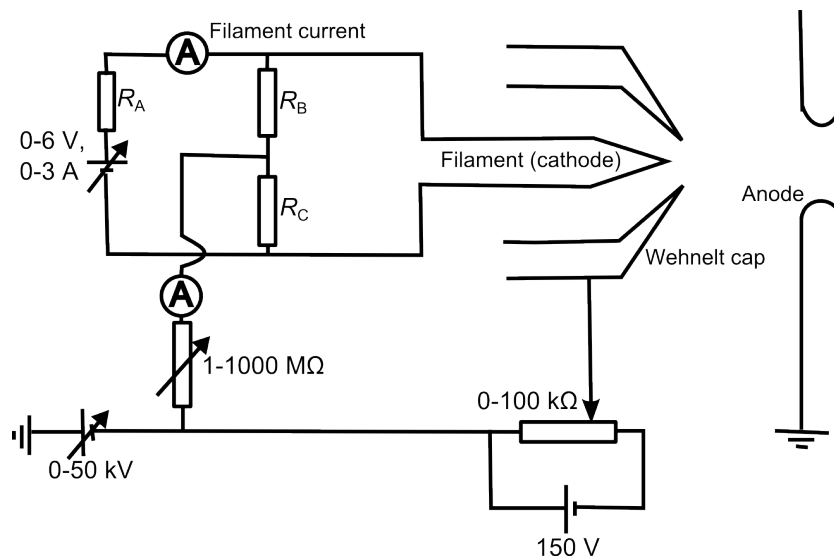
Figure 2.9 – An example of a triode telefocus electron gun. Image redrawn from an image in the thesis of Stuart Hayes.[11]

The novel function of a telefocus gun is the focussing effect, which is achieved by impinging upon the electric field between the cathode and anode with a specially shaped Wehnelt cylinder (C in Figure 2.8).[90] Figure 2.10 shows that the lines of equipotential electric field (red) are affected by the Wehnelt cylinder resulting in a lensing effect of the electron beam (blue).

The shape of the cylinder alters the electric field to produce an effect akin to the optical focussing of light using shaped lenses. Varying the distances between the filament, Wehnelt cap, and anode of the gun will alter the focussing effect. This is different from a conventional electron gun, such as the one used in the Christchurch apparatus or in an electron microscope, where magnetic lenses are used to focus and steer electron beams; the beam quality is maintained through the use of a number of pinhole apertures. The resultant beam from a telefocus gun can, therefore, have a much greater intensity, with a similar beam size to that generated in a gun using lenses and apertures.
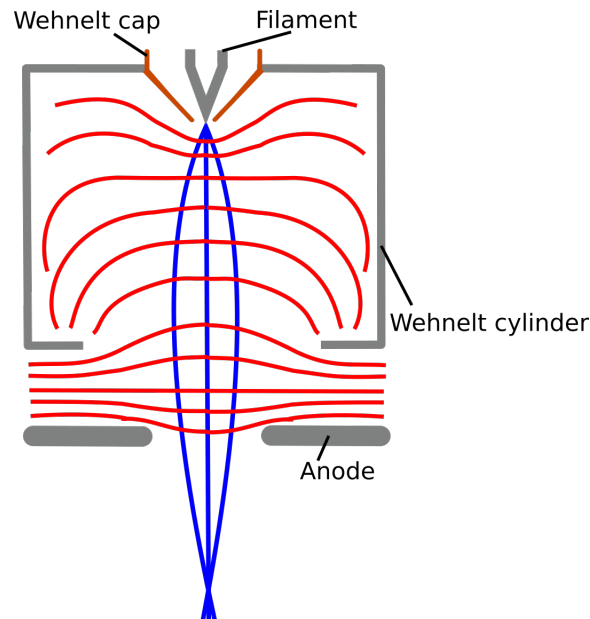
Figure 2.10 – A simple schematic of the lensing effect of the Wehnelt cylinder showing equipotential lines (red).[90]

After the anode of the electron gun is a series of steering plates, shown in Figure 2.11. Two plates are used to deflect the electron beam up and down, and a further two are used to steer the beam left and right. The ability to control the trajectory of the beam is important for the initial set-up of the gun, and subsequent calibration explained in Section 4.2.1.
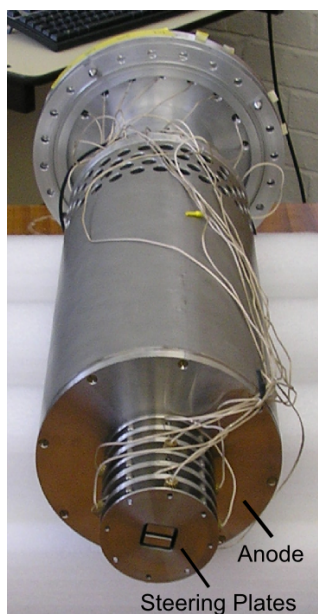
Figure 2.11 – Photograph of the telefocus electron gun used in the York time-averaged apparatus.

During the course of this PhD the apparatus was moved from Edinburgh to York, and the opportunity was taken to recalibrate the electron gun. The changes made to the gun, and the resulting improvement in the beam quality, are outlined in Section 4.2.

To allow easy alignment of the electron beam, and to aid in the beam profiling reported in Section 4.2.1, a beam tube (shown in Figure 2.12) can be placed within the diffraction chamber. The tube consists of two electrically isolated collars, through which the electrons travel to reach the detector. By varying the voltage applied across the steering plates, the electron beam can be diverted to hit either the near or far collar, where a current is recorded. By aligning the beam to initially strike the collar nearer to the gun, then to strike the far collar, and eventually to pass through without any current being recorded, the beam is considered to be aligned through the apparatus and the camera can be positioned accordingly.
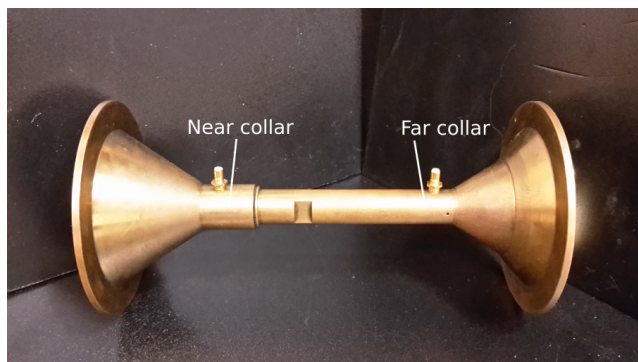
Figure 2.12 – The brass beam tube used for electron beam alignment in the York GED apparatus.

2.3.2 Cold trap

Although the focussing of the electrons leads to a well-collimated electron beam, stray electrons are still produced, which can increase the detectable background. As part of this PhD a simple cold trap was designed and built in-house (see Figure 2.13). The trap doubles as both a clean-up aperture (5 mm diameter) before the point of diffraction, and also acts as a surface onto which the sample can condense. The trap acts to block all light and electrons from the filament that is not travelling parallel to the main electron beam, reducing the observed background at the detector. The light causes a problem at the detector as the phosphor screen, used to convert incident electrons into photons, is not sufficiently opaque to block background light from reaching the CCD chip. The lower the light level in the apparatus, the better the signal-to-noise ratio, increasing the chances of detecting sufficient electrons at a higher scattering angle, which are rarer events.

The main function of the cold trap is to condense sample gas after the nozzle to reduce the chance of multiple diffraction along the electron beam path due to gas migration. This was suggested as a possible source of inaccurate data at extreme values of s reported in a previous PhD student's thesis.[11] Background gas already present in the chamber condenses as well as sample when the trap is cold, further reducing the pressure in the chamber.

The trap consists of two main pieces: a copper end piece (A), and a stainless steel reservoir (B), both shown in Figure 2.13. The copper end piece has four holes in it. Two for the electron beam to pass through, and two along the axis travelled by the sample gas jet. The 'sample' hole is large enough for the heated nozzle assembly to fit through, allowing the tip of the nozzle to be as close to the point of diffraction as possible, maximising target density. The first 'electron' hole is the 5 mm aperture mentioned previously, with a larger hole towards the camera allowing both the undiffracted beam and the diffracted electrons to proceed towards the detector.

Figure 2.13 – Photograph of the cold trap used in the York time-averaged apparatus. The stainless steel reservoir (B) holds $N_2(l)$ to cool the trap. The copper end piece (A), is the surface onto which the sample condenses.

Liquid nitrogen, which acts as the coolant, is held in the stainless steel reservoir. The reservoir is designed such that the vacuum present in the apparatus extends to the top of the reservoir, insulating to some extent the body of the reservoir from the main chamber of the apparatus. This is necessary so that metal contraction does not occur at the knife edge of the vacuum seal.

The cold trap is in a fixed position, and fits closely to the heated nozzle, ensuring that the point of diffraction is relatively fixed. As the calibration of the apparatus required the precise knowledge of the nozzle-to-camera distance, the fixed point of diffraction simplifies measurement.

2.3.3   Nozzles used in apparatus

Nozzles are required to deliver a beam of gaseous molecules to the point where diffraction can occur. Many of the samples studied using GED do not have significant vapour pressures under normal conditions; nozzles designed to increase the vapour produced are, therefore, vitally important. An effusive nozzle, with a diameter far greater than the mean free path of the molecule, results in little or no collisional cooling.[91] To a reasonable approximation the temperature of the sample can be assumed to be the temperature at the tip of the nozzle and so easily measured using a thermocouple. Our apparatus retains the ability to perform GED using effusive nozzles, both at room temperature and heated to more than 600 K. In addition to this, however, we have the capability with this apparatus to introduce the sample seeded in a carrier gas as a supersonic beam.

2.3.3.1   Pulsed supersonic nozzle

As described in Section 1.5, the expansion of gas from high pressure to relatively low pressure through a small orifice results in a cooling effect. Collisions between molecules reduce the translational, rotational and vibrational energy. Routinely used in spectroscopy, where molecules are required in the vibrational ground state, supersonic nozzles have until relatively recently only been used in the field of GED in the study of clusters. Clusters form upon cooling as the energy of the molecules is lowered such that weaker interactions can become significant.[73]

In York a General Valve pulsed nozzle has been combined with a skimmer

box assembly to form the supersonic expansion set-up shown in Figure 2.14. This is similar to a Campargue nozzle assembly, although only one skimmer is employed.[92] Work carried out by Bartell *et al.* suggested that, because of the high sample density required, two skimmers would not be desirable in GED experiments.[91]
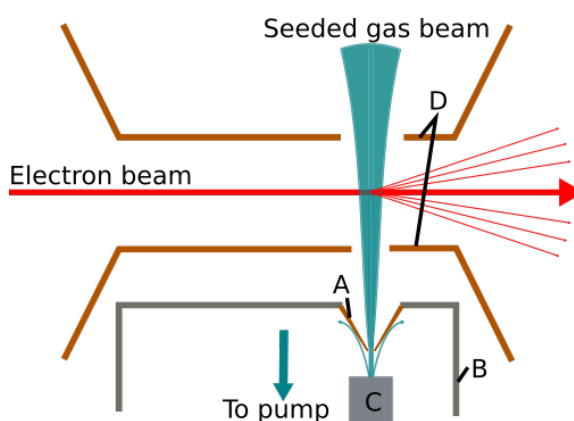
Figure 2.14 – Simple schematic of the supersonic expansion nozzle assembly. The main components are: the skimmer (A), housed within the skimmer box (B) separating the main diffraction chamber from the pulsed nozzle (C), and the beam tube (D), to which the box is also mounted.

An approximation of the cooling possible in the York set-up has been calculated previously, with approximate temperatures of 2 K translational, 20 K rotational and 100 K vibrational determined.[11]

The skimmer box separates the diffraction chamber from the nozzle. The nozzle chamber, behind the skimmer box, is pumped by a roots blower pump (Edwards 80, coupled to a mechanical booster) to remove the large quantity of gas that does not pass through the skimmer. To ensure the correct alignment of electron and sample beams, the skimmer box is connected to the beam tube through which the electron beam passes.

The skimmer itself admits only those molecules travelling parallel to the nozzle axis, selecting the most translationally cooled molecules. The velocity spread of the resulting beam is far smaller than for a corresponding effusive beam. The

pulsed beam reduces the amount of gas that has to be pumped away allowing higher pressures to be achieved behind the valve, while maintaining a low pressure within the skimmer box, and, as explained in Section 1.5, ultimately, lower vibrational temperature of the sample. No significant changes have been made to this assembly over that described in the theses of Fender and Hayes.[11, 88] No experiments using the supersonic assembly have been carried out in this work.

2.3.3.2   Heated nozzle

An effusive nozzle capable of heating samples to temperatures of 675 K, has been designed and built in-house as part of this PhD. The nozzle is heated using air passed through a threaded in-line heater [Sylvania 3/8" F038821; shown in Figure 2.15(c)], while Figure 2.16 is a schematic diagram of the nozzle and shows the direction of travel of the heated air. The hot air passes through the space between pipes C and D, towards the copper tip (A) of the nozzle, before passing back between pipes C and B and exiting out the back of the nozzle. A temperature gradient of about 5 °C is maintained between the hotter tip and the cooler exit point where the sample is attached. This is necessary to ensure no sample condenses in the nozzle itself, or in the flow controlling valve.
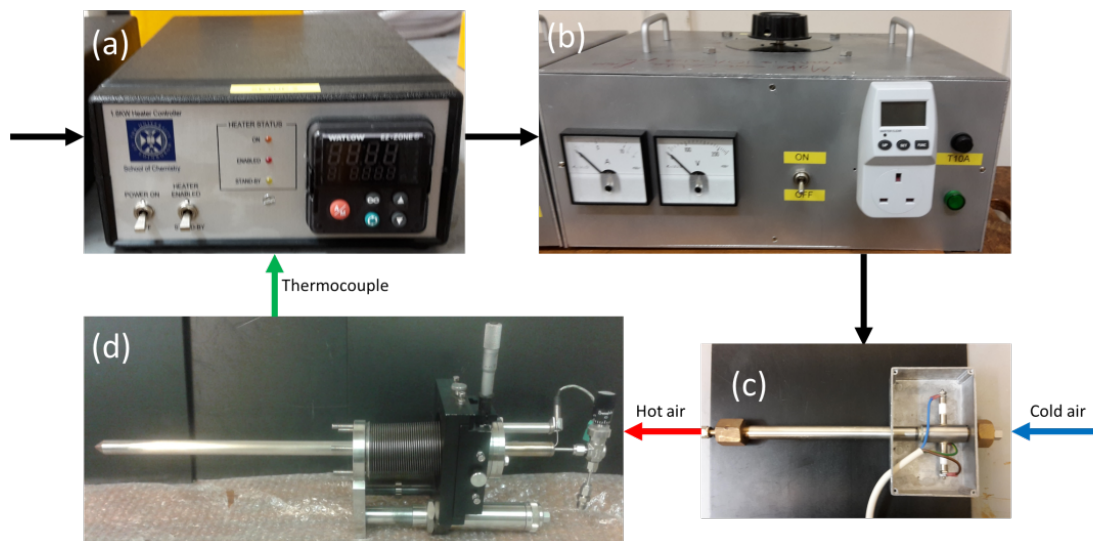
Figure 2.15 – Schematic of the heating assembly used for the heated nozzle. The photographs show (a) the PID controller, (b) the variable resistor, (c) the inline heater, and (d) the heated nozzle.
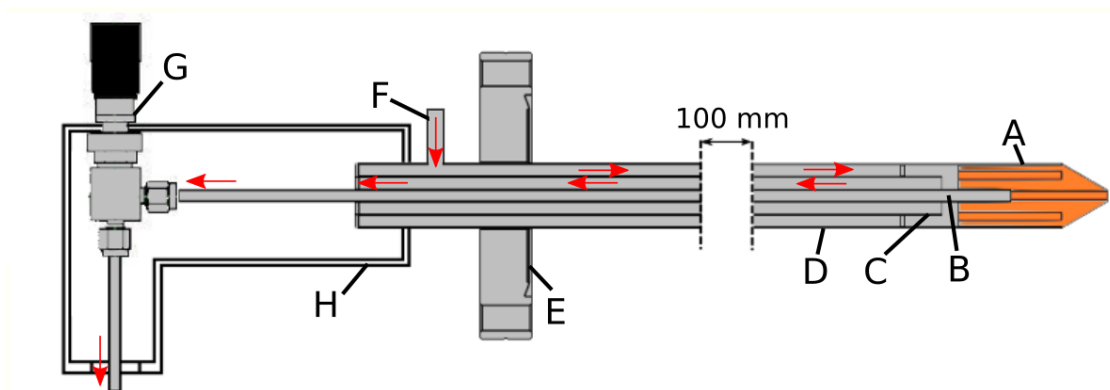
Figure 2.16 – Schematic of the heated nozzle construction. Red arrows denote the direction of air flow. Main components are nozzle tip (A), sample tube [B, $\frac{1}{8}$″ Stainless Steel (SS)], central tube (C, $\frac{3}{8}$″ SS), outer tube (D, $\frac{5}{8}$″ SS), 2.75″ flange (E, SS), air inlet (F, $\frac{1}{4}$″ SS), metering valve (G), and aluminium casing (H).

The temperature of the air used to heat the nozzle, is controlled using a combination of a proportional-integral-derivative (PID) controller and a large variable resistor, shown in Figures 2.15(a) and 2.15(b), respectively. A separate but identical heated air system is used to heat the sample vial, shown in Figure 2.17, to give greater control over temperatures directly applied to the samples of interest.[93] This is crucial as we will often work with small amounts of custom-made samples close to their decomposition temperatures to produce the highest sample density possible. The separate PID controllers limit the temperature of the tip of the nozzle and of the sample to $\pm 5\,\mathrm{K}$, while the resistors provide a hard limit in-line heater temperature.

Heated air exiting the back of the pipe assembly of the nozzle is directed using the casing, component H in Figure 2.15, to heat the valve controlling the sample introduction. This casing also acts as the stabilising part of the assembly, preventing excessive strain being applied to the sample vial, shown in Figure 2.17.

Figure 2.17 – Photograph of the sample vial used with the heated nozzle.[94]

2.3.4   Camera assemblies

To collect data, our apparatus is equipped with a camera assembly capable of being moved within the vacuum. Sealed in a vacuum-tight container, the assembly is connected to an *xyz* translator; scanning in the *x* and *y* directions is

performed as described in Section 4.2. In fact two different camera set-ups have been used during this PhD and they are described below. Translating in the z direction allows us to alter the nozzle-to-camera distance without changing the nozzle position; this enables sampling of a sufficient s range. By maintaining the point of diffraction, more complicated nozzle assemblies, as described previously, can be used. Data collection can be performed at several nozzle-to-camera distances; overlapping datasets, where the differences between nozzle-to-camera distances are well known can be used to check data quality. By refining data at these known differences, any problems with the experimental data can be identified.

CCD cameras offer almost limitless data acquisition, instant data quality checking and greater adaptability to the experiment of choice. As such it is preferred here over other detection media, such as photographic films and image plates.

2.3.4.1 Rigaku camera

The camera used at the beginning of this PhD was a prototype of the Mercury II detector, made by Rigaku. The Rigaku assembly is shown in Figure 2.18. Cooled by room temperature water, using thermoelectric cooling, the CCD chip can reach temperatures as low as -40 °C, reducing noise in the data obtained. The camera is held within a vacuum-tight cylinder, that can be placed within the vacuum of the apparatus. Mounted on a translator parallel to the electron beam the camera can record data at many distances from the fixed point of diffraction. In other apparatus data acquisition media often remain stationary, with the point of diffraction changed. If using a more complicated assembly to introduce the sample, this need to move the nozzle can be problematic.
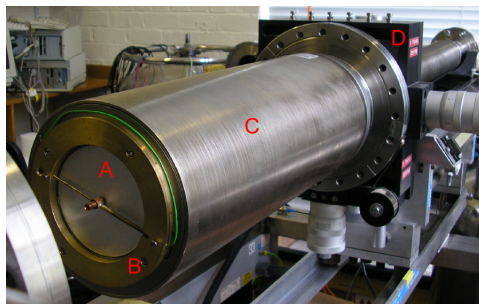
Figure 2.18 – Photograph of the Rigaku camera. The silver colour on the face (A) is the aluminium coating of the phosphor screen. The beam stop and holder (B) allow incident electron beam to be measured down to picoamps. The assembly is housed within a vacuum-tight tube (C), mounted on an *xyz* translator (D).

The CCD chip is a 1024 × 1024 pixel Kodak KAF-1001, with each square pixel 0.024 mm wide; the CCD chip is, therefore, 25 mm wide. For a complete diffraction pattern to be collected a larger detection surface is needed. To achieve this, the chip is connected to a phosphor screen *via* an optical taper. The value of this taper is 3.17 allowing a circular detector face of radius 39 mm. Excess electrons are carried to ground by an aluminium layer (50-70 nm) covering the phosphor screen. To perform a similar job to a rotating sector, a radial apodising filter, darker in the centre and lighter at the edges, is placed behind the phosphor screen, limiting the intensities recorded at smaller scattering angles. This is necessary to allow data to be collected at larger scattering angles.

2.3.4.2 Stingray camera

Due to complications with the electronics of the Rigaku camera set-up, that began on moving from Edinburgh to York, a new camera assembly was designed and built in-house (Figure 2.19). To maintain the ability to record data at multiple nozzle-to-camera distances, this assembly was designed to be similar to the Rigaku camera outlined previously. Figure 2.20 illustrates the assembly and relative distances between components. A Stingray F-146B CCD camera (D),

paired with a Schneider 17 mm focal length lens (E), sits at atmospheric pressure within a vacuum tight cylinder (C) with 98 mm diameter glass viewport (B). By placing the phosphor screen (A) 15 mm in front of the viewport, the image recorded by the camera is of maximum diameter 105 mm. The camera and lens are placed on a runner (G) so the camera-to-phosphor distance can be altered to best focus the image.
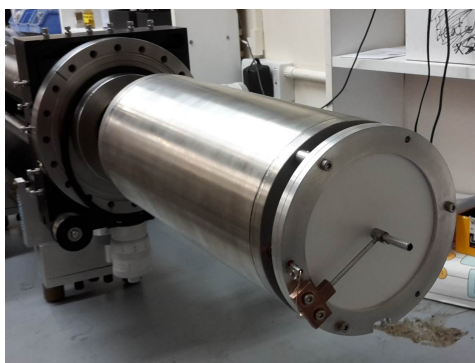
Figure 2.19 – Photograph of Stingray camera assembly attached to the *xyz* translator.

The new assembly differs from the Rigaku camera, in that the components are separate and easily replaced if, for example, the high beam current from the telefocus electron gun impacts directly on the phosphor screen. Unfortunately, the Stingray camera used does not have the same low-light sensitivity as the Rigaku camera, resulting in a larger intensity of electrons required to collect refineable data. The new assembly is 30 mm shorter than the Rigaku assembly, which can be a benefit when using the deep beam stop, shown in Figure 2.19. The deep beam stop is required for high beam intensities, but its length prevented the gate valve from being closed when used with the Rigaku assembly. An apodising filter is also present in the Stingray camera assembly. Held behind the phosphor screen, the filter can be removed or changed if needed for a particular experiment, and performs the same function as for the Rigaku camera.

Alterations were required to the extraction code described in Chapter 3 to accommodate the Stingray camera. This is because of the different number of pixels as well as the change in pixel size compared to the Rigaku camera; the
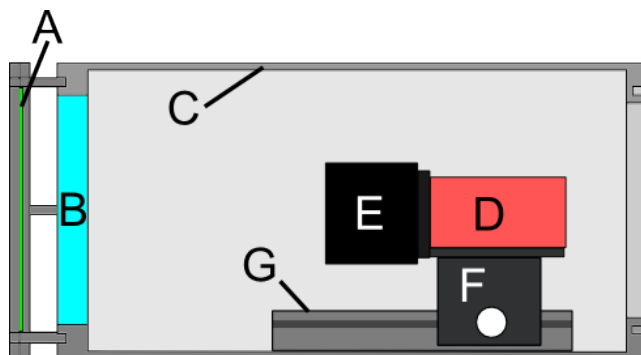
Figure 2.20 – Schematic of the Stingray camera assembly. The P22 phosphor screen (A), is held 15 mm in front of the glass window (B). Within the vacuum tube (C), the CCD camera and lens (D and E, respectively) sit on a holder (F), which is attached to a track (G) to allow movement of the camera.

changes are explained in Chapter 3. Changes to the mask corrections were also required due to the rectangular shape of the CCD chip and different intensity variation within the acquired image, requiring new limits of exclusion of pixels to be coded.

2.3.5   Overview of the apparatus

The temperatures reached using the heated nozzle are relatively low in comparison to very-high temperature nozzle assemblies previously used to study GED of salts,[95] but will provide a consistent and easily controlled temperature for samples that can be studied within this apparatus. This in conjunction with the data acquisition possible using the CCD camera and the intense electron beam will allow the study of particularly low vapour pressure samples.

The York apparatus with these novel additions presents an opportunity to increase the range of compounds studied. Traditional GED structures can be obtained for a number of species that previously lacked the necessary vapour pressure, while the selection of specific states within molecules of interest should now be possible. This could be achieved by combining the cooling of the

supersonic expansion with an excitation laser, which could be incorporated into the apparatus. Time-resolved structures obtained from other apparatus rely to some extent on structures obtained from these time-averaged experiments and, as such, both types of experiment performed in York are complementary.

This potential to both increase the variety of samples suitable for study, but also the nature of the study will increase the continuing applicability of the time-averaged GED technique to the study of structure.

Chapter 3

Extraction software

3.1 Introduction

Once a diffraction pattern has been collected, a number of steps are taken to convert the raw pattern to an intensity curve suitable for use in a refinement. These steps are termed data extraction, and are different for each experimental set-up; this is because of the custom nature of the GED apparatus. Different experimental conditions, as well as different detection media, must be considered when extracting the data, to allow both a refinement and datasets comparable between experimental groups.

Extraction and treatment of data collected using the York time-averaged GED apparatus is outlined in this chapter. Novel extraction code (EDSTRACT, Appendix B) has been written and here I describe the code, as well as testing and calibration that has been performed.

Frequently used extraction scripts that are described in the literature, such as xpkg,[9] are not suitable for use with the camera assemblies in York; the limitless data acquisition and custom design of the cameras require an adapted code that can be improved as the understanding of the apparatus and the different techniques used becomes apparent. As outlined in Section 2.3.4, the camera assemblies we have used contain apodising filters to perform a similar role to a rotating sector, effectively reducing the scattering intensities at narrower angles so that data at wider angles can be detected.

The xpkg code was used with the Edinburgh GED apparatus (now in New Zealand), where the rotating sector is centred with respect to the scattering pattern using a beam stop. The detected beam current, passing through a 0.1 mm diameter aperture, is maximised giving the centre of the beam. The beam stop is fixed at the centre of the rotating sector. In the York apparatus, the centring of the beam stop relative to the optical filter presents a different problem as the filter is fixed and the cup placed approximately over the centre of the camera. This is one of the main apparatus-specific features in EDSTRACT, with the other being the

need to treat malfunctioning pixels and to mask damage to the phosphor screen.

As well as using the Rigaku camera described in Section 2.3.4.1, the Stingray designed camera assembly described in Section 2.3.4.2 has also been used to acquire diffraction images. The required alterations to the code, to account for the differences between the camera assemblies, are outlined in Section 3.2.2

Within this chapter calibration of EDSTRACT with data collected using the old Edinburgh apparatus is performed. To prove the extracted data are of high quality, suitable for refinement, and to illustrate the steps taken in the extraction code, benzene data recorded using the Stingray camera assembly are used.

3.2   Data extraction

For data collected using the York apparatus to be of use they must be formatted for input into the existing refinement software ed@ed.[34] To reach this point the data must first be treated as outlined in Figure 3.1.[96] All of the extraction software used was written in MATLAB and is presented in Appendix B. The EDSTRACT software uses a central script which calls functions to carry out the actions needed. The central script is called Extract_2.m, with the functions: fOpenSSED.m (used with Rigaku camera), fExtract2array.m, fExtract2tot.m, fMaskcorrector.m and fMaskCreator.m.

The central script also calls two small files, one containing a list of constants (sConstants.m), such as the mass of an electron, and the other containing information about the particular data being extracted (sExperimentalInfo.m). The electron wavelength, nozzle-to-camera distance, limits of image from which to extract data, and the pixel size of the camera can all be altered in this file.
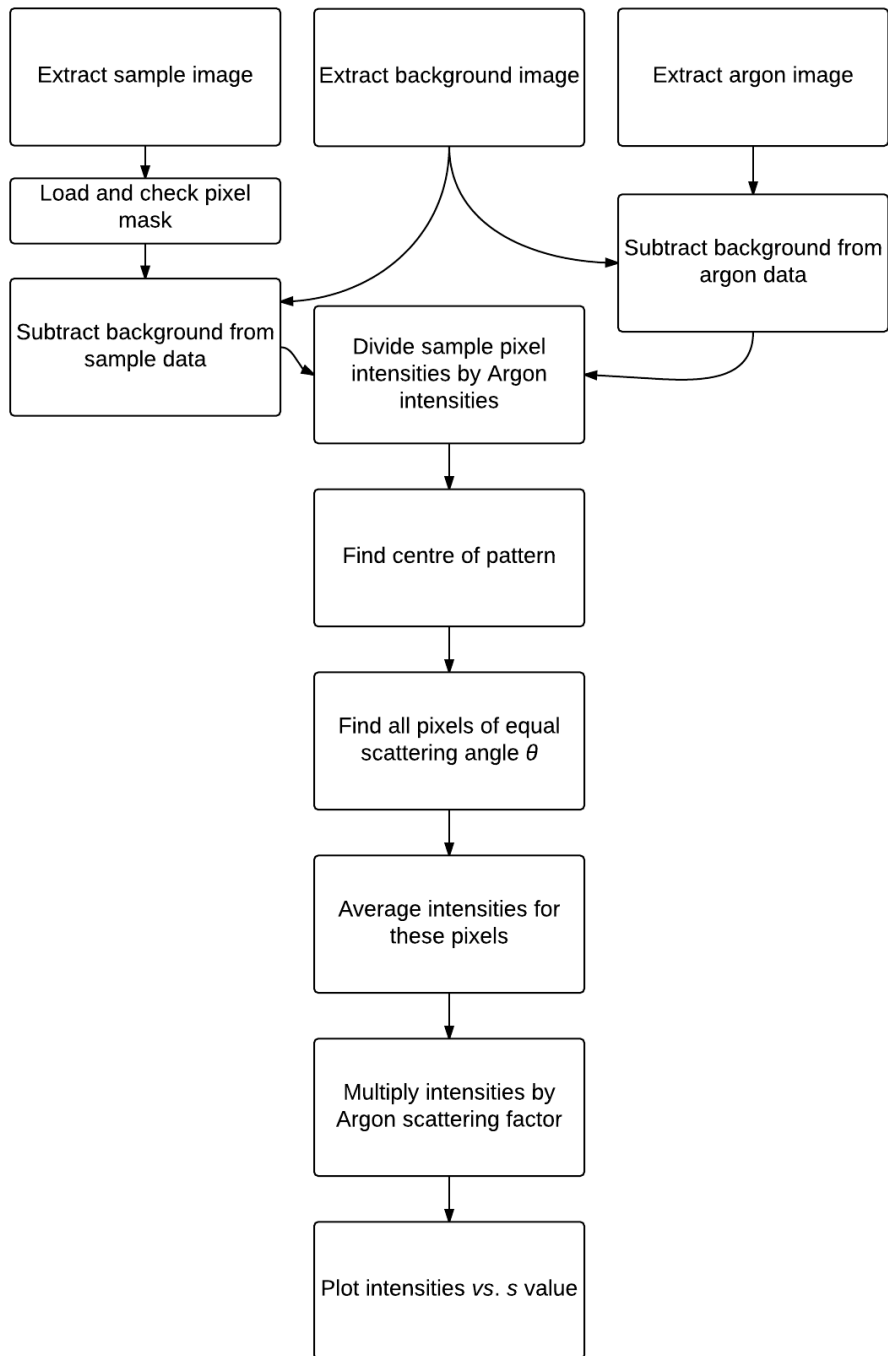
Figure 3.1 – Flowchart depicting the main functions of the extraction software EDSTRACT.

Three images are required to produce refinable data: an image of the diffraction pattern of the sample studied [Figure 3.2(a)], a background image [Figure 3.2(b)], and an argon scattering image [Figure 3.2(c)]. All three are collected using the same exposure time and beam intensity. The argon data obtained are used to perform a number of corrections that would usually be applied after the extraction of data, as well as accounting for the misalignment and precise correction for the optical filter.
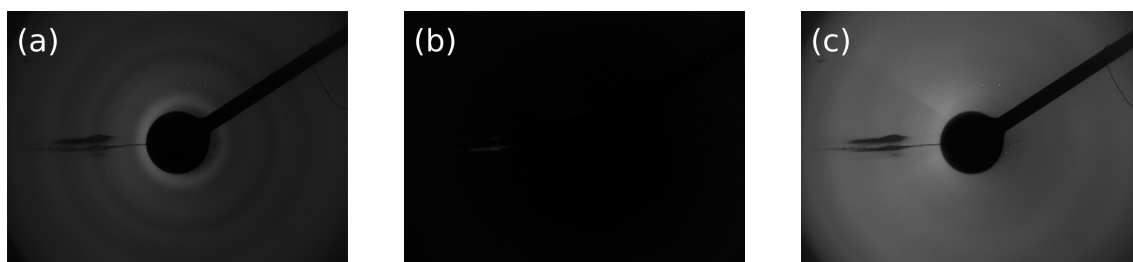
Figure 3.2 – The three images required for extraction of experimental data. The images are for (a) benzene, (b) no sample (background), and (c) argon.

Experimental data for the sample of interest are recorded for an exposure time which is dependent upon the volatility of the sample and the intensity of electron beam being used. The light detected at the CCD camera is not all as a result of diffraction from the gas sample; it also contains light from exposed ion gauge filaments, and from the electron gun filament. Steps are taken to reduce this background light, but it cannot be eradicated entirely. Stray electrons can also be diverted from the central beam trajectory by background scattering with any gas present in the vacuum, or any magnetic field that may be present. To account for these anomalies a background image is used that is acquired under the same conditions as the experimental data, though without sample gas present. Subtracting the background image from the sample diffraction image produces a 'data only' image for refinement. The background-corrected sample image is divided by the argon (minus background) intensities, pixel by pixel. The resulting image (Figure 3.3) is used for the extraction of data.
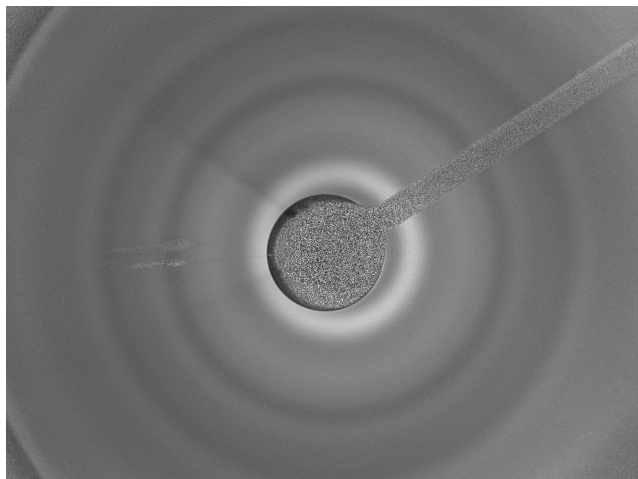
Figure 3.3 – Background-subtracted benzene divided by background-subtracted argon image.

An approximate centre is chosen by visual inspection of the image, giving a starting point for comparison. The centre is calculated first in the x direction and then in the y direction. For the centre with respect to x, a rectangle of pixels is considered with dimensions [9 (y) $\times$ 280 (x)], 320 pixels in the x direction from the proposed centre. Comparison of the extracted intensities, averaged over the 9 pixels, fitted with a second-order polynomial provides the centre. The algorithm is run twice to find both the centre in the x and y directions. The rectangle of pixels considered during the centring process can be adapted depending on the species studied, where prominent rings closer to or further from the centre can be used to produce a more reliable centre. The full extraction of data using EDSTRACT completes in approximately 30 s, allowing experimentation in the centring algorithm to obtain the best centre. Within the code, the sample-divided-by-argon diffraction pattern can be extracted for specific sectors rather than the whole pattern, which can be compared in a graph of intensity *vs. s* value. If the extracted sectors match well, then a good centre has been found.

Once the centre is found, each pixel is grouped in s steps of 2 nm^{-1}, relative to the centre, with the intensities of the pixels averaged over the number of pixels in each group. Each data point is then multiplied by a value equal to 1.0 minus

the corresponding scattering factor for argon at that s value. The scattering factor accounts for the argon scattering in the collected argon image, levelling the sample intensities collected, which is the format that the ed@ed refinement code requires.

The argon scattering patterns are collected using the same experimental conditions as the sample and, as such, can initially flatten the intensities so as to reveal any data present, as well as correcting, in conjunction with the known scattering factors for argon,[97] for problems in the experiment. Corrections applied to data collected using image plates or photographic film include a plate flatness correction due to the detection media not being truly perpendicular to the incident beam, a sector correction to account for the rotating sector employed, as well as the possible misalignment of the centres of the beam and sector. The argon data accounts for the problems seen in the intensities collected, such as badly functioning pixels, or non-uniform phosphorescence from the phosphor screen; however, any distortion to the scattering angle of the collected data features would not be corrected this way. One of the errors that can cause small variations in the s values collected is the camera face not being perpendicular to the incident electron beam. The data collected using both Rigaku and Stingray camera set-ups showed no improvement in the refinement goodness-of-fit R factors when a plate-flatness correction was applied. As such it is not implemented in the code, nor used for the refinements presented in Section 4.3.

The impact of the argon data and scattering factors are shown in Figure 3.4. Data extracted from the benzene image alone [Figure 3.4(a)] show features representing peaks and troughs in intensity; however, the relative intensities are impacted by the drop off in intensity with scattering angle, despite the optical filter limiting exposure at narrow scattering angles. The known scattering of argon with respect to s is roughly an exponential decay, with no additional features. The argon data collected [Figure 3.4(b)] using these camera assemblies differ greatly from this, illustrating the effect of the optical filter. The final multiplication by the scattering factors at particular s values produces the 'uphill

curve' suitable for reading into ed@ed, as shown in Figure 3.4(c).
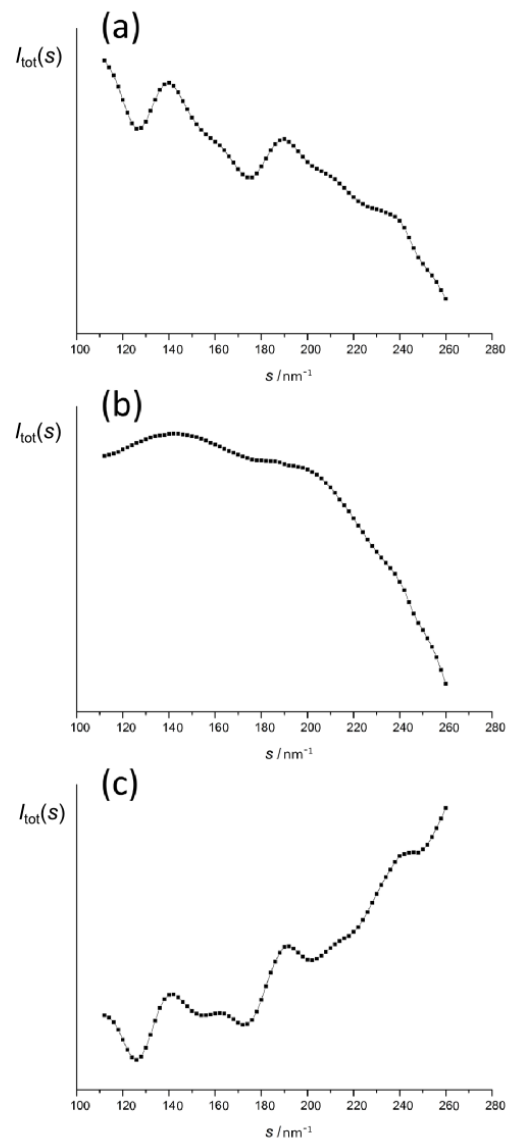
Figure 3.4 – Extracted intensities for (a) a benzene image, (b) an argon image, and (c) the fully corrected benzene intensities suitable for refinement in ed@ed.

The pixels in a CCD camera vary in quality. The majority of imperfections are corrected using the argon image and scattering factors, although some pixels lie behind structural barriers, such as the beam stop, rendering their data useless, or malfunctioning so badly as to be uncorrectable. These pixels must be removed during the extraction process. An initial mask to denote pixels as either 1 (to be

used) and 0 (not to be used), is created using the function fMaskCreator.m, before running the EDSTRACT central script. Two images collected with a sufficiently bright diffracted electron beam, in which the beam stop and arm can be clearly seen, are tested to see whether the recorded intensities fall within set limits. If the recorded pixel intensity lies outside of the set limits, the pixel is set to 0. During subsequent extractions of data, this mask is updated using fMaskcorrector.m, called within Extract_2.m. By comparing each pixel to its four neighbours, with which it shares an edge, shown in Figure 3.5, the intensities of 'bad' pixels can be identified and removed for individual experiments. The intensities of the four pixels are averaged and the standard deviation (σ) found. If the intensity of the tested pixel lies outside of the average value $\pm \, \sigma$, it is set to 0. These faulty pixels are removed from all subsequent actions carried out in the extraction code.
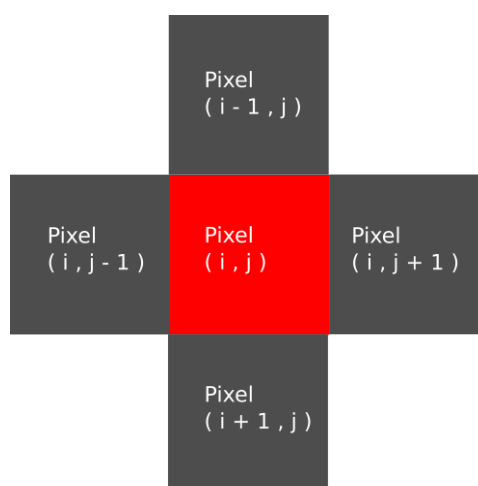
Figure 3.5 – Diagram showing the pixels compared in fMaskcorrector.m. The intensity of the central pixel (red) is compared to four edge-sharing pixels. The values i and j are the indexing values for the array of intensities in MATLAB.

Any contraction or stretching of the sample data due to an aberration in the camera, or due to non-linear optical manipulation, as is the case for the Rigaku camera's optical taper (see Section 4.3.1), cannot be accounted for using these argon corrections. The correction only allows for intensity variations between pixels to be corrected, not to account for any manipulation of the electrons or light

prior to detection. Incorrect s values are then obtained that show contraction of the data at larger s values in the image. Corrections for this can be applied using a different method as explained further in Section 4.3.

In the future, the optical taper could be fully described using a mask to cover the camera face, with a large number of holes to allow radiation, or electrons, to reach the phosphor screen and be detected. By comparing the acquired image to the known mask, a correction could be applied to the data to correct for the taper. Unfortunately, during the timescale of this work, this was not possible for the Rigaku camera and, in any case, the problems with the internal electronics of the Rigaku camera mean that it will probably not be used in the future.

3.2.1 Extraction software testing

Cyanuric chloride (Figure 3.6) was chosen as the test molecule for EDSTRACT. Previously studied,[64] the extracted intensities and resulting refinements can be compared.
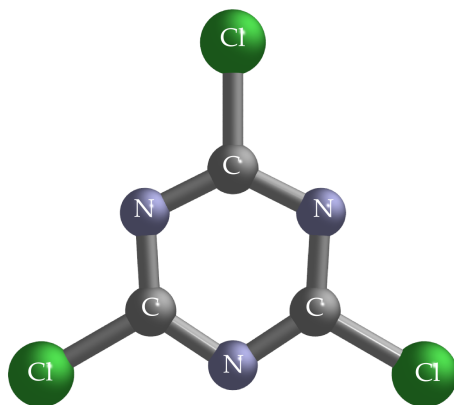
Figure 3.6 – Diagram of the structure of cyanuric chloride ($C_3N_3Cl_3$).

To test the EDSTRACT code, an image recorded several years ago, of the diffraction pattern of cyanuric chloride, using the former Edinburgh apparatus was re-analysed. The EDSTRACT extracted intensities were compared with the previously extracted intensities from xpkg.[9] Intensities extracted using

EDSTRACT matched those extracted using xpkg very well. Both extracted intensities are shown in Figure 3.7.
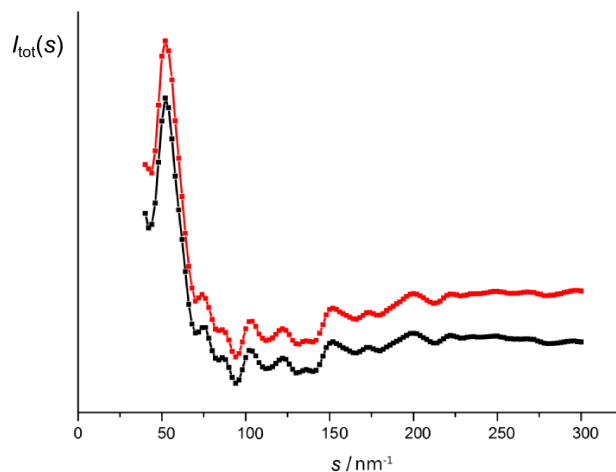
Figure 3.7 – Comparison of data extracted using xpkg (black line) and EDSTRACT (red line). Extracted intensities have been shifted in the y direction to avoid overlap and aid comparison. Data are for cyanuric chloride ($C_3N_3Cl_3$).

The extracted data were then used to refine the structure using the ed@ed refinement code, producing goodness-of-fit R values comparable to those obtained from the original refinement using xpkg extracted data.[64] This is further evidence that the extraction of data using EDSTRACT is working correctly.

The comparison only accounts for the extraction of intensities in a sample image. As data were recorded on a different apparatus using a different imaging process, it does not deal with any of the physical problems associated with the two camera assemblies used in York. The pixel size and the nozzle-to-camera distance were already known for this sample image. For the York cameras these parameters needed to be found; this work is described in Section 4.3.

3.2.2   EDSTRACT for Stingray camera assembly

As described in Section 2.3.4.2 the Stingray camera assembly samples a larger image, and the output images are rectangular of 1038×1388 pixels. The Stingray camera cannot output .raw images as are recorded using the Rigaku camera. However, the bitmap images recorded can be manipulated for use in the same way as the raw images, by combining the three colour layers of the bitmap image.

The pixel size used for the new camera assembly is 0.0501×0.0501 mm. These values have been deduced from extractions performed in Section 4.3.2.1. This pixel size is only correct for the current set-up of the camera assembly; any change in camera position will require a new calibration.

Although the sensitivity of the Stingray camera at low-light conditions is poorer than for the Rigaku camera, the intention of the apparatus remains the same. Less volatile and seeded gas beams are the intended target for this apparatus, and this and other commercially available cameras provide an alternative way of maximising the data collected. Binning of the data increases the intensities collected with an associated loss in spatial resolution. The intensities of four neighbouring pixels are combined to create a 'super pixel', shown in Figure 3.8. This allows rare events, such as higher angle scattering, to be imaged over a shorter period of time. The data for the studies reported here are collected in 2 nm^{-1} steps of s value; 2×2 binning would not adversely affect the resolution of the experiment.

Binning of data is only required if the vapour pressure of the sample gas is too low to produce a discernible diffraction image. None of the studies reported in this work have required data binning as either the samples are already volatile enough to allow a high-quality diffraction image to be collected without the need for binning. Further investigations of less volatile compounds will be aided by the use of binning, especially for samples that require heating to close to their decomposition temperatures to attain the required vapour pressure.
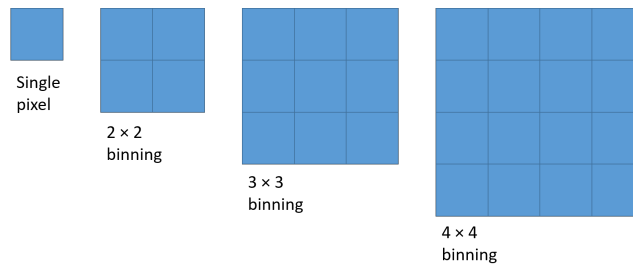
Figure 3.8 – Simple schematic of binning that could be used during image collection in the Stingray camera.

3.2.3 Overview of EDSTRACT

The extraction code has been shown to provide comparable results to those obtained from xpkg, allowing it to be used to obtain refinement quality data from GED patterns. Other benefits of the new extraction code lie in the 'openness' of the code. It is not a black box and the removal or inclusion of specific scripts to alter the handling of the data is relatively simple.

The extraction code tested and explained in this Chapter will not only serve as a tool for the extraction of data from this apparatus, but also as a starting point for extraction code further modified within the research group. The use of Matlab allows a variety of inbuilt functions and a network of other users exchanging scripts to be utilised. The availability and ease with which the code can be experimented with and adapted will allow EDSTRACT to be applicable for not only the time-averaged domain, but also the time-resolved experiments which will be undertaken within the group.

Chapter 4

Apparatus calibration

4.1 Introduction

The York GED apparatus has been part of three former PhD students work,[11, 88, 89] with improvements made to the apparatus and characterisation performed at each stage. Unfortunately, up to the start of this PhD, data of refineable quality had not been routinely produced from the apparatus. Alterations to the apparatus as part of this work, have aimed not only to improve data quality to a point where data obtained were suitable for refinement, but also to include the addition of custom nozzles, cameras and data-handling processes, such that novel GED structures could be obtained. The changes made to the apparatus, as outlined in Chapter 2, have been optimised and characterised, and are reported here.

4.2 Electron gun optimisation

Initial work carried out, using a gun set-up equivalent to that described in the theses of Hayes[11] and Fender,[88] resulted in beam widths of comparable size to those measured in their work, where full-width at half-maximum (FWHM) values of 0.76 and 0.96 mm were reported, respectively. For adequate resolution of data for structure refinement, a FWHM of approximately 0.5 mm is desirable.[28] This section explains the changes made to the gun, the justification for the changes, and results in terms of the electron beam quality.

4.2.1 Beam optimisation

To improve the focus of the electron beam, small changes have been made to the gun set-up. Several components within the gun can be moved to maximise the focus of the beam. Without significant modifications to the gun assembly the main variables are the distance between the cathode and anode (varied by the

screw handle outside of the vacuum) and the distance between the cathode and Wehnelt cap, which can be varied when assembling the gun.

At the start of this PhD the best focus was found to correspond to the limit of the screw mechanism, bringing the cathode as close as possible to the anode, which is fixed. Crucially, a global minimum in beam size was not achieved, suggesting that a better quality beam could be achieved were the cathode assembly able to be moved further forward. For this to be done the Mu-metal shield that surrounds the gun, and on which the anode is mounted, would need to be reduced in length. It was decided that this was impractical unless absolutely necessary as it could be detrimental to the overall beam quality as well as increasing the anode-to-detector distance. Other approaches to achieve a similar effect were then considered. Moving the Wehnelt cap back, relative to the cylinder, would move the point of greatest focus closer to the gun, as shown in Figure 4.1.[90]
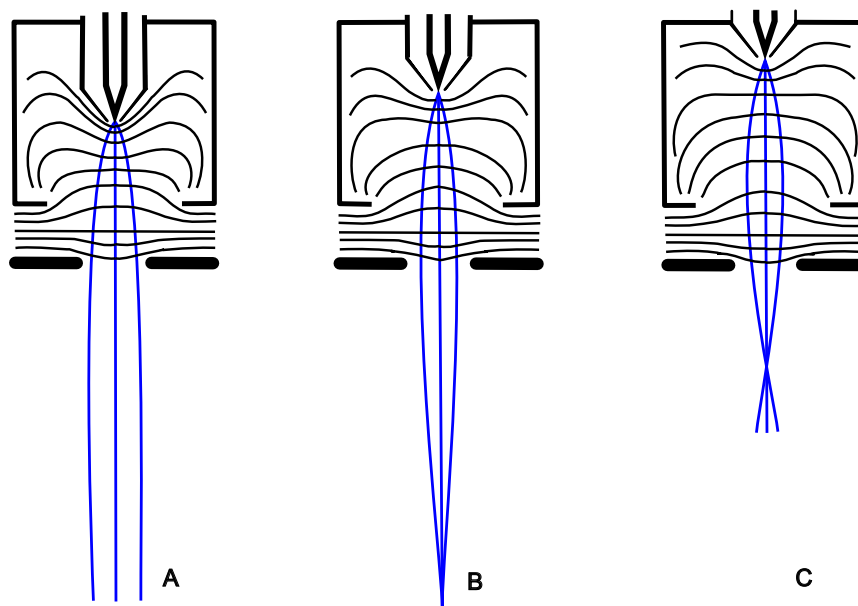
Figure 4.1 – Equipotential lines present within a telefocus electron gun, representing different distances between the Wehnelt cap and the cylinder. Image redrawn from image in Ref.[90]

This was also not an option as the Wehnelt cap has already been moved as close

as possible to the ceramic high-voltage insulator. The entire Wehnelt assembly could be moved forward, relative to the feedthrough, although this would require additional pieces to be made and tested. Instead, in an attempt to mimic the effect of moving the Wehnelt cap backwards, the filament was moved back in the Wehnelt cap leaving a distance of 0.2 mm between the filament tip and the plane of the tip of the Wehnelt cap, an increase of 0.05 mm from the previous gun set-up. This is a very small distance and can only be achieved approximately, determined using trigonometry. When the filament is 0.2 mm below the plane of the Wehnelt cap tip, it is obscured by the Wehnelt cap when viewed 300 mm from the tip horizontally and 120 mm vertically, as shown in Figure 4.2.
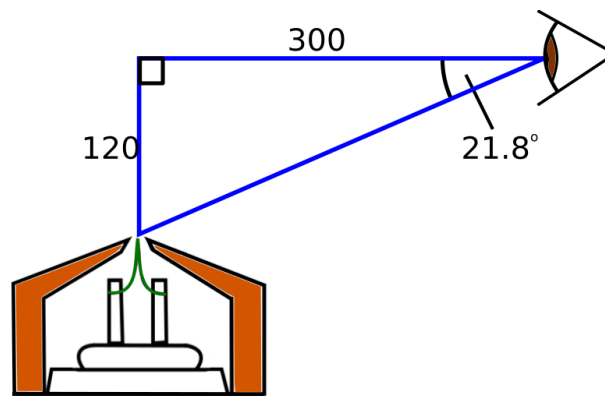
Figure 4.2 – Diagram showing the trigonometry required to correctly place the filament (green) within the Wehnelt cap (orange). All distances are in mm.

Once in place, the distance of the filament from the Wehnelt cap can be approximated by observing the bias potential (see Section 2.3.1). The further back the filament, the lower the bias required to retard the electron beam. This voltage is dependent, not only on the filament to Wehnelt cap distance, but also the Wehnelt-assembly-to-anode distance and, therefore, is quoted after the optimisation performed later in this Section.

After the filament was moved, an improvement was immediately observed with the best focus at the camera (when at a nozzle-to-camera distance of 120 mm),

being achieved nearer the midpoint of our variable anode-to-filament distance. This provides a definitive minimum for this set-up, and a greater ability to vary the focus for longer nozzle-to-camera distances, which are necessary to obtain data to refine complicated structures. As the camera is retracted, thereby increasing the nozzle-to-camera distance, the Wehnelt assembly is moved further from the anode to maintain electron beam focus.

The beam tube described in Section 2.3.1 is used in the optimisation of the electron beam. The presence of the collars allows the steering and alignment of the beam to be performed more simply and quickly as any beam aligned through the tube will be roughly positioned at the centre of the camera. Also, the full beam current produced from the gun can be measured at the collar, and this value is needed when calculating the FWHM of the electron beam reaching the detector.

The beam stop at the detector (Figure 4.3) functions as both a measure of the current of the electron beam and as a shield for the camera. High beam currents, of which this gun is capable, can damage the phosphor screen or obscure intensity rings at wider scattering angles by high intensities of electrons saturating the camera at narrow scattering angles. The beam stop, as its name suggests, stops the beam from reaching the phosphor, thus preventing damage. The undiffracted incident beam strikes a copper Faraday cup located in the centre of the beam stop. Only the copper Faraday cup is electrically isolated from the rest of the beam stop and by extension the earthed apparatus. Any electrons hitting this cup are detectable as a current; a wire passing through a vacuum feedthrough carries this current to a picoammeter (Keithley 610C), which detects the current reaching the Faraday cup. By comparing the current at the Faraday cup to the full beam current detected at the beam collar, the beam size is determined. A full schematic and more in-depth description of the beam stop can be found in the thesis of Hayes.[11] A deep removable cup is placed in front of the Faraday cup, which contains a 0.5 mm aperture. The deep cup allows greater beam intensities to be used. High numbers of electrons can overwhelm the Faraday cup alone, resulting in a larger background being detected, which thereby reduces data quality. The

larger cup presents a larger surface area and volume preventing electrons from escaping and being detected. Only electrons travelling straight through the aperture can be detected as a current at the Faraday cup; any electrons striking the aluminium cup will flow to earth.
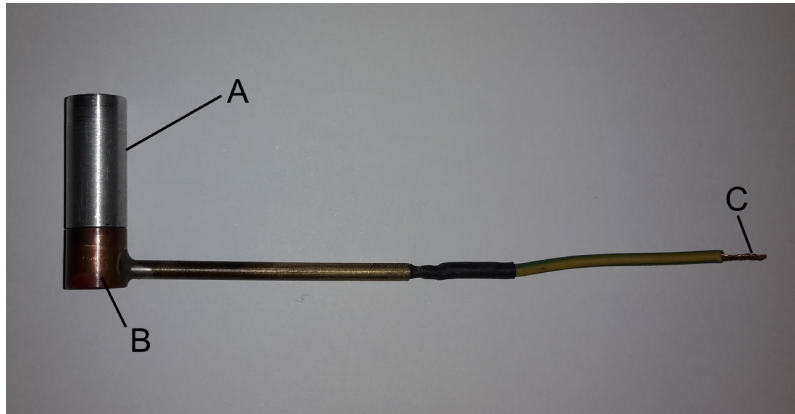
Figure 4.3 – Photograph of the beam stop used to characterise the electron beam within the time-averaged York GED apparatus. The beam stop consists of a deep aluminium beam cup (A), a copper Faraday cup within the beam stop (B) and a copper wire carrying the collected current to be measured (C).

Maximising the ratio of the beam current detected at the Faraday cup to the full beam current detected at the beam collar gives the optimum focussing. The distance between the cathode and anode was varied using the screw focus, and the beam stop scanned in a 2-D grid perpendicular to the beam to capture the largest current at the Faraday cup. The distance that the Wehnelt assembly has been moved relative to the anode was measured using callipers, and all distances are relative to the maximum extent of the screw (minimum distance obtainable between the anode and cathode).

At each distance the beam intensity was initially recorded at the beam collar, using the steering plates to deviate the beam to strike the collar. The beam collar has a sufficiently large area that the full electron beam can be detected. The steering plates are then returned to the deflecting potentials where the beam passes through the collar, allowing detection at the beam stop. Figures 4.4 and

4.5 show the FWHM detected at each focus, for nozzle-to-camera distances of 120, 170, and 270 mm, at 0.1 μA and 1.0 μA, respectively.
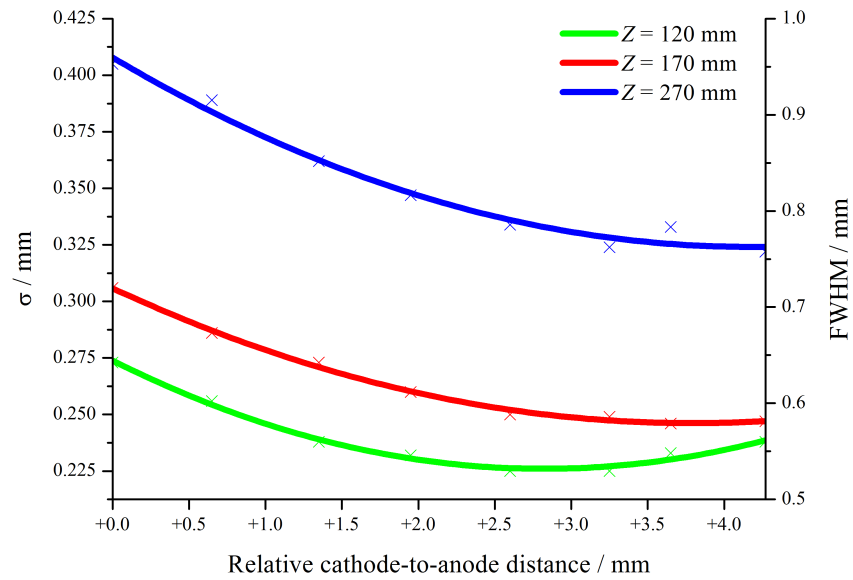
Figure 4.4 – The standard deviation (σ) and FWHM of the 0.1 μA electron beam recorded at nozzle-to-camera distances of 120, 170 and 270 mm.
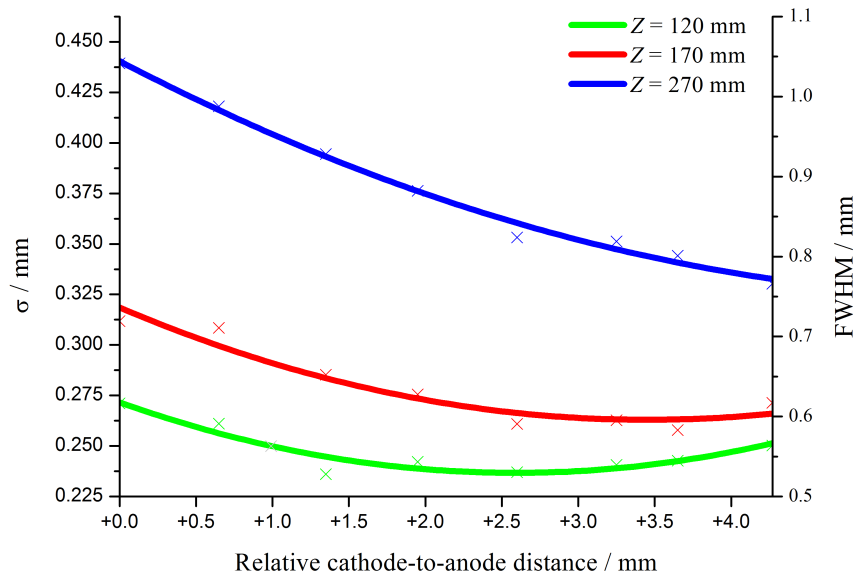
Figure 4.5 – The standard deviation (σ) and FWHM of the 1.0 μA electron beam recorded at nozzle-to-camera distances of 120, 170 and 270 mm.

Figure 4.4 shows that the optimum focus FWHM is 0.53 mm for 0.1 μA at a 120 mm nozzle-to-camera distance; this was achieved at a distance, between the Wehnelt assembly and anode, that was 3 mm shorter than the maximum achievable distance. It is worth noting that this distance only applies to this specific filament set-up, so changing the filament requires finding the optimum focussing again. The bias potential required to produce 0.1 μA at the optimum focus was 72 V, which should serve as a guide for future replacement of the filament.

After beam focussing had been completed, the wire carrying current from the Faraday cup to the ammeter was changed as the quality of the earth and the presence of multiple joins had led to a leaking of charge, artificially reducing the current detected. As the quality of the focus is determined by comparison of the beam charge at the collar and charge detected through the aperture at beam stop, the best focus is still valid; however, previous beam characterisation work[11, 88] may have overestimated the FWHM.

106

The calculation of a FWHM beam size is performed assuming that the beam profile is Gaussian in shape, a valid assumption as shown in Figure 4.6. Beam FWHMs have been determined for beam currents of 0.1, 1.0 and 10 μA, with full beam profiles carried out at 0.1 and 1.0 μA, shown in Figures 4.7 and 4.8, respectively. A full beam profile was not carried out for the 10 μA beam as even a portion of that beam reaching the phosphor screen could cause damage. To minimise damage to the phosphor screen during a data collection, the beam was centred at the beam stop using a lower current and then turned up to the higher currents.

Equation 4.1 describes the current that would be collected up to radius r when a beam is Gaussian in shape. The standard deviation of the electron-beam intensity, σ, is calculated using Equation 4.2:

$$I = \frac{I_{\text{tot}}}{2\pi\sigma^2} \exp\left(-\frac{r^2}{2\sigma^2}\right) \quad , \tag{4.1}$$

$$\sigma = R\left[-2\log\left(1 - \frac{I}{I_{\text{tot}}}\right)\right]^{-\frac{1}{2}} \quad , \tag{4.2}$$

where I and I_{tot} are the currents recorded at the Faraday cup and beam collar, respectively. R is the size of the aperture, which was 0.5 mm in this work. Equation 4.1 can be rewritten for when the ratio between I and I_{tot} is equal to 0.5, in terms of σ and FWHM, shown in Equation 4.3:

$$\frac{I}{I_{\text{tot}}} = \frac{1}{2} = \exp\left(-\frac{r_{\text{HM}}^2}{2\sigma^2}\right) = \exp\left(-\frac{[\frac{\text{FWHM}}{2}]^2}{2\sigma^2}\right) \quad , \tag{4.3}$$

where the final value of FWHM is:

$$\text{FWHM} = 2\sigma\sqrt{-2\ln(0.5)} = 2.355\sigma \quad , \tag{4.4}$$

and r_{HM} is the radius at half the maximum intensity.

The beam collected shows a Gaussian distribution about the centre; the electron beam is both small enough in space, and sufficiently symmetric for diffraction experiments to be possible.
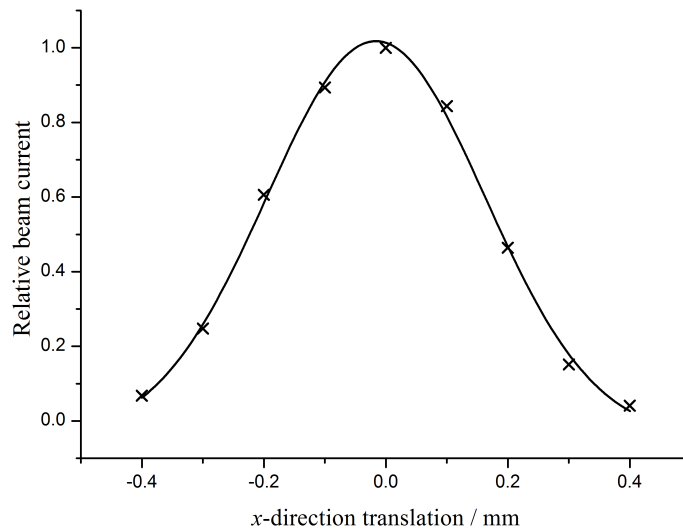
Figure 4.6 – A 2-D profile in the x direction of the 0.1 μA electron beam at a nozzle-to-camera distance of 120 mm. A Gaussian curve has been fitted to the data with a 99.6% fit. Beam intensities have been normalised relative to the highest recorded intensity.
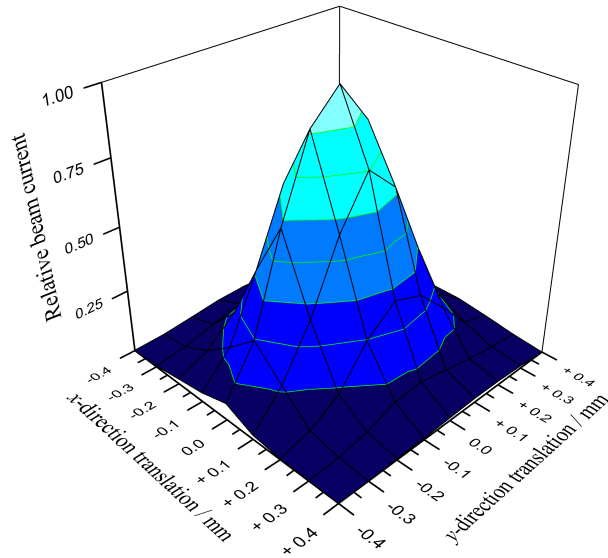
Figure 4.7 – A 3-D profile of the 0.1 μA electron beam at a nozzle-to-camera distance of approximately 120 mm. Beam intensities have been normalised relative to the highest recorded intensity.
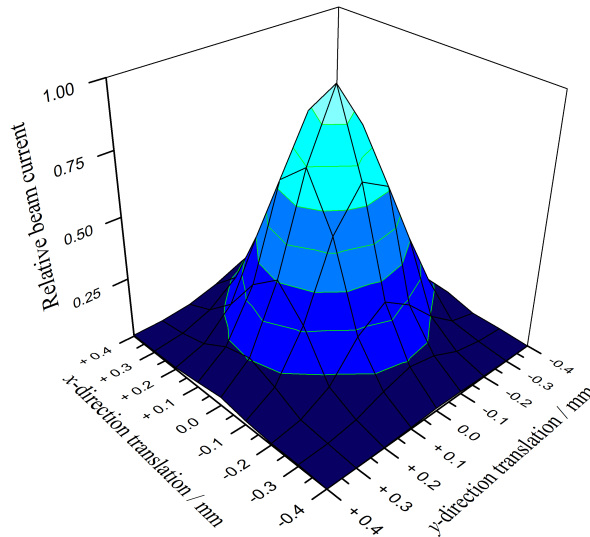
Figure 4.8 – A 3-D profile of the 1.0 μA electron beam at a nozzle-to-camera distance of approximately 120 mm. Beam intensities have been normalised relative to the highest recorded intensity.

Table 4.1 – FWHM values for beam currents at a nozzle-to-camera distance of 120 mm, for a beam accelerating potential of 35 kV. I_{tot} and I are the current collected at the beam collar, and Faraday cup, respectively.

I_{tot} / μA	I / μA	FWHM / mm
0.1	0.066	0.401
1.0	0.643	0.410
10.0	5.61	0.459

Electrons, due to their negative charges, will repel one another when close in space. As the intensity of an electron beam increases so will the charge density. Larger charge densities accelerated over the same potential will result in larger beam widths being observed at the point of diffraction. This can be seen in the FWHM values recorded here. When carrying out experiments, the goal is to use the minimum beam current to collect an acceptable diffraction pattern. Beam currents as high as 10 μA can be produced whilst still maintaining an acceptable beam width. Although this is not necessary for any of the experiments carried out in this work, it provides the opportunity to study less volatile species introduced through an effusive nozzle and also to study seeded gas beams, as used in supersonic expansion nozzle assemblies, containing relatively low concentrations of species of interest.

4.3   Camera testing

As explained in Section 2.3.4, two different camera assemblies have been used in this work. Each has been tested to ensure that data collected are accurate and suitable for refinement.

4.3.1 Rigaku CCD assembly

Data collected by a previous PhD student, using the Rigaku CCD camera,[11] showed an apparent contraction of the data at larger scattering angles. It was initially believed that a failure in the experimental set-up was the cause of this contraction, with excessive electron beam width, multiple scattering of sample along the beam line, or unsuitable sample introduction cited as possible causes. During my PhD work, all of these theories have been tested and found either to have no appreciable effect, or that any improvement led to changes in data that were distinct from the contraction observed.

After the optimisation of the electron beam, a return to a traditional nozzle set-up as used in other GED apparatus, and the introduction of a cold trap, the data collected with the Rigaku camera still showed the aforementioned contraction at larger s values. The conclusion, therefore, was that the contraction must be caused either by the camera assembly or by the extraction of data from the diffraction images. As the extraction code has been shown to be functioning correctly (Section 3.2.1) the error must come from the camera. The contraction of the data could be due to either a physical misalignment between the phosphor screen and CCD chip, or an incorrect set of camera parameters used in the data extraction. Reported within this Section is the testing of the experimental variables within the data extraction of images recorded using the Rigaku camera.

4.3.1.1 Pixel-size testing

The optical taper connecting the phosphor screen and CCD chip within the camera has a published value of 3.17.[11] This value denotes the multiplicative increase in size of the observed pixel size from the CCD chip to the phosphor screen. The CCD chip has a square pixel width of 0.024 mm, meaning an effective pixel width of 0.076 mm at the phosphor screen. For the testing performed in this chapter for the Rigaku camera has used data collected for tetrahedral carbon

tetrachloride (CCl_4). Data were extracted using a number of different assumed pixel sizes and the resulting scattering intensity curves were refined using ed@ed (Figure 4.9). For all of these extractions, the nozzle-to-camera distance was 130 mm, and the electron wavelength was 6.45 pm. Although a minimum is not seen in Figure 4.9, the refined central carbon to chlorine (C−Cl) bond distance decreased markedly in comparison to experimental values[18] as the pixel size was increased, as shown in Figure 4.10. The C−Cl bond length of 173.9(1) pm, from the refinement at a pixel size of 0.0744 mm, is already far smaller than the electron diffraction bond length of 176.4(2) pm.[18] The goodness-of-fit R factors for the refinements decrease as the pixel size is increased; however, even the best fit achieved (pixel size of 0.0744 mm) shows significant contraction of the data at larger s values. The molecular intensity curve for the best refinement is shown in Figure 4.11.
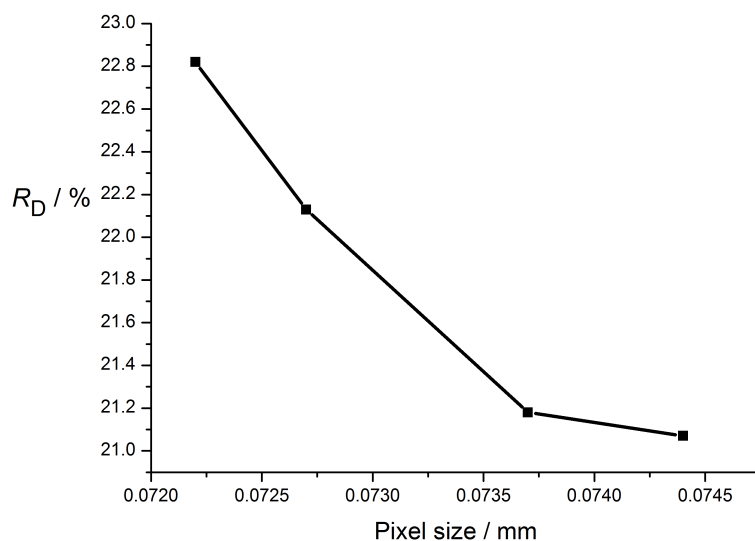
Figure 4.9 – R factors obtained from refinement of experimental intensities extracted using different assumed values of pixel size. Data presented are for carbon tetrachloride (CCl_4).
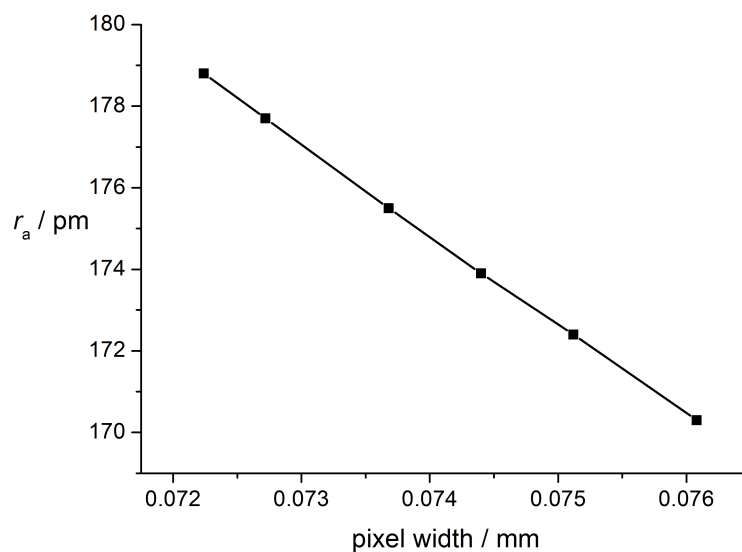
Figure 4.10 – Variation in refined C−Cl bond length in CCl_4 at different pixel sizes.
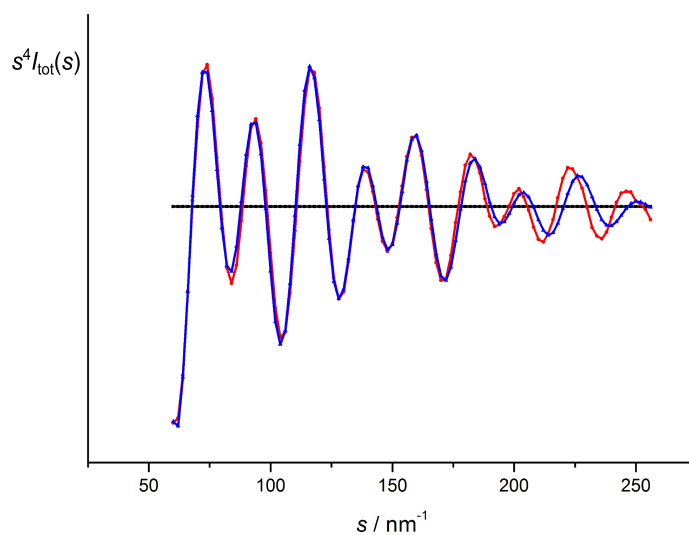
Figure 4.11 – Experimental (red) and refined theoretical (blue) molecular intensity curves for refined CCl_4 data recorded using the Rigaku camera. Extracted data intensities are for a pixel size of 0.0744 mm.

4.3.1.2 Electron wavelength testing

The electron wavelength is the only variable investigated in this chapter that scales linearly with the s value, as shown in Equation 1.3. Varying the wavelength used in the data extraction did allow a more comparable MIC to be produced and, as a result, a lower R factor to be obtained. Unfortunately, the change in wavelength required to obtain the best fit was too long to be considered plausible. If the electron wavelength is far from the theoretical value corresponding to the accelerating potential displayed at the electron gun, then the use of another camera as the data collection medium should also show the same contraction of data; as explained later in Section 4.3.2, the Stingray camera assembly did not show this.

4.3.1.3 Nozzle-to-camera distance testing

In addition to varying the pixel size, the nozzle-to-camera distance, which was physically measured to be close to 120 mm for the data discussed earlier, was also varied. Once again, although the R factors for the refinements decreased, the data continued to look contracted, limiting the R factors to 0.15 and above. When the nozzle-to-camera distance was varied in conjunction with the pixel size the contraction remained; although a lower R factor was achieved, this was only possible by extracting the data using unrealistic values for each parameter.

Following improvements made to the apparatus, and as a result of the testing of the experimental variables that directly affect the molecular intensity curves produced, it was decided that the source of the data contraction observed both in this work, and in the work of Hayes,[11] was a non-linear scaling between the phosphor screen, upon which the electrons are incident, and the CCD chip recording the scattering intensities. The magnitude of this discrepancy could not be adequately resolved, and so a new camera assembly was designed and built.

4.3.2   Custom Stingray CCD assembly

The original design of the Stingray camera assembly did not include an optical filter to account for the rapid decrease in scattering intensity with diffraction angle. It was instead hoped that the limitless data acquisition possible using the camera would allow the stacking of images, revealing faint data at larger s values without the saturation of the camera at smaller s values. Data were recorded at a nozzle-to-camera distance of 140 mm. The images were recorded for 2 s as the camera became saturated with longer exposure. To try and extract the data to allow its use in a refinement and to display any data that could be present in the image at larger scattering angles, 100 argon images were also recorded with the same experimental conditions. The scattering intensities extracted from the image (Shown in Figure 4.12), corrected using the stacked argon image and associated scattering factors, were low quality at s values greater than 150 nm^{-1}.
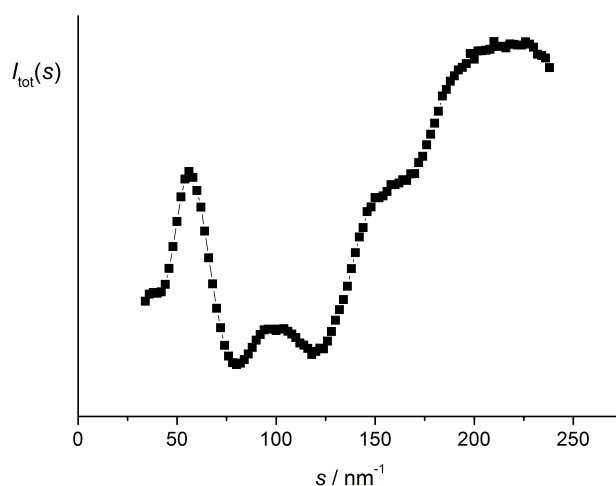
Figure 4.12 – Extracted scattering intensities for benzene, recorded using the custom camera assembly without an optical filter. Extraction carried out from a stacked image of 100, 2 s exposure images.

Unfortunately stacking of n images of exposure time t does not produce the same intensities as an image with exposure time $n \times t$. As a result, for data of refineable

115

quality to be recorded, the cumulative exposure time needs to be far longer. A lens and CCD pairing has been shown to be less sensitive than an optical taper and CCD pairing,[98] and the same is seen here. The Stingray camera assembly is approximately 20 times less sensitive than the Rigaku camera assembly, requiring far longer exposure times to record a diffraction pattern. If this is compounded by the need to record the hundreds of images necessary when not using an optical filter, samples with limited availability, such as new compounds produced by synthetic chemists, become unsuitable for study.

The images extracted from the Rigaku camera assembly, treated using an argon image collected under the same experimental conditions, showed that high-quality intensities could be collected using an optical filter, despite the other problems faced by that camera. An optical filter was, therefore, added to the custom camera assembly, and further data collected. Data are now recorded at far larger s values, and are suitable for refinement. The argon data account well for the optical filter, producing an uphill curve (Shown in Figure 4.13) comparable to those seen from images acquired using the former Edinburgh apparatus. The size of the new camera face is comparable to that of the Rigaku camera, and the images, once extracted, do not appear to show the same contraction in the data, as was the case for the Rigaku camera. The extracted uphill curve, containing both molecular and atomic scattering, is compared with a theoretical MIC for benzene in Figure 4.13. The extracted curve displays good agreement in terms of s value with the theoretical MIC.
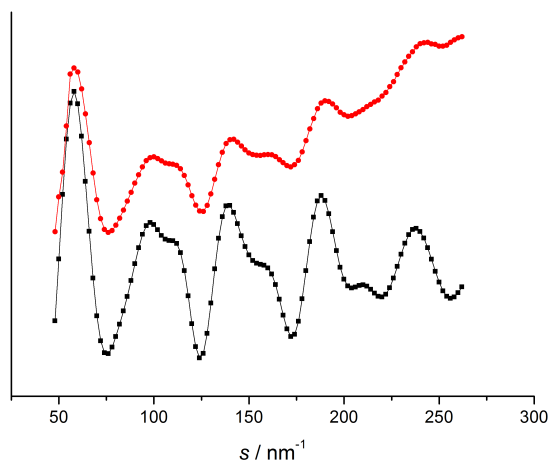
Figure 4.13 – Comparison of the scattering intensities extracted from data collected using the Stingray camera assembly with an optical filter (red) and theoretical scattering intensities of benzene (black). Experimental scattering intensities are corrected using an experimental argon image and the associated scattering factors.

4.3.2.1   Pixel-size testing of Stingray camera assembly

The nature of the custom camera assembly is such that the pixel size can vary depending upon the distance between the camera and the phosphor screen. As shown in Figure 2.20, the camera can be moved on the runner within the vacuum-tight tube, and was positioned so that the greatest amount of the phosphor screen could be visualised. Rough calculations suggested that the pixel size is approximately 0.05 mm. When comparison of the beam-stop size to the size of the visible edge of the phosphor screen was carried out, the pixel size was determined to be 0.048 mm. The measured nozzle-to-camera distance for all data in this section is 145 mm. The pixel size was scaled until the best visual fit to the theoretical benzene scattering was obtained. The pixel size that best fitted the theoretical data was 0.0515 mm. This is larger than expected and suggested a problem may exist in the data.

117

4.3.3 Corrections for Stingray camera assembly

After the testing outlined previously, the images acquired were still insufficient in quality for refinement. Data collected at nozzle-to-camera distances of approximately 140 and 250 mm refined well individually, producing the calibration benzene C−C bonded distance of 139.75 pm[99] when data extracted at nozzle-to-camera distances of 141.07 and 247.49 mm respectively. The manipulator used to move the camera has an uncertainty in the distance of $\pm$ 0.1 mm, therefore the calibrated distance for each of these data collections should be separated by 110 $\pm$ 0.2 mm if the data are correct. This is not the case, confirming that a problem in the data exists. One possible reason for this has been investigated, and is described in this Section.

The Stingray camera assembly utilises a CCD camera paired with a lens. This lens, like all lenses, has a focal aberration, distorting the image. This is similar to the failing in the Rigaku camera; however, testing of the lens to obtain an acceptable correction is more easily performed for this assembly. The ability to disassemble the components, removing parts of the assembly to more easily image a known pattern, allows a correction to the camera assembly to be obtained.

Figure 4.14 shows the known pattern used in the calibration process. Images were recorded of this pattern placed in the same position as the phosphor screen. An image was captured, with the centre of the calibration pattern kept as close to the centre as possible [approximately pixel (706, 523)]. The comparison of the captured image to the known image is shown in Figure 4.15. It can be seen that the camera image is contracted at the extremes of the image. The pixel size was then scaled in an attempt to match the two, but the patterns could not be matched this way, confirming the presence of a barrel distortion.
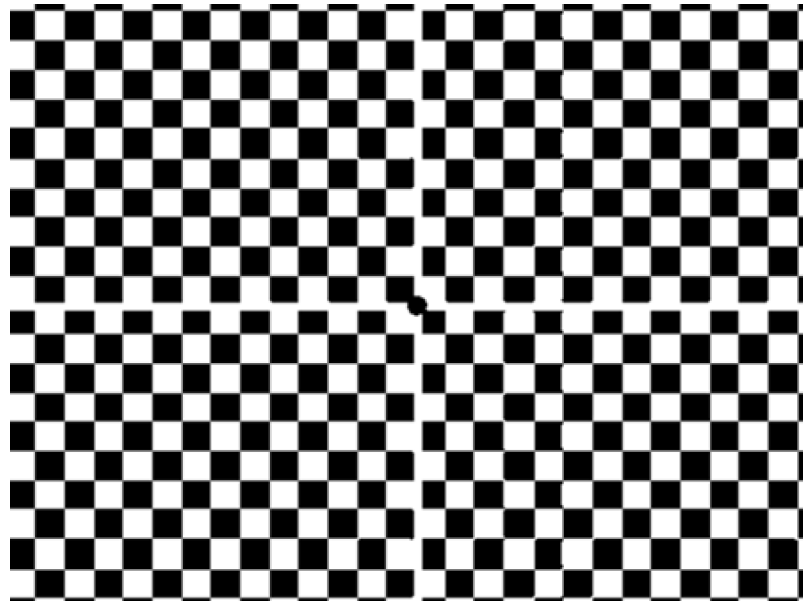
Figure 4.14 – The known pattern used to calibrate the Stingray camera assembly.

A piece of custom code[100] (Appendix B) was used to alter the collected image, effectively flattening the barrel distortion. Correction 2 within the code yielded the best match between the calibration and corrected images. Figure 4.16 shows the calibration image overlaid with the corrected image. Correction 2 uses Equation 4.5 to correct radially distorted images:

$$r_1 = r \left[\frac{1}{(1+k)\, r^2} \right] \quad , \tag{4.5}$$

where r_1 is the corrected distance from the centre of the image, produced from the original distance, r. The k value was varied until the best fit to the data was seen. The correction applied gave the best fit with $k = 0.0125$. This correction procedure will need to be repeated every time the camera is moved in the assembly.
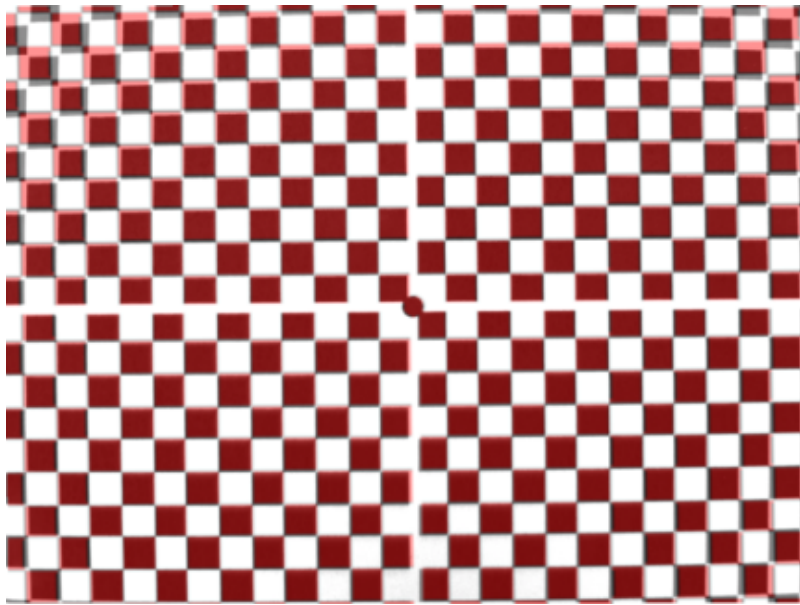
Figure 4.15 – The image captured using the Stingray camera assembly (black) overlaid with the known pattern (red).
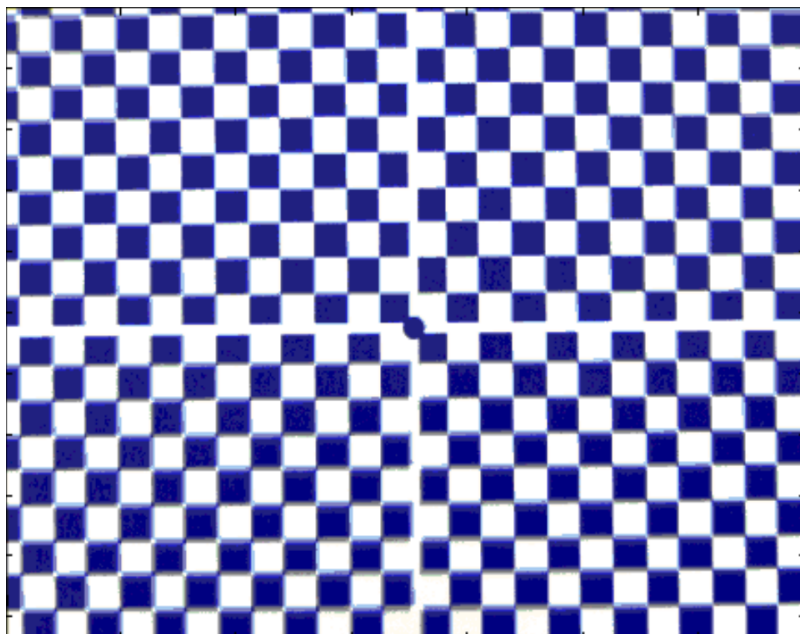
Figure 4.16 – Comparison of the calibration image with the corrected image. Corrected image (solid blue) overlaid with the calibration image (light blue).

Diffraction patterns for benzene were now re-extracted using EDSTRACT including the barrel distortion correction and refined using ed@ed. The calibrated distances are now 140.33 and 250.59 mm, very close to the 110.0 $\pm$ 0.2 mm difference expected. The RDC from the refinement using two data sets is shown in Figure 4.17. The final R factors for this refinement are R_{G} = 0.18 (R_{D} = 0.12), with a final bonded $C-C$ distance of 139.6(1) pm. The disparity between the refined distance here and the GED derived experimental values used to calibrate, 139.75(1) pm,[99] shows that the data quality is still not acceptable for publishable refinement; however, the data are an improvement over previous data recorded on this apparatus. Unfortunately, within the time scale of this work, further improvement to the data quality was not possible, but the custom camera assembly will yield high quality data, if calibration for the lens correction can be improved using a better calibration image.

Figures 4.18 and 4.19 show the molecular intensity curves from the corrected benzene refinements. Although the agreement between the theoretical and experimental curves in terms of s value is good, the overall fit of the data is not perfect. Experimental data collected at the longer nozzle-to-camera distance appear slightly more stretched at the extremes of the camera, a result of the slight failure in the correction applied. As the radius of the camera face is the same for both the short and long nozzle-to-camera distances, the smaller s range sampled in the long data set is affected to a greater extent by the lensing effect. Further data acquisition with improvements to the data collection will improve this fit. The data used in this refinement were collected over a short timescale with limited ability to maximise the quality of the collected data.

As shown in Table 4.2, the $C-C$ distance obtained from the refinement is only just out with the calculated error and is a great improvement over the uncorrected images. The problem that still persists is due to the calibration image used. The large size of the squares makes comparison at a large number of points difficult; appearing to fit when actually still incorrectly lensed.
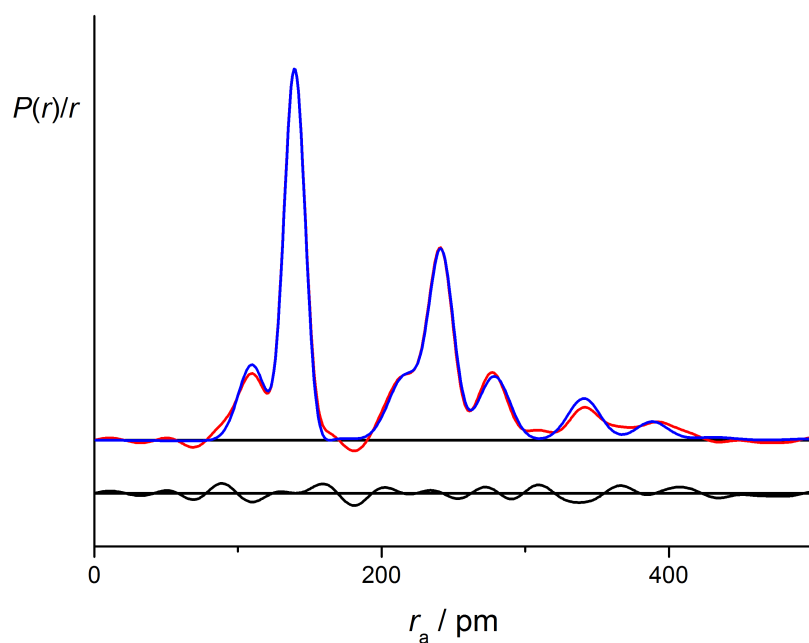
Figure 4.17 – Experimental (red), theoretical (blue), and difference (experimental-minus-theoretical, black) radial distribution curves, from the GED refinement of the corrected benzene data using the Stingray camera assembly. Before Fourier inversion, data were multiplied by $s \exp\left(\frac{-0.00002 s^2}{(Z_C - f_C)(Z_H - f_H)}\right)$.
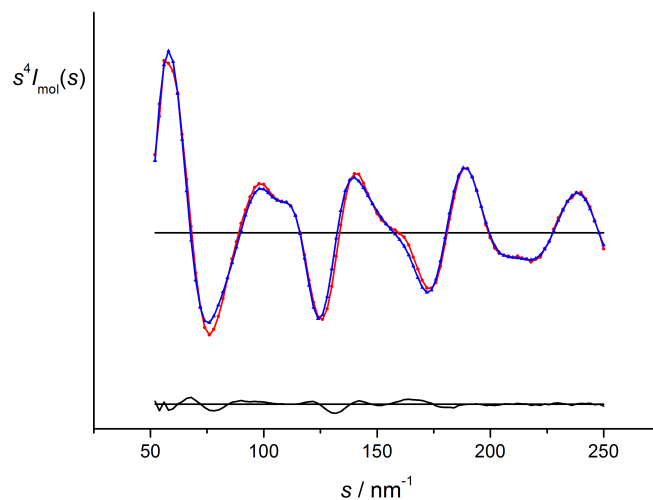
Figure 4.18 – Experimental (red), theoretical (blue), and difference (experimental-minus-theoretical, black) molecular intensity curves collected at a nozzle-to-camera distance of 140.33 mm, using the Stingray camera assembly and image correction.
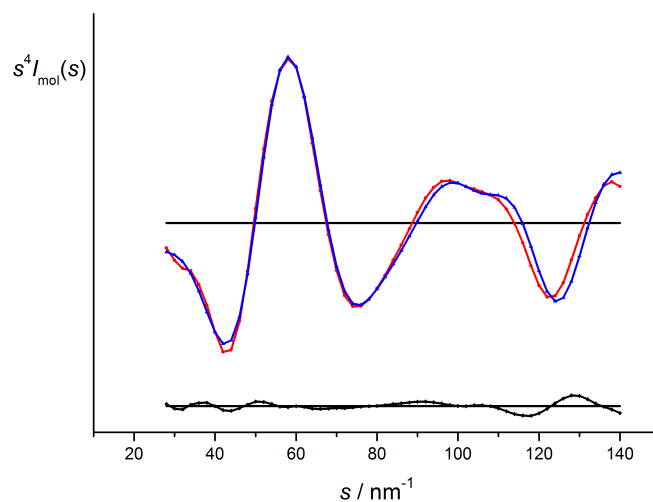
Figure 4.19 – Experimental (red), theoretical (blue), and difference (experimental-minus-theoretical, black) molecular intensity curves collected at a nozzle-to-camera distance of 250.59 mm, using the Stingray camera assembly and image correction.

Table 4.2 – Experimental and reference geometric parameters for benzene. Tabulated values are in picometers.

Parameter	r_a	$r_a{}^{99}$
C$-$C	139.6(1)	139.75(1)
C$-$H	110.8(8)	109.90(3)

Table 4.3 – Experimental and quantum-chemically calculated geometric parameters and amplitudes of vibration, u, for benzene. Calculated values obtained at the B3LYP/cc-pVTZ level. Tabulated values are in picometers.

Amplitude	r_a	u value	Calculated u^{99}
C$-$H	110.3(8)	9.3(14)	7.6
C$-$C	139.5(1)	4.5(4)	4.5
C$\ldots$H *ortho*	216.9(6)	9.0(10)	9.8
C$\ldots$C *meta*	241.6(2)	6.4(4)	5.4
C$\ldots$C *para*	278.7(2)	8.8(7)	6.1
C$\ldots$H *meta*	341.1(7)	11.4(7)	9.4
C$\ldots$H *para*	388.7(8)	9.4(8)	9.3

The work of Hayes[11] to calibrate the York time-averaged apparatus produced refinements in which the bonded parameters were comparable to literature values, but only when the amplitudes of vibration were around twice as large as expected. As shown in Table 4.3, this is not seen in these refinements, where the amplitudes of vibration are all close to calculated values and lie within 3 standard deviations. The full output from this benzene refinement can be found in Appendix D.

Chapter 5

Ab initio molecular dynamics vibrational corrections

5.1   Introduction

To characterise fully a complex structure from GED data requires the combination of both theoretical and experimental data. As explained in Section 1.4, vibrational corrections are required to approximate an equilibrium structure from GED data; this is routinely done using force constants calculated for the equilibrium structure, extrapolated using a program called SHRINK.[101] Without the corrections, the experimental GED data yield a vibrationally averaged structure, which cannot be meaningfully compared with theoretical structures or with other experimentally derived structures.

In this Chapter I present an approach to calculating these distance corrections using molecular dynamics (MD) to simulate the vibrations of the molecule. By comparing these simulations to an *ab initio* calculation of the equilibrium structure of the molecule, corrections can be applied to every internuclear distance in the molecule. The motivation for this approach is the complete sampling of the molecular motion, allowing applicable corrections to be calculated for anharmonic motions that are badly described by the standard approach using SHRINK. For most molecules studied the standard approach works well; however, in the presence of large-amplitude or anharmonic motions, such as the breathing modes of silsesquioxanes,[17] the description becomes unsatisfactory.

Previous attempts to use MD to produce vibrational corrections using classical mechanics neglect quantum effects, particularly important in the consideration of light atoms, resulting in an underestimation of distance corrections. Path-integral molecular dynamics (PIMD),[102, 103] was shown to not only provide high quality corrections, but also to account for quantum effects,[64] and is used as the comparison here. The approach outlined in this Chapter, utilising Gaussian 09[61] *ab initio* TD-DFT calculations to calculate the force constants at each time step, coupled to the Newton-X MD package to propagate the molecular trajectory, intends to provide comparable quality corrections to the PIMD approach but in a

simpler to use and less computationally demanding way.

5.2 Vibrational corrections theory

As mentioned in Section 1.4, the desired structure obtained from any structural technique is the equilibrium structure (r_e), a theoretical vibrationless state at the minimum of the potential-energy surface (PES). This structure allows comparison between different structural methods and experiments, as any structure is independent of experimental variables such as temperature. It also means that experimental structures are directly comparable to structures calculated using *ab initio* methods.

To understand the nature of the corrections required, we must first understand the structural distances measured. GED determined distances (r_a), shown in Equation 5.1, are vibrationally averaged over the time of the experiment. Formally, r_a is the inverse of the average inverse of the interatomic distance (r):

$$r_a = \left\langle r^{-1} \right\rangle^{-1} \quad . \tag{5.1}$$

As the intended distance is r_e, and the GED experimental distance is r_a, the correction can be expressed as the difference between these two distances, shown in Equation 5.2. The Root-Mean-Squared (RMS) amplitude of vibration between two atoms is denoted u, while k is the correction for a vibration perpendicular to that interatomic bond vector, and is responsible for 'shrinkage'. The correction for the centrifugal distortion due to the rotation of the molecule is δr, and δA is the correction due to anharmonicity within the molecular vibration:

$$r_e - r_a \approx \frac{u^2}{r_a} - k - \delta A - \delta r \quad . \tag{5.2}$$

Equation 5.2 is only the approximate correction. For the full correction u would be divided by r_e; but this is not known exactly. The distance r_a is used as this is comparable, and the variation between r_e and r_a does not affect the correction to any great extent.

The r_{h1} corrected distance is the best calculated correction based on a harmonic oscillator. The variety of corrections that have been applied to GED data can be categorised by which constituents of the correction are approximated, and the approach to each correction. Equations 5.3 and 5.4 describe the process for obtaining the vibrationally averaged distance (r_g), and the distance obtained by accounting for perpendicular vibrational corrections using a curvilinear correction calculated using SHRINK (r_{h1}), respectively:

$$r_g = \langle r \rangle \approx r_a + \frac{u^2}{r_a} \quad , \tag{5.3}$$

$$r_{h1} \approx r_a + \frac{u^2}{r_a} - k_{h1} \quad . \tag{5.4}$$

These distances are systematic improvements to the distance obtained from GED data, requiring extrapolation from *ab initio* calculations of a stationary equilibrium geometry and its associated vibrations. The majority of structures refined in the last few years have been refined at the r_{h1} level, using a harmonic approximation to provide a first-order curvilinear correction for the shrinkage effect outlined in Section 1.4.

As mentioned earlier, to describe more accurately anharmonic movements from a theoretical approach requires a calculation that takes into account anharmonicity in vibration. A cubic frequency calculation needs to be performed. Unfortunately this approach has a couple of drawbacks: scaling of the cubic calculation to larger, more complex structures is poor, making calculations for many molecules

prohibitively long, and only a small amount of anharmonicity along the bond can be taken into account without the need for higher-order potentials to be used.

Molecular dynamics propagates molecular motion trajectories over a set time period. This is directly comparable to a time-averaged GED experiment, which probes the molecule throughout the data collection time, and so MD can be used to calculate corrections to apply to experimental data to approximate an equilibrium structure. As the MD simulation samples movement of the atoms in the molecule, it can implicitly model all potential motion of the molecule producing a more complete correction for the GED refinement.

5.3   Molecular dynamics in Newton-X

The freely available Newton-X[104, 105] code has been developed to calculate non-adiabatic molecular dynamics for excited-state species; however, standard adiabatic approximation molecular dynamics of ground-state species can be carried out as well, and is used here. For the vibrational corrections to be applicable, a large number of steps in the ground state of the molecule must be sampled with the average positions of the atoms calculated. Distances calculated using these positions are a theoretical equivalent of r_a and can be compared to the equilibrium distances (r_e) determined from *ab initio* geometry optimisations to determine a correction to be applied to each distance in the refinement. A flowchart of the Newton-X molecular dynamics method is shown in Figure 5.1.
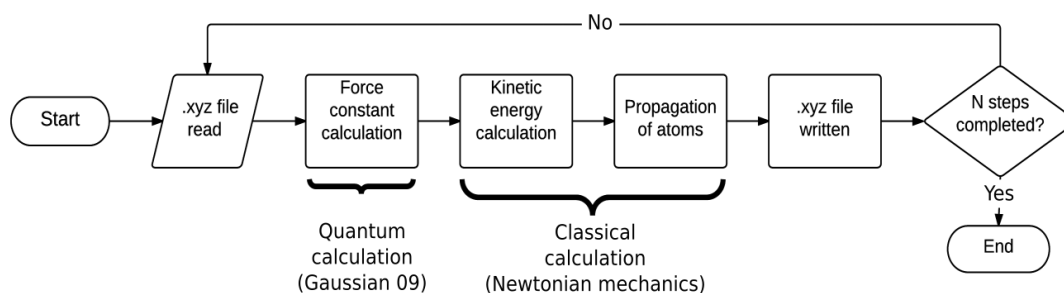
Figure 5.1 – Simple flowchart to illustrate the steps used in Newton-X to simulate molecular dynamics.

For the MD simulation a number of steps, N, is chosen to give a simulation duration sufficient to sample movement of the molecule to support the assumption that the time-averaged results of the simulation are equivalent to an ensemble average. For the simulations in this work, a minimum of 5 ps is sampled. The time-step chosen depends on the molecule being studied, and for all simulation undertaken in this work is the default in Newton-X calculations, 0.5 fs; this was chosen as it is approximately 15 times shorter than the period of the highest frequency interatomic vibration in this molecule.

Newton-X propagates the atoms using forces calculated in a single-point TD-DFT calculation at each time-step. The movement of the atoms is treated classically, a potential problem when treating low-mass, high-frequency vibrations such as $C-H$ bonded distances. The potential for quantum tunnelling to occur is higher for these vibrations, having an appreciable effect on the distance correction needing applied. This effect on interatomic distance is explained in further detail in the work of Wann *et al.*[17,64] For the study outlined here, a rigid molecule containing no light atoms is used to show the general applicability of the Newton-X MD simulations as an alternative to SHRINK.

Any MD simulation requires a number of variables to be set, such as the temperature (T) and the time-step (δt). The temperature is set to the temperature of the experiment for which it will become the comparison. MD at constant

temperature is the intention; however, for a single isolated molecule there exists nothing with which to collide to provide temperature to the system. Many approaches have been used to tackle this problem: theoretical heated baths into which the molecule is submerged so as to maintain the temperature, as well as more local heating techniques.

One of the main advantages of the Newton-X MD approach is the scaling in computational time for larger, more complex molecules. For example, MD simulations have been run both for cyanuric chloride and 4-(dimethylamino)benzonitrile (DMABN), which are composed of 9 and 21 atoms, respectively. The calculations for DMABN took around three times as long as those for cyanuric chloride using the same basis set and level of theory. As the majority of molecules that will require a more anharmonic description of their atomic movement are larger and more complex, the ability to sample their movement and produce an adequate correction at lower computational cost is a distinct advantage.

Although the method of MD differs from previous approaches, the method for extrapolating the appropriate data is the same,[64] and is only summarised here. Equation 5.5 describes distance $r_{a,ij}$ as the inverse of the inverse of the vibrational averaged distances. N is the number of steps from the simulation, while $r_{ij,k}$ is the distance between atoms i and j at time-step k:

$$r_{a,ij} = \left[\frac{1}{N} \sum_{k=1}^{N} (r_{ij,k})^{-1} \right]^{-1} . \tag{5.5}$$

An optimised geometry calculated using the same basis set and level of theory as the MD simulation, provides the values for r_e. Subtracting r_e from r_a for each interatomic distance gives the distance correction to be used during a GED refinement.

The amplitudes of vibration are extracted from the MD simulations using Equation 5.6:

$$u_{ij} = \left[\frac{1}{N_p N_s} \sum_{p=1}^{N_p} \sum_{n=1}^{N_s} \left(r_{ij}^{n,p} - \langle r_{ij}^p \rangle \right)^2 \right]^{\frac{1}{2}} \quad , \tag{5.6}$$

where N_p is the number of equivalent pairs in the molecule and N_s is the number of steps in the simulation. The angle brackets denote the average value.

The distance corrections and amplitudes of vibration are extracted from the Newton-X trajectory using MDSIM, which was also used with the MD simulations carried out previously by Wann *et al.*[29, 64, 106]

5.4 Results and Discussion

All molecular dynamics mentioned in this Chapter concern cyanuric chloride ($C_3N_3Cl_3$), shown in Figure 5.2; this molecule has been used in previous work in Edinburgh as a test case for vibrational corrections determined using MD simulations.[64] Comparison of the corrections calculated here with those published values, and the use of these new corrections in a full structural refinement will serve as a good estimate of their quality and, ultimately, the suitability of vibrational corrections determined from Newton-X MD simulations.

5.4.1 Calculations

The Andersen Thermostat (AT)[107] is used in this work, as it is the only thermostat within Newton-X. It provides a local temperature rather than a global bath temperature, as was used in the previous MD corrections work,[64] resulting in a faster equilibration of energy within the molecule. The kinetic energy of the system is modulated using a series of stochastic collisions, and a mean collision frequency is chosen, controlling the rate at which these collisions occur. An atom, having experienced a collision, is assigned a new random kinetic energy from a
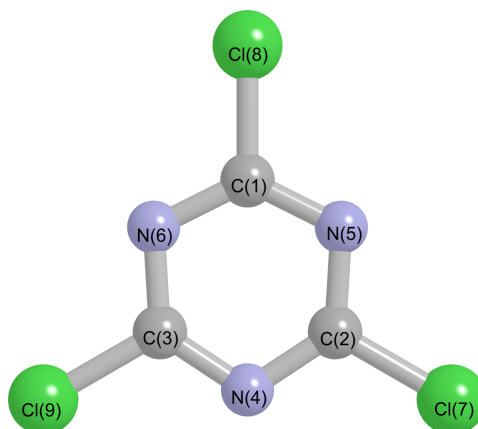
Figure 5.2 – Schematic diagram of the cyanuric chloride structure. Cyanuric chloride exhibits D_{3h} symmetry and has nine unique interatomic distances.

Boltzmann distribution of energies; the change in kinetic energy of the atoms is instantaneous and does not affect any other atoms in the molecule.

The faster equilibration achieved means that the full movement profile of the molecule can be sampled more quickly. The work mentioned previously, with which the data here are compared, used a "massive chain" of Nosé-Hoover thermostats[108, 109] as a temperature bath in the Car-Parrinello Molecular Dynamics (CPMD) software.[110, 111] The initial few picoseconds of the simulation were discarded as this time was needed for the molecule to equilibrate. As shown in Table 5.1, the equilibration time (denoted by the number of steps that must be skipped) of the Newton-X simulations is far shorter. Variation between the corrections calculated using the entire simulation (skipped steps = 0), and those discarding the initial 500 fs (skipped steps = 1000) and 1 ps (skipped steps = 2000) is very small. As a result, an acceptable MD simulation, which samples sufficiently the trajectory of the molecule, is shorter in length.

Table 5.1 – Amplitudes of vibration, u_{NX}, and distance corrections, r_a-r_{NX}, obtained for different number of skipped steps, for $C_3N_3Cl_3$. Tabulated values are in picometers.

atom pair	skipped steps = 0		skipped steps = 1000		skipped steps = 2000	
	u_{NX}	r_a-r_{NX}	u_{NX}	r_a-r_{NX}	u_{NX}	r_a-r_{NX}
C(1)−N(5)	3.2	0.1	3.2	0.1	3.2	0.1
C(1)−Cl(8)	4.4	2.8	4.4	2.8	4.3	2.6
C(1)···C(2)	4.0	−0.3	4.0	−0.3	4.0	−0.4
N(4)···N(5)	4.3	−0.2	4.2	−0.2	4.3	−0.2
N(4)···Cl(7)	6.2	2.3	6.2	2.3	6.2	2.1
C(1)···N(4)	4.9	−0.4	4.8	−0.5	4.8	−0.5
C(1)···Cl(7)	6.2	1.6	6.2	1.6	6.2	1.3
N(4)···Cl(8)	6.1	1.2	6.2	1.1	6.2	0.8
Cl(7)···Cl(8)	9.2	2.9	9.1	2.8	9.2	2.3

For the corrections calculated using Newton-X MD simulations to be valid, they must be tested against a reference. The reference chosen is the best correction obtained by Wann *et al.*,[64] using PIMD.

The frequency with which the kinetic energy is modulated using the AT impacts the perturbation of the molecular motion and, as such, alters the corrections obtained. Varying this frequency (ν) was tested and the results are shown in Table 5.2. The comparison values from the PIMD simulation are shown,[64] these corrections were deemed the highest quality of those obtained in that work.

Table 5.2 – Amplitudes of vibration, u_{NX}, and distance corrections, $r_a - r_{NX}$, obtained for different collision frequencies, for the MD simulations carried out in this work compared to the previous PIMD simulations for $C_3N_3Cl_3$. All calculations were performed using the B3LYP method and the 6-31G* basis set. Tabulated values are in picometers.

atom pair	0.10 fs^{-1}		0.15 fs^{-1}		0.20 fs^{-1}		D. A. Wann *et al.*[64]	
	u_{NX}	$r_a - r_{NX}$	u_{NX}	$r_a - r_{NX}$	u_{NX}	$r_a - r_{NX}$	u_{PIMD}	$r_a - r_{PIMD}$
C(1)−N(5)	3.2	−0.1	3.2	0.0	3.2	0.1	4.6	0.6
C(1)−Cl(8)	4.3	2.6	4.4	2.7	4.3	2.6	5.2	0.9
C(1)···C(2)	4.0	−0.5	4.0	−0.2	4.0	−0.4	5.3	0.7
N(4)···N(5)	4.5	−0.4	4.5	−0.3	4.3	−0.2	5.5	0.8
N(4)···Cl(7)	6.4	2.0	6.1	2.3	6.2	2.1	6.6	1.1
C(1)···N(4)	5.2	−0.7	5.1	−0.4	4.8	−0.5	6.2	0.7
C(1)···Cl(7)	6.1	1.2	6.1	1.7	6.2	1.3	6.6	0.8
N(4)···Cl(8)	6.3	0.8	6.5	1.3	6.2	0.8	6.8	0.6
Cl(7)···Cl(8)	9.8	2.3	9.1	3.0	9.2	2.3	8.5	0.8

Increasing ν does not alter the amplitudes of vibration of the bonded and shorter non-bonded pairs of atoms to any great extent; however, the longer non-bonded amplitudes of vibrations, especially between two chlorine atoms, get smaller as collision frequency increases. This reduction in the non-bonded amplitudes of vibration brings them closer to the reference PIMD values, which were shown to be good corrections for this molecule.[64] The distance corrections, upon increase in ν from 0.1 to 0.2 fs^{-1}, also becomes closer to the PIMD values, although the disparity between the corrections found and the PIMD values is still unacceptably large.

The description of the dynamics of the molecule is dependent upon the forces calculated at each time-step, so a better calculation should improve the quality of the correction obtained. To that end, further MD simulations were run at B3LYP, M06-2X and PBE1PBE levels of theory, also increasing the size of the basis set used to describe the molecule from 6-31G* to 6-311+G*. The results are presented in Table 5.3, as well as the reference PIMD values.[64]

Increasing in the size of the basis set, from 6-31G* to 6-311+G*, reduces the amplitudes of vibration, especially in the case of atom pairs involving chlorine atoms. Non-bonded distance to chlorine, both $C\cdots Cl$ and $Cl\cdots Cl$, are reduced by the most. The improvement in the description of the larger, more electronically complex chlorine atoms by the increased basis set is most likely responsible for this. A reduction in the values of the amplitudes of vibration is also observed when the level of theory is changed to M06-2X, bringing these longer interactions into better agreement with the rest of the atom pairs compared to the PIMD values. All amplitudes of vibration are now smaller than or similar to the PIMD derived values.

Table 5.3 – Amplitudes of vibration, u_{NX}, and distance corrections, $r_{\mathrm{a}}-r_{\mathrm{NX}}$, taken from Newton-X simulations using different levels of theory and basis sets. These are compared to the previous PIMD simulations performed for $C_3N_3Cl_3$ in Edinburgh. All simulations are run at 473.15 K, $\nu = 0.20$ fs^{-1}, and tabulated values are in picometers.

atom pair	B3LYP/6-31G*		B3LYP/6-311+G*		M06-2X/6-311+G*		MN12-SX/6-311+G*		D. A. Wann $et\ al.$[64]	
	u_{NX}	$r_{\mathrm{a}}-r_{\mathrm{NX}}$	u_{NX}	$r_{\mathrm{a}}-r_{\mathrm{NX}}$	u_{NX}	$r_{\mathrm{a}}-r_{\mathrm{NX}}$	u_{NX}	$r_{\mathrm{a}}-r_{\mathrm{NX}}$	u_{PIMD}	$r_{\mathrm{a}}-r_{\mathrm{PIMD}}$
C(1)−N(5)	3.2	0.1	3.2	−0.3	3.2	−0.8	3.2	−0.7	4.6	0.6
C(1)−Cl(8)	4.3	2.6	4.5	2.6	4.2	1.1	3.9	0.3	5.2	0.9
C(1)···C(2)	4.0	−0.4	3.9	−0.4	4.1	−1.6	4.0	−1.7	5.3	0.7
N(4)···N(5)	4.3	−0.2	4.5	−1.3	4.2	−1.8	4.5	−1.4	5.5	0.8
N(4)···Cl(7)	6.2	2.1	5.9	2.2	5.8	0.1	5.7	−0.6	6.6	1.1
C(1)···N(4)	4.8	−0.5	5.0	−1.2	4.9	−2.1	5.1	−1.9	6.2	0.7
C(1)···Cl(7)	6.2	1.3	5.8	1.5	6.0	−1.1	5.4	−2.0	6.6	0.8
N(4)···Cl(8)	6.2	0.8	6.2	0.5	6.1	−1.8	5.8	−2.5	6.8	0.6
Cl(7)···Cl(8)	9.2	2.3	8.0	2.8	8.5	−1.2	8.0	−2.5	8.5	0.8

An increase in temperature in the MD simulation will likely increase all of these amplitudes, increasing agreement with the PIMD values, especially for the bonded distances. As the AT has been shown to overly perturb motion in isolated molecule simulations,[112] an artificial increase in temperature within the simulation was tested to see if any improvement could be obtained. The resulting amplitudes of vibration and distance corrections are shown in Table 5.4.

Table 5.4 – Amplitudes of vibration, u_{NX}, and distance corrections, $r_a - r_{NX}$, taken from Newton-X simulations using different temperatures. These are compared to the previous PIMD simulations performed for $C_3N_3Cl_3$ in Edinburgh. All calculations are performed using the B3LYP level of theory and the 6-31G* basis set with a collision frequency of 0.2 fs^{-1}. Tabulated values are in picometers.

atom pair	473.15 K		673.15 K		D. A. Wann *et al.*[64]	
	u_{NX}	$r_a - r_{NX}$	u_{NX}	$r_a - r_{NX}$	u_{PIMD}	$r_a - r_{PIMD}$
C(1)−N(5)	3.2	0.1	3.9	−0.8	4.6	0.6
C(1)−Cl(8)	4.3	2.6	5.1	−2.3	5.2	0.9
C(1)···C(2)	4.0	−0.4	5.0	0.2	5.3	0.7
N(4)···N(5)	4.3	−0.2	5.3	−3.0	5.5	0.8
N(4)···Cl(7)	6.2	2.1	7.1	−1.7	6.6	1.1
C(1)···N(4)	4.8	−0.5	6.2	−1.8	6.2	0.7
C(1)···Cl(7)	6.2	1.3	7.1	−1.9	6.6	0.8
N(4)···Cl(8)	6.2	0.8	7.4	−4.0	6.8	0.6
Cl(7)···Cl(8)	9.2	2.3	11.0	−3.8	8.5	0.8

Increasing the simulation temperature by 200 K has, unsurprisingly, increased all of the amplitudes of vibration. The longer non-bonded amplitudes are now far larger than the PIMD values, but, as these simulation were, for reasons of time constraint, run at the lower B3LYP level of theory, with the smaller basis set 6-31G*, a reduction in these bonded distance would be expected upon improvement of the simulation theory and basis set as shown in Table 5.3. The

bonded and shorter non-bonded distances that have, for all simulations up to this point, been consistently lower than the PIMD comparison, now show far better agreement with the reference values. Therefore the likely best simulation requires an artificial increase in temperature paired with an increase in collision frequency, level of theory and basis set. A simulation was therefore run at M06-2X, with basis set 6-311+G*, collision frequency of 0.25 fs^{-1}, and temperature of 673.15 K. The results are shown in Table 5.5.

Table 5.5 – Amplitudes of vibration, u_{NX}, and distance corrections, $r_a - r_{NX}$, taken from the best Newton-X simulation performed. These are compared to the previous PIMD simulations performed for $C_3N_3Cl_3$ in Edinburgh. The simulation was performed using the M06-2X level of theory and the 6-311+G* basis set with a collision frequency of 0.25 fs^{-1} at 673.15 K. Tabulated values are in picometers.

atom pair	Best simulation		D. A. Wann *et al.*[64]	
	u_{NX}	$r_a - r_{NX}$	u_{PIMD}	$r_a - r_{PIMD}$
C(1)−N(5)	3.8	−0.6	4.6	0.6
C(1)−Cl(8)	4.9	1.3	5.2	0.9
C(1)···C(2)	4.5	−1.0	5.3	0.7
N(4)···N(5)	4.9	−1.9	5.5	0.8
N(4)···Cl(7)	6.8	0.7	6.6	1.1
C(1)···N(4)	5.8	−1.8	6.2	0.7
C(1)···Cl(7)	6.8	−0.5	6.6	0.8
N(4)···Cl(8)	6.8	−1.6	6.8	0.6
Cl(7)···Cl(8)	9.3	−0.4	8.5	0.8

The amplitudes of vibration are the closest to the PIMD reference values seen for any of the simulations; however, the smallest amplitudes of vibration are still lower than their equivalent values, and the Cl···Cl amplitude is still overestimated. This simulation represents the best compromise possible with the current implementation of Newton-X. To reduce further the amplitude for

Cl$\cdots$Cl, larger basis sets could be employed, but the increase in computational time required to run these simulations makes them impracticable at this time.

5.4.2 Refinement of $C_3N_3Cl_3$

Refinement of data collected for cyanuric chloride using vibrational corrections calculated from PIMD simulations has been carried out in the literature.[64] The vibrational corrections obtained from the Newton-X simulation using basis set 6-311+G*, at the M06-2X level of theory, collision frequency of 0.25 fs^{-1}, and temperature of 673 K were used in a refinement of the previously collected data. The goodness-of-fit R_G factor of 0.076 is similar to the 0.079 reported for the PIMD corrected refinement;[106] the bonded distances obtained from the refinement agree reasonably well with the PIMD corrected structure. The bonded distances from the Newton-X derived corrected refinement are 169.90(9) and 133.22(6) pm for the C$-$Cl and C$-$N distances, respectively, while the corresponding distances from the PIMD simulations are 170.24(9) and 132.14(6) pm. The remaining parameter used to describe the structure was $\angle$C$-$N$-$C, which was found to be 127.2(1)° from the Newton-X corrected refinement, and 127.04(9)° from the PIMD corrected refinement. Comparing these values against a geometry optimisations using MP2/6-311+G* which produced 126.86$^{\text{deg}}$ for $\angle$C$-$N$-$C, 171.2 pm for C$-$Cl and 133.4 for C$-$N, both the C$-$Cl distance and $\angle$C$-$N$-$C are further from the calculated values than the PIMD derived corrections. The C$-$N distance agrees well with the calculations. Overall the agreement is relatively close between the two methods, however the need to artificially increase the temperature for the Newton-X simulations reduces their applicability.

5.4.3 Further improvements

In lieu of artificially increasing the temperature of each simulation, a better approach to solving this problem is required as each molecule may require

different changes in thermostat to produce adequate results, negating the usefulness of the approach. The current implementation of Newton-X only allows for the use of the AT, which we have shown is inadequate for use in our work. The Andersen-Lowe thermostat (ALT)[113] is currently being implemented for the next release of Newton-X. It has been shown that the ALT does not perturb molecular motion to the same extent as the AT, and so should allow adequate corrections to be found without resorting to artificially increased temperature.[112] While the ALT should be an improvement upon the AT, it is still most commonly used in liquid or solid calculations and may still overly perturb the isolated molecule. A more applicable thermostating method using a combination of the ALT and a Nóse-Hoover could be the best approach to take.[114] Unfortunately, this is not available within the Newton-X package at present. As Newton-X is open-source software, adaptation to include a relevant thermostat could be undertaken within the group, if expertise existed.

After improvements to the temperature control of the isolated molecules, further calculations involving a wider range of test molecules, containing highly anharmonic or large-amplitude motions should be undertaken, for the Newton-X MD approach to be considered an all purpose source of vibrational corrections.

Chapter 6

Gas-phase structure of 4-(dimethylamino)benzonitrile

6.1 Introduction

The improvements to the York time-averaged GED apparatus, which were described in Section 2.3, led to calibration experiments, described in Chapter 4 demonstrating the capability for the collection of high-quality experimental data using this apparatus. In this Chapter, I report on the data collection, data extraction and structural refinement for 4-(dimethylamino)benzonitrile (DMABN).

DMABN displays dual fluorescence, the emission of light at two separate wavelengths, with the longer lived decay process associated with intramolecular charge transfer (ICT); it has been the subject of a number of studies: crystalline structure determined using X-ray diffraction,[115] dynamics and energies probed using a variety of spectroscopic methods,[115, 116] and theoretical calculations used to describe structural changes.[117, 118] Excitation to the second excited state can result in a structural change facilitating ICT, which could be directly probed using time-resolved electron diffraction. Not only would direct observation resolve the time-scales involved but also the structural pathways that allow relaxation of the molecule. This is of interest as the spectroscopic techniques have determined the lifetimes of the excited states as well as the likely relaxation pathways; however, without directly observing the structural change, a degree of uncertainty still exists.

The two electron diffraction apparatus that are in York present an opportunity to fully study the static and dynamic structures in tandem of DMABN and other molecules of interest. The experiments carried out on the time-averaged apparatus serve not only to provide a reliable structure for the ground state, but also to test some of the experimental conditions required for DMABN to be studied using the time-resolved apparatus.

6.2 Experimental

6.2.1 GED experimental

All diffraction data were collected using the York time-averaged apparatus, and the heated nozzle assembly described in Section 2.3.3.2. An accelerating voltage of 35 kV was used, resulting in an electron wavelength of approximately 6.45 pm. All images were recorded using the Stingray camera assembly described in Section 2.3.4.2. For all data collected the temperature of the heated nozzle assembly was 463 K at the nozzle tip, and 458 K at the sample. Two nozzle-to-camera distances were used, 140.33 mm (short) and 250.59 mm (long), and data were extracted using the EDSTRACT software outlined in Chapter 3. The beam current used for the short nozzle-to-camera distance was 1 μA; 0.5 μA used for the long nozzle-to-camera distance. Exposure times for all images acquired were 67 s; the maximum exposure time possible with this camera set-up for a single image. Data reduction and refinement were carried out using ed@ed v3.0,[34] using the scattering factors of Ross *et al.*[97] Nozzle-to-camera distances were determined using benzene at the same experimental conditions as those used for the collection of DMABN data.

The diffraction pattern collected was corrected using data for argon collected under the same experimental conditions; the corrected diffraction pattern is shown in Figure 6.1. The extracted intensities from this image are shown in Figure 6.2

The collected images are subject to the lensing effect described in Section 4.3.2 as the DMABN data were collected under the same experimental conditions as the benzene images used for the calibration of the lens distortion described in Section 4.3.3. All images used for this data extraction (DMABN image, argon image, background image) are treated in the same way as those corrected benzene images before extraction of data.
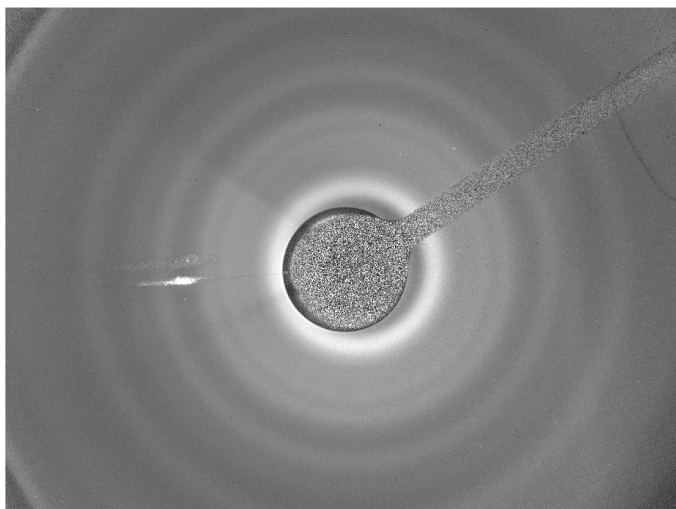
Figure 6.1 – Diffraction pattern for DMABN collected using the York time-averaged GED apparatus, corrected using argon data collected under the same experimental conditions.
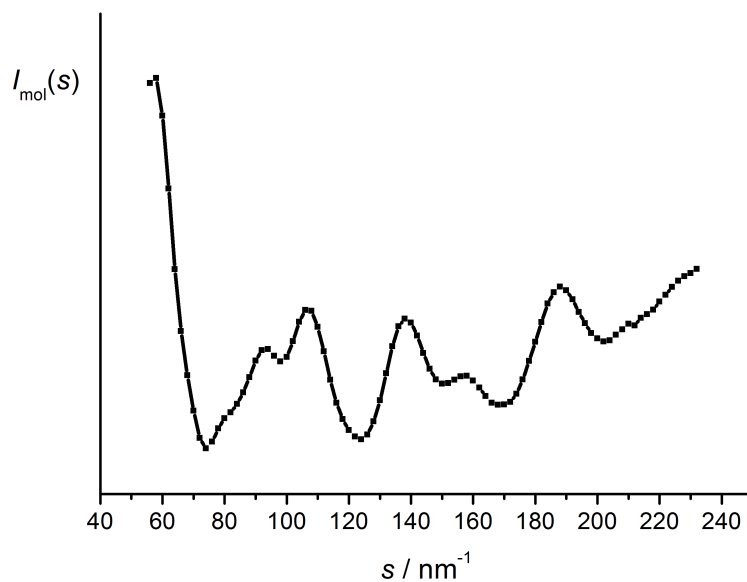
Figure 6.2 – Argon-corrected DMABN data extract at a short nozzle-to-camera distance of 140.33 mm.

6.3 Refinement

6.3.1 Model description

Figure 6.3 shows the structure of DMABN, useful for understanding the model used in the refinement. Atoms which are symmetrically equivalent are given the same number with a prime. The hydrogen atoms are given the same number as the atom to which they are bonded.
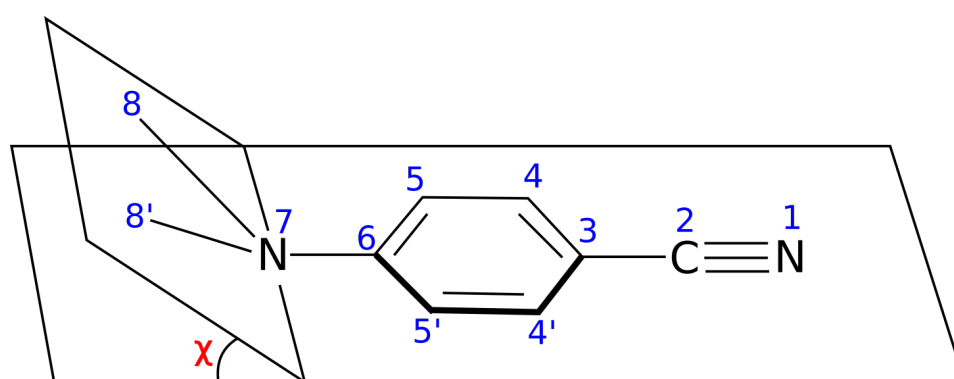
Figure 6.3 – Structure of DMABN with atom numbering. Hydrogen atoms have been omitted for clarity but take the same number as the heavy atoms to which they are bonded.

The model used in the refinement of DMABN consists of 14 parameters (p_n, n = 1−14), namely eight distances and six angles. χ denotes the angle between the plane of the aromatic ring, and the plane made by the nitrogen and two methyl carbons. Six of the bonded distances within DMABN lie under one peak in the RDC. To allow refinement of these similar distances a collection of weighted averages and differences have been used, shown in Equations 6.1−6.6:

$$p_1 = \frac{r\mathrm{C(2)C(3)}}{10} + \frac{2r\mathrm{C(3)C(4)}}{10} + \frac{2r\mathrm{C(4)C(5)}}{10} + \frac{2r\mathrm{C(5)C(6)}}{10} + \frac{r\mathrm{C(6)N(7)}}{10} + \frac{2r\mathrm{N(7)C(8)}}{10} \tag{6.1}$$

$$p_2 = \frac{r\mathrm{C(3)C(4)}}{2} + \frac{r\mathrm{C(5)C(6)}}{2} - r\mathrm{C(4)C(5)} \tag{6.2}$$

$$p_3 = r\mathrm{C(5)C(6)} - r\mathrm{C(3)C(4)} \tag{6.3}$$

$$p_4 = \frac{r\mathrm{C(2)C(3)}}{4} + \frac{r\mathrm{C(6)N(7)}}{4} + \frac{r\mathrm{N(7)C(8)}}{2} - \frac{r\mathrm{C(3)C(4)}}{3} - \frac{r\mathrm{C(4)C(5)}}{3} - \frac{r\mathrm{C(5)C(6)}}{3} \tag{6.4}$$

$$p_5 = \frac{r\mathrm{C(2)C(3)}}{3} + \frac{2r\mathrm{N(7)C(8)}}{3} - r\mathrm{C(6)N(7)} \tag{6.5}$$

$$p_6 = r\mathrm{C(6)N(7)} - r\mathrm{C(2)C(3)} \quad, \tag{6.6}$$

which are rearranged to give the distances in terms of the refineable parameters. These are shown in Equation 6.7−6.12:

$$r\mathrm{C(2)C(3)} = p_1 + \frac{3p_4}{5} + \frac{p_5}{4} - \frac{2p_6}{3} \tag{6.7}$$

$$r\mathrm{C(3)C(4)} = p_1 - \frac{p_4}{4} + \frac{p_2}{3} - \frac{4p_3}{5} \tag{6.8}$$

$$r\mathrm{C(4)C(5)} = p_1 - \frac{p_4}{4} - \frac{2p_2}{3} - \frac{3p_3}{10} \tag{6.9}$$

$$r\mathrm{C(5)C(6)} = p_1 - \frac{p_4}{4} + \frac{p_2}{3} + \frac{p_3}{5} \tag{6.10}$$

$$r\mathrm{C(6)N(7)} = p_1 + \frac{3p_4}{5} - \frac{3p_5}{4} \tag{6.11}$$

$$r\mathrm{N(7)C(8)} = p_1 + \frac{3p_4}{5} + \frac{p_5}{4} - \frac{p_6}{3} \quad . \tag{6.12}$$

The remaining distances are $r\text{N}(1)\text{C}(2)$ (p_7), the cyano group carbon-to-nitrogen distance, and $r\text{C}(8)\text{H}(8)$ (p_8), the methyl carbon-to-hydrogen distance. All hydrogen bond distances are based upon p_8, with the aromatic hydrogen bond distances from calculation only varying from the methyl hydrogen distance by 1.1 pm. As light atom parameters are described poorly by GED, the choice was made to fix the aromatic hydrogen distances as ($p_8 - 1.1$).

The six angle parameters are listed in Table 6.1.

Table 6.1 – List of angle parameters used in the refinement of DMABN.

parameter	constituent angles
p_9	$\angle\text{C}(8){-}\text{N}(7){-}\text{C}(8')$
p_{10}	χ
p_{11}	$\angle\text{C}(5){-}\text{N}(6){-}\text{C}(5')$
p_{12}	$\angle\text{C}(4){-}\text{N}(3){-}\text{C}(4')$
p_{13}	$[\angle\text{C}(3){-}\text{C}(4){-}\text{H}(4) + \angle\text{C}(6){-}\text{C}(5){-}\text{H}(5)]/2$
p_{14}	$\angle\text{N}(7){-}\text{C}(8){-}\text{H}(8)$

The average of $\angle\text{C}(3){-}\text{C}(4){-}\text{H}(4)$ and $\angle\text{C}(6){-}\text{C}(5){-}\text{H}(5)$ is taken for p_{13} as the variation between these angles is less than $1.0°$ at the B2PLYPD/aug-cc-pVTZ level of theory.

6.3.2 Computational details

Initially, the intention was to use the MD simulations approach outlined in Chapter 5 to provide the vibrational corrections for use in the refinement of DMABN. This has not been carried out as the problems with thermostatting the simulations, discussed in Section 5.4, require an artificial increase in temperature to achieve comparable results to other methods. The required increase in temperature used for $\text{C}_3\text{N}_3\text{Cl}_3$, is not necessarily the same required for DMABN and without a set of vibrational corrections produced from a trusted MD method to compare, the decision taken was to only perform an r_{h1} refinement.

Equilibrium structures have been determined using B3LYP, M06-2X, MN12-SX,[119] B2PLYPD[120] and MP2 levels of theory, with 6-31G* and aug-cc-pVTZ basis sets. The series of calculations is needed to provide appropriate restraints during the refinement of the structure as described in Section 1.2.3. SHRINK was used to calculate vibrational corrections at the MN12-SX level of theory, using the aug-cc-pVTZ basis set. This calculation was chosen as it yielded an equilibrium structure similar to that calculated at the MP2 level of theory with the same basis set, without the calculations of frequencies being prohibitively computationally expensive, such as is the case for both B2PLYPD and MP2.

The refinement carried out here yielded goodness-of-fit values of 0.16 and 0.10 for the R_G and R_D, respectively. The RDC and MIC from this refinement are shown in Figures 6.4 and 6.5, respectively. Selected structural parameters from the refinement (r_h1), as well as calculated values are shown in Table 6.2, which also contains parameters relating to the published crystal structure.[121]

Table 6.2 – Selected theoretical and GED experimental (r_{h1}) structural parameters for DMABN. For all calculations below the aug-cc-pVTZ basis set was used. Tabulated distances are in picometers and angles in degrees. Crystallographic data collected at 293 K are shown where available.

	B3LYP	M06-2X	MN12-SX	B2PLYPD	MP2	r_{h1}	Crystallographic data[121]
rN(1)−C(2)	115.4	114.9	115.1	116.2	117.4	117.5(8)	114.5(3)
rC(2)−C(3)	142.4	143.0	142.3	142.6	142.8	144.9(9)	143.4(4)
rC(3)−C(4)	140.0	139.4	139.5	140.0	139.8	139.8(4)	138.1(3)
rC(4)−C(5)	138.0	137.8	137.6	138.3	138.7	139.0(6)	136.8(3)
rC(5)−C(6)	141.3	141.0	140.8	141.3	141.0	141.2(4)	139.6(3)
rC(6)−N(7)	136.6	136.6	137.1	137.3	138.0	140.1(10)	136.7(3)
rN(7)−C(8)	145.2	144.6	143.9	145.1	145.1	145.8(6)	145.7(3)
∠C(4)−C(3)−C(4′)	118.3	118.8	118.4	118.6	119.0	118.5(6)	-
∠C(5)−C(6)−C(5′)	117.3	117.7	117.6	117.4	117.4	117.2(4)	-
∠C(8)−N(7)−C(6)	120.3	119.9	119.9	119.4	117.9	118.0(8)	121.6(3)
∠C(8)−N(7)−C(8′)	119.4	120.1	119.4	118.5	116.7	123.8(18)	116.5(2)
χ	0.0	0.0	8.7	16.4	26.7	5(10)	10.8(2)
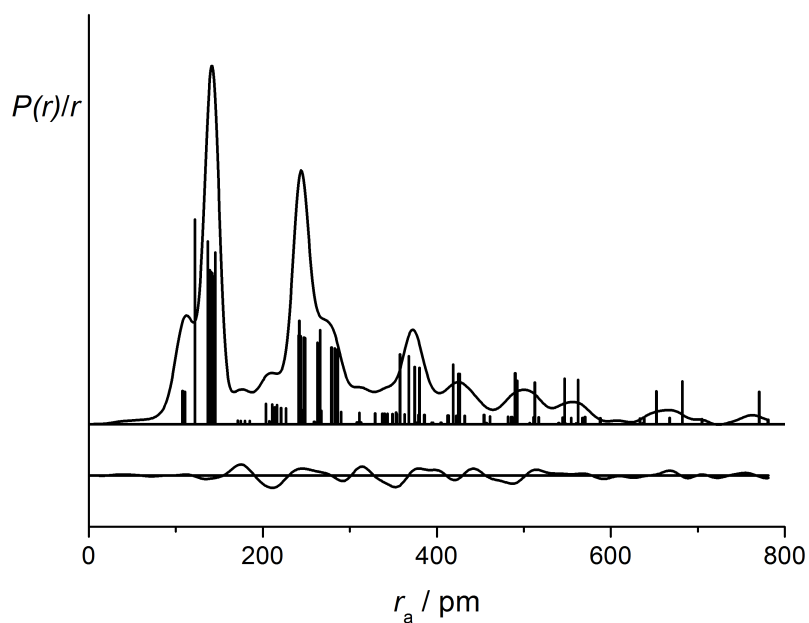
Figure 6.4 – Experimental and difference (experimental−theoretical) radial distribution curves, $P(r)/r$, from the GED refinement of DMABN using vibrational corrections from SHRINK. Before Fourier inversion, data were multiplied by $s \exp \left(\frac{-0.00002s^2}{(Z_C - f_C)(Z_N - f_N)} \right)$.

The refinement values and correlation matrices can be found in Appendix D.
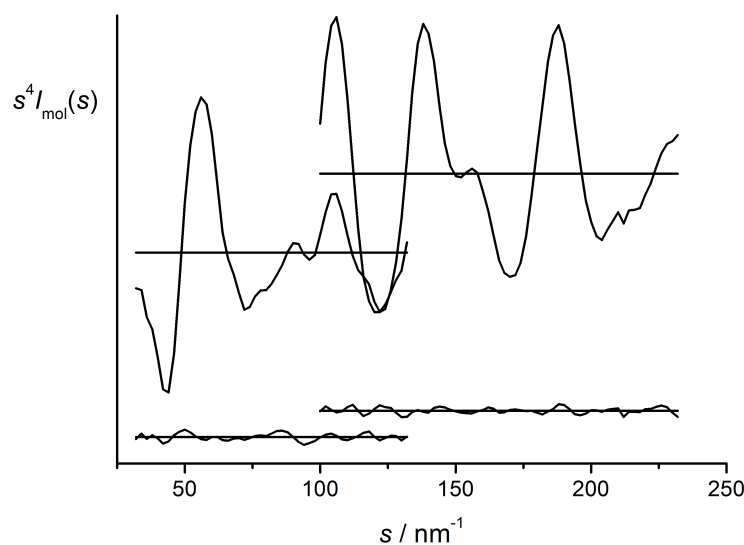
Figure 6.5 – Experimental and difference (experimental−theoretical), molecular intensity curves for DMABN. The top curve is collected at a short nozzle-to-camera distance, while the bottom curve is collected at a long nozzle-to-camera distance.

6.4 Discussion

The crystal structure of DMABN has been previously characterised,[121] showing pyramidalisation of the amine group.   The χ angle of 10.8(2)° is less than the corresponding angle found using microwave spectroscopy of 15°;[122] unfortunately, this value was presented without an uncertainty, as the angle was determined from fitting a small number of parameters to account for the inertia defects. The disparity between the crystal structure and the microwave spectroscopy determined structure is likely due to the crystal packing. The refinement carried out here also finds pyramidalisation, with an angle of 5(10)°. The very large uncertainty on the value reflects the very flat potential energy surface . Manually varying of the pyramidalisation angle from 0 to 30° showed very little difference in the R factors obtained.

The size of the angle χ is highly sensitive to the level of theory used. B3LYP,

153

as expected, poorly describes this angle, finding the benzene ring and the heavy atoms of the amine group to be coplanar. M06-2X has been posited as a replacement for general purpose calculations requiring the best compromise between short computational time and accuracy; however, it also fails to describe the angle between the planes, again giving a value of $0°$. Only when the level of theory is increased to MN12-SX, MP2, or when dispersion is considered in DFT, as in B2PLYPD, which employs the D2 correction of Grimme,[123] does the angle increase.

The quality of the data collected is an issue, as was seen for the benzene refinement in Chapter 4; however, optimisation of data collection procedure, which was not possible during the time of this thesis, and recalibration of the camera to account for the lensing effect could be carried out relatively quickly. This refinement was performed using the one viable image collected, but in future multiple images could be stacked to improve the data quality.

From the refinement of benzene carried out in Chapter 4 the distances obtained were within 3 standard deviations of the literature values. The same is seen for DMABN relative to crystallographic and the highest level *ab initio* calculations carried out (MP2/aug-cc-pVTZ).

The lack of quality in this data limits its application in full structure determination, but the refined distances can also be used to inform us about the problems with the camera. The distances are, for the most part, larger than for any of the calculations, which could suggest that the nozzle-to-camera distances used for this refinement were slightly shorter than in reality, further demonstrating the failing in the current camera correction. An approach to improving the correction and therefore increasing the quality of data for refinement is outlined in Section 7.1.1.1. Once these have been carried out, the refinement of newly collected data for DMABN would be beneficial in the comparison to crystallography and microwave spectroscopy.

Chapter 7

Conclusions and future work

7.1 Apparatus additions

During this PhD, improvements to the experimental set-up in York have increased the applicability of the apparatus. Heating of samples can allow lower volatility compounds to be studied, and the new camera assembly shows promise, displaying no contraction of data as has been reported in the thesis of Stuart Hayes.[11]

A skimmer box and the ability to pump away background carrier gas and sample already exists within the York apparatus. The testing and refinement of this in conjunction with an appropriate pulsed nozzle will allow novel experiments to be carried out, and will increase comparability with the time-resolved GED apparatus also present within the group. Samples deemed suitable for study in the time-resolved apparatus can have their experimental viability checked in this apparatus.

7.1.1 Camera improvements

To increase the intensity of photons produced from the electron impacts to the phosphor screen a new phosphor could be tested. Two suggestions for a new phosphor screen are P43 and P47, both of which display longer decay times than the phosphor currently in use in this apparatus. The increased lifetime of the scintillation allows a greater intensity to be recorded by the camera over the course of the experiment. In time-resolved electron diffraction experiments, where the number of incident electrons is low, these phosphors can greatly reduce the required exposure time required for adequate quality diffraction images.[124] For less volatile species, where low target density is a problem, the effect would be the same.

7.1.1.1 Improved camera calibration

The calibration used in Section 4.3.3 improved the lens problem encountered with the Stingray custom camera assembly. However, the correction is not as good as it could be, shown in the contraction still seen in the data acquired and refined for benzene. The application of a more sophisticated image with which to calibrate the camera should improve the correction applied to the extent that data recorded using the Stingray camera assembly may in the future be used for publishable structural refinements. This might involve the use of a pattern containing a series of small dots at regularly spaced intervals, as opposed to the square grid used in Section 4.3.3. The smaller size of the spots would allow inconsistencies between the calibration and collected images to be more easily identified, and corrected.

7.2 Molecular dynamics improvements

The problems encountered in the MD simulations performed in Chapter 5 were due to the thermostatting of the simulations overly perturbing the atomic movement due to the use of the Andersen thermostat. The need to artificially increase the simulation temperature to produce useful corrections means that these corrections are not currently useful.

Recent unpublished work elsewhere has involved performing MD for vibrational corrections using GAMESS US,[125, 126] controlling the temperature using a Nosé-Hoover thermostat.[127] The vibrational corrections are of a high quality, suggesting that this may be a better approach to calculating corrections for the more exotic species that the apparatus is intended to study.

The Newton-X derived corrections may be of use in the study of molecules containing small numbers of atoms. Global bath thermostats struggle to partition the potential and kinetic energies of these molecules.[128, 129] The AT maintains temperature using a local thermostat altering the velocity of single atoms

randomly at a set rate. This would allow the thermostatting of these small molecules. For this to be viable, an improved thermostat, such as the ALT is needed.

As mentioned in Chapter 5, the molecules to which these MD-derived vibrational corrections will be most applicable are those with anharmonic and large-amplitude vibrations. For example, carbon suboxide (C_3O_2) vibrates far from its equilibrium geometry and is, therefore, badly described by frequency calculations based on that geometry. The same is true of non-covalent interactions (NCI), both intra- and intermolecular, which, due to their relatively weak interaction energies, have large amplitudes of vibration. As the apparatus described in this thesis has the capability of introducing samples through a supersonic expansion nozzle, the formation of weakly-bound species is possible. The use of MD-derived corrections with the study of weakly bound species using this apparatus could yield structural parameters important in many areas of chemistry, such as medicinal drug interaction and macromolecular chemistry. The data would be particularly useful for calibrating computational methods.

Some calculations have been carried out to determine the suitability of different molecules for study using the supersonic expansion nozzle. For the molecules to be suitable, at least in early experiments, an appreciable change in the proportion of dimer or complementary pair in the beam being probed is needed upon cooling in the supersonic expansion. Interactions with strong intermolecular forces are already present as dimers in high proportion at room temperature, reducing the impact cooling the sample would have. One possible sample to study is silyl chloride (SiH_3Cl). Based upon frequency calculations using MP2/6-311+G*, the percentage of the molecules present as dimers increase by more than 10% when sample cooled to 100 K, a temperature well within the range of this type of supersonic nozzle.

Appendix: associated publications

Work carried out during my PhD has led to the publication of one article, published in a peer reviewed journal. For the aid of the examiners, this article is appended here.

Publication:

Structures of Tetrasilylmethane Derivatives C(SiXMe$_2$)$_4$ (X = H, F, Cl, Br) in the Gas Phase and their Dynamic Structures in Solution - D. A. Wann, S. Young, K. Bätz, S. L. Masters, A. G. Avent, D. W. H. Rankin and P. D. Lickiss, Z. *Naturforsch. B*, 2014, **69**, 1321-1332, DOI: 10.5560/ZNB.2014-4147

Structures of Tetrasilylmethane Derivatives C(SiXMe$_2$)$_4$ (X = H, F, Cl, Br) in the Gas Phase and their Dynamic Structures in Solution

Derek A. Wann[a], Stuart Young[a], Karin Bätz[b], Sarah L. Masters[c], Anthony G. Avent[d,†], David W. H. Rankin[e], and Paul D. Lickiss[b]

[a] Department of Chemistry, University of York, Heslington, York, UK YO10 5DD

[b] Department of Chemistry, Imperial College London, London, UK SW7 2AZ

[c] Department of Chemistry, University of Canterbury, Private Bag 4800, Christchurch 8140, New Zealand

[d] Department of Chemistry, School of Life Sciences, University of Sussex, Falmer, Brighton, UK BN1 9QJ

[e] School of Chemistry, University of Edinburgh, West Mains Road, Edinburgh, UK EH9 3JJ

[†] Deceased

Reprint requests to Dr. D. A. Wann. E-mail: derek.wann@york.ac.uk

Dedicated to Professor Hubert Schmidbaur on the occasion of his 80th birthday

The structures of the molecules C(SiXMe$_2$)$_4$ (X = H, F, Cl, Br) have been determined by gas electron diffraction (GED). *Ab initio* calculations revealed nine potential minima for each species, with significant ranges of energies. For the H, F, Cl, and Br derivatives nine, seven, two, and two conformers were modelled, respectively, as they were quantum-chemically predicted to be present in measurable quantities. Variable-temperature ^{1}H and ^{29}Si solution-phase NMR studies and, where applicable, ^{13}C NMR, ^{1}H/^{29}Si NMR shift-correlation, and ^{1}H NMR saturation-transfer experiments are reported for C(SiXMe$_2$)$_4$ (X = H, Cl, Br, and also I). At low temperature in solution two conformers (one C_1-symmetric and one C_2-symmetric) are observed for each of C(SiXMe$_2$)$_4$ (X = Cl, Br, I), in agreement with the isolated molecule *ab initio* calculations carried out as part of this work for X = Cl, Br. C(SiHMe$_2$)$_4$ is present as a single C_1-symmetric conformer in solution at the temperatures at which the NMR experiments were performed.

Key words: Silyl Methane Derivatives, Gas Electron Diffraction, Variable-Temperature NMR

Introduction

The chemistry of tetrasilylmethane derivatives has been studied extensively, with the severe steric constraints imposed by four Si-centred substituents attached to a carbon atom often leading to unusual reactivities and novel structural features [1 – 4]. The most widely studied tetrasilylmethane derivatives have the general structures (Me$_3$Si)$_3$CSiRR′X, (PhMe$_2$Si)$_3$CSiRR′X, and (Me$_3$Si)$_2$C(SiXMe$_2$)(SiR$_2$Y) (where R and R′ = Me, Et, Ph *etc.* and X, Y = H, halide, OAc *etc.*) [1 – 4].

A range of related tetrasilylmethanes with four substituents of the same kind C(SiXMe$_2$)$_4$ (X = H [5 – 8], Ph [9 – 11], OH [12, 13], OMe [6, 14], OEt [6, 14], OAc [6], O$_2$CCF$_3$ [6], OSO$_2$CF$_3$ [15], OSO$_2$-C$_6$H$_4$-*p*-Me [15], F [6], Cl [6, 16, 17], Br [6], and I [6] are known, although little of their chemistry has been explored. In contrast, the permethyl species, C(SiMe$_3$)$_4$, has been the subject of numerous reports, using NMR spectroscopy [18 – 22], X-ray diffraction [23 – 25], gas electron diffraction (GED) [26, 27], quantum-chemical calculations [28, 29], and vibrational spectroscopy [29].

Dynamic processes in bulky tetrasilylmethane derivatives have been studied previously by NMR spectroscopy in solution, for example, for C(SiMe$_3$)$_2$(SiMePh$_2$)(SiMe$_2$ONO$_2$) [30], C(SiMe$_3$)$_2$(SiClPh$_2$)(SiMe$_2$OMe) [31], and (Me$_3$Si)$_3$SiX$_3$ (X = Cl, Br) and (PhMe$_2$Si)$_3$SiCl$_3$ [32]. (Me$_3$Si)$_3$CSiH$_3$ was stud-

ied using both NMR spectroscopy and GED [33], while GED studies have also been carried out for (Me$_3$Si)$_3$CSiCl$_3$ [34], and for (HMe$_2$Si)$_3$CSiH$_3$ [35], which showed the presence of eleven distinct conformers.

The work presented here comprises two main parts. First, the multiconformer structures of C(SiXMe$_2$)$_4$ [X = H (**1**), F (**2**), Cl (**3**), Br (**4**)] have been determined by GED experiments aided by *ab initio* calculations. Secondly, an NMR spectroscopic investigation of the dynamic processes occurring in C(SiXMe$_2$)$_4$ species [this time including X = I (**5**)] in solution has been undertaken.

Experimental Section

Syntheses of C(SiXMe$_2$)$_4$ (X = H, F, Cl, Br, I)

The syntheses of C(SiHMe$_2$)$_4$ (**1**) [5, 6], C(SiFMe$_2$)$_4$ (**2**) [6], C(SiClMe$_2$)$_4$ (**3**) [6], C(SiBrMe$_2$)$_4$ (**4**) [6], and C(SiIMe$_2$)$_4$ (**5**) [6] were carried out using methods previously reported in the literature, and outlined in Scheme 1. Yields were generally good, and the compounds were purified by sublimation.

NMR spectroscopy

The ^{1}H, ^{13}C, and ^{29}Si NMR spectra were recorded in CDCl$_3$/CD$_2$Cl$_2$ or CDCl$_3$/[D$_6$]acetone solutions using a Bruker AMX 500 spectrometer at 500, 126, and 99 MHz, respectively, unless otherwise stated. The ^{29}Si{^{1}H} NMR INEPT spectra were recorded using a Bruker AMX 500 NMR spectrometer at 99 MHz, while ^{29}Si{^{1}H} inverse-gated NMR spectra were recorded on a Bruker Avance 600 spectrometer at 119.23 MHz. Chemical shifts for all NMR spectra are reported in ppm relative to TMS.

Computational methods

With four SiXMe$_2$ groups present in each of **1**–**4**, rotation about the C(1)–Si(2/3/4/5) bonds allows many possible conformers to exist. The atom numbering used throughout
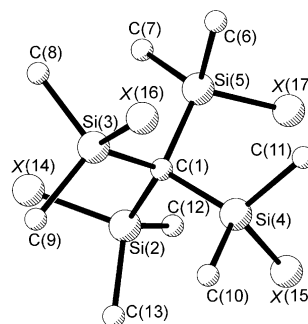
Fig. 1. Representation of the general structure of C(SiX-Me$_2$)$_4$ with atom numbering. Hydrogen atoms have been removed for clarity. For numbering of subsequent conformers, $[41 \times (n-1)]$ should be added, where n is the number of the conformer.

this work is shown in Fig. 1. Before interpreting gas electron diffraction data it is important to identify all possible minimum-energy structures and compare their energies, to judge which will be present in observable amounts at the experimental conditions. Experience suggests that molecules such as **1**–**4** often have groups that are rotated by $15-20°$ from a perfectly staggered geometry, and that $+20°$ and $-20°$ for any particular group may give different structures, depending on the overall symmetry [36]. The four SiXMe$_2$ groups for each of **1**–**4** were treated as two pairs [the groups based on Si(2) and Si(3) were defined relative to one another and, similarly the groups based on Si(4) and Si(5) were paired], allowing dihedral angles to be uniquely defined as X(14)–Si(2)–C(1)–Si(3), X(16)–Si(3)–C(1)–Si(2), X(15)–Si(4)–C(1)–Si(5), and X(17)–Si(5)–C(1)–Si(4). Allowing just one of the SiXMe$_2$ groups to rotate with all others fixed, a potential-energy scan was performed; this indicated that each group could be present in three possible minimum-energy orientations, with dihedral angles (as defined above) of approximately -80, 160, and $40°$. With four SiXMe$_2$ groups acting independently that gives a total of $3^4 (= 81)$ possible conformations. Considering the negative sense of each dihedral angle (*i. e.* 80, -160 and $-40°$) gives an additional 81 possible conformers.

Geometry optimisations and frequency calculations were carried out to determine the free energies of all conformers. All calculations utilised the GAUSSIAN 09 [37] suite of programs and were performed on the University of Edinburgh ECDF cluster [38] or the UK National Service for Computational Chemistry Software clusters [39]. For comparison, both the B3LYP [40–42] and M06-2X [43] methods with 6-31G(d) basis sets [44, 45] were used for these calculations.

For each species nine low-energy conformers were identified, and further geometry optimisations and frequency calculations were then carried out. The B3LYP hybrid method

CBr$_4$ + HMe$_2$SiCl + Mg $\xrightarrow{\text{THF}}$ C(SiHMe$_2$)$_4$

$\downarrow$ X$_2$ X = Cl, Br, I

C(SiFMe$_2$)$_4$ $\xleftarrow[\text{X = F}]{\text{AgBF}_4}$ C(SiXMe$_2$)$_4$ $\xleftarrow[\text{X = Cl, Br}]{\text{IX}}$ C(SiMe$_3$)$_4$
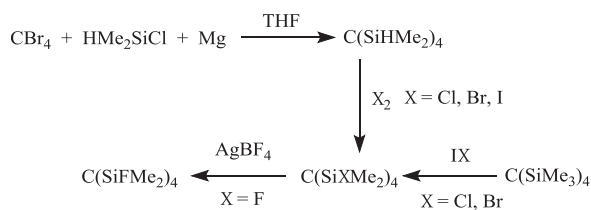
Scheme 1. Synthetic routes to C(SiXMe$_2$)$_4$ (X = H, F, Cl, Br, I) compounds.

with the aug-cc-pVDZ basis set [46, 47] was used for most atom types, with the aug-cc-pVDZ-PP [48, 49] pseudopotential basis set used for the heavy bromine atoms in **4**. Calculations were also performed using the M06-2X and MP2 methods [50] with the aug-cc-pVDZ(-PP) basis sets. All MP2 calculations were performed with a frozen core.

For each of **1**–**4**, force fields were calculated using analytic second derivatives of the energy with respect to the nuclear coordinates obtained at the M06-2X/aug-cc-pVDZ(-PP) level. These were then used with the program SHRINK [51, 52] to provide estimates of the amplitudes of vibration (u_{h1}) and curvilinear vibrational correction factors (k_{h1}) to internuclear distances required for the GED refinements.

Gas electron diffraction (GED)

The GED data used for the refinements of each of $C(SiXMe_2)_4$ (X = H, F, Cl, Br) (**1**–**4**) were collected using the apparatus formerly housed in Edinburgh [53], from samples that were synthesised and characterised at Imperial College London. Scattering intensities were recorded on Kodak Electron Image film at two nozzle-to-film distances, maximising the scattering angles over which data were collected. All nozzle-to-film distances and sample and nozzle temperatures are given in Table S1 in the Supporting Information available online (see note at the end of the paper for availability).

The photographic films were scanned using an Epson Expression 1680 Pro flatbed scanner using a routine method described elsewhere [54]. The data reduction and least-squares processes were carried out using the ED@ED v3.0 program [55], with the scattering factors of Ross *et al.* [56].

X-Ray crystallography

Several attempts were made to carry out single-crystal X-ray diffraction structural analyses of $C(SiHMe_2)_4$ (**1**), $C(SiClMe_2)_4$ (**3**) and $C(SiBrMe_2)_4$ (**4**) using an OD Xcalibur 3 diffractometer at 100 K in order to freeze out any dynamic disorder. Single crystals of **1** proved difficult to grow and, although the material diffracted, the quality of the diffraction pattern obtained was too poor to yield a believable unit cell. However, a highly symmetrical space group was suspected based on the behaviour of the crystals under polarised light. Both **3** and **4** were found to belong to the cubic space group $Pa\bar{3}$, with unit-cell dimensions of 12.46 and 12.53 Å, respectively. This space group requires complete disorder of chlorine and bromine positions along with at least two different sets of silicon positions. The disorder present precluded the identification of any specific conformers, and no model structures could be obtained for either **3** or **4**. A similar problem

was noted previously for $C(SiIMe_2)_4$, which also crystallised in a cubic unit cell [$a = 12.982(1)$ Å] [57].

Results and Discussion

Gas-phase static structures

Nine conformers were identified for each of **1**–**4**, arising from geometry optimisations started from all possible combinations of dihedral angle minima. Using the Boltzmann equation and the Gibbs free energy for each conformer, the relative amounts of all conformers were determined at the temperatures of the experiments. As is common practice, and to maintain the data-to-parameter ratios, only conformers present with more than approximately 5 % abundance were included in the model for refinement.

As an example, the free energies of all nine conformers of $C(SiBrMe_2)_4$ (**4**) are listed in Table 1. Similar listings of energies for $C(SiXMe_2)_4$ (X = H, F, Cl) are given in Tables S2–4, respectively. Also shown are the relative amounts of each conformer that would be present in the GED samples at the temperature of that experiment. Because of the large energy differences between the conformers, only two of the nine possible conformers of **4** would likely be observed in the GED experiment; these have been designated conformer 1 (C_1 symmetry), and conformer 2 (C_2 symmetry). The molecular structure and numbering of $C(SiBrMe_2)_4$ can be seen in Fig. 1. The atomic numbering scheme is the same for all four species (**1**–**4**) studied using GED.

Table 1. Total free energies and energy differences between conformers of $C(SiBrMe_2)_4$ (**4**) calculated at the M06-2X/6-31G(d) level.

Conformer[a]	Symmetry	Total free energy (kJ mol^{-1})	Relative energy[b] (kJ mol^{-1})	Abundance[c] (%)
1	C_1	−8336788.25	0.00	75.5
2	C_2	−8336785.25	3.01	16.7
3*	C_1	−8336775.50	12.78	2.4
4*	C_1	−8336774.36	13.92	1.8
5*	C_1	−8336774.32	13.97	1.7
6*	C_2	−8336775.77	12.51	1.3
7*	D_2	−8336774.09	14.20	0.4
8*	C_1	−8336765.55	22.76	0.2
9*	C_2	−8336761.61	26.71	0.0

[a] Conformers marked with a star were not considered to be present in sufficient quantities to be included in the GED refinement model; [b] energy differences are relative to conformer 1, the lowest-energy conformer; [c] calculated at the average temperature of the GED experiment.

GED studies

Experimental GED data were refined using parameterised models based on bond lengths, bond angles, and dihedral angles, guided by calculations at the MP2/aug-cc-pVDZ(-PP) level. The following description is for the Br derivative (**4**), but all models are based upon similar sets of bond lengths and angles, with the only significant differences being additional dihedral angle parameters arising from the number of conformers being modelled. Each species is described by four distances, ten bond angles, and two dihedral angles. Full lists of parameters for each of **1**–**4** (Tables S5–S8) and the model descriptions can be found in the Supporting Information.

From geometry optimisations it was observed that the four SiXMe$_2$ groups exist in a near tetrahedral geometry, with only slight deviations from the ideal tetrahedral angles. These deviations, as well as many other small deviations related to parameters used in the models, are taken into account using fixed (non-refinable) differences in the models. Fixed differences were also used to define small variations between the principal conformer for each species and any higher-energy conformers.

On the basis of the data presented in Table 1 and in Tables S2–4, the models were written to fit nine, seven, two, and two conformers for the H, F, Cl, and Br derivatives, respectively. For each of these species the differences between conformers were shown by MP2/aug-cc-pVDZ(-PP) calculations to be small. The approach taken when writing the models was, therefore, to choose parameters that adequately described the dominant conformer, and then to use fixed differences to describe the minor conformers.

The SARACEN [58–60] method was used for the refinement of experimental data, with the required restraints based upon comparison of calculations at the MP2, B3LYP and M06-2X levels of theory, and with 6-31G(d) and aug-cc-pVDZ basis sets (using aug-cc-pVDZ-PP as a pseudopotential for Br in **4**). Vibrational corrections were based upon data from SHRINK [51, 52], calculated using force constants obtained from GAUSSIAN.

As is common, because they are not particularly well defined from the GED data, restraints were placed upon the distance difference parameters, as well as upon parameters associated with hydrogen atoms.

Many dihedral angles were also restrained during the refinement process.

Amplitudes of vibration were grouped together, excluding those involving hydrogen, under their respective peaks in the radial distribution curves, with only that with the greatest scattering intensity refining. Other amplitudes under a given peak were allowed to change according to their ratios with respect to the refining value. Eleven amplitudes were refined for the Br derivative. Full lists of interatomic distances and amplitudes of vibration for **1**–**4** can be found in Tables S9–12, respectively.

All refinements were initially performed with the proportion of each conformer fixed at predicted values. For species **4** the proportion of conformer 1 was then stepped in increments of 0.05 either side of the predicted amount and the R factor recorded to ascertain the best fit. Fig. 2 shows this for **4**, where the 95 % confidence limit is also marked to allow the uncertainty in this measurement to be estimated [61]. The final proportion of conformer 1 was almost identical to that calculated, giving some reassurance that the Gibbs free energies were accurate. For **1**–**3** such an experimental determination was not possible. For **1** and **2** the presence of very many conformers with similar energies means that a satisfactory way of fixing some proportions and varying others could not be achieved. For **3** the quality of the experimental data are relatively poor (see further discussion later), and varying the amount of conformer 1 resulted in the R factor being lowest
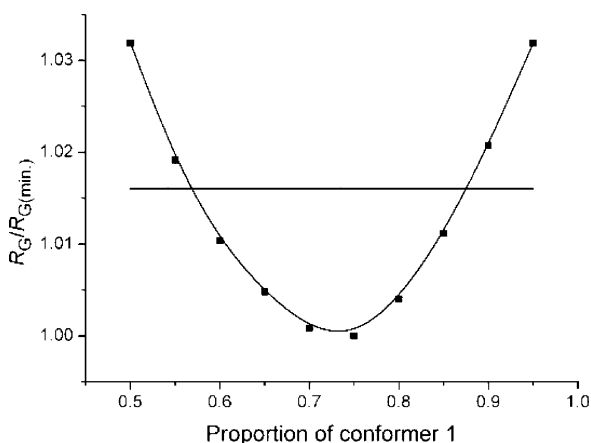

Fig. 2. Variation in R_G/R_G(min.) with different amounts of conformer 1 for species **4**. The horizontal line denotes the 95 % confidence limit, approximately equal to 2 σ.
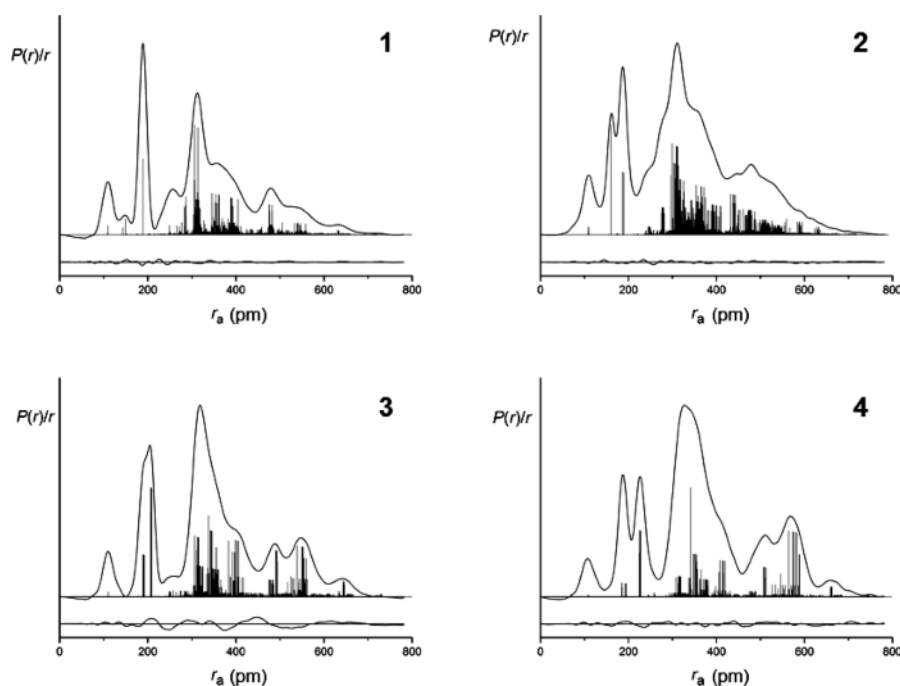
Fig. 3. Experimental and difference (experimental-minus-theoretical) radial distribution curves, $P(r)/r$, from the GED refinement of C(SiXMe$_2$)$_4$ [X = H (**1**), F (**2**), Cl (**3**), Br (**4**)]. Before Fourier inversion, data for **1** and **2** were multiplied by $s \cdot \exp(-0.00002s^2)/(Z_C - f_C)(Z_{Si} - f_{Si})$, while data for **3** and **4** were multiplied by $s \cdot \exp(-0.00002s^2)/(Z_C - f_C)(Z_X - f_X)$.

when the proportion of conformer 1 was 1.0; we do not believe that this is a realistic estimate.

Experimental radial distribution curves and difference curves can be seen for all four species in Fig. 3, illustrating the goodness of fits to the respective GED data. The R_G values obtained for X = H, F, Cl, Br were 8.4, 12.2, 11.0, and 12.5 %, respectively, with R_D values (ignoring off-diagonal elements of the weight matrix) of 7.5, 5.1, 10.0, and 7.5 %, respectively. A more complete explanation of differences between R_G and R_D can be found in ref. [62]. Figs. S1 – 4 show the related molecular intensity scattering curves as well as enlarged versions of the radial distribution curves in Fig. 3. Tables S13 – 16 show the correlation matrices for the refinements of each of **1** to **4**, while Tables S17 – 20 give the refined atomic positions of all conformers for the four species studied, and Tables S21 – 24 the equivalent calculated coordinates.

As mentioned earlier, a visual inspection of radial distribution curves for **3** indicates that the data were rather noisy. However, the R_G factor for the refinement of **3** suggests that these data fit at least as well as is the case for **2** and **4**. We can conclude that there was some-

thing affecting the quality of the raw data in the case of **3**, though we don't believe that this significantly affected the quality of the refinement.

Selected refined and calculated parameters for **1**–**4** are given in Tables 2 – 5. The bond lengths and angles shown correspond to the most abundant conformer of each species as this was the basis for the models, while dihedral angles describing the relative positions of the SiXMe$_2$ groups for all conformers are shown as these are individual to each conformer. Although each conformer can have two (C_2 symmetry) or four (C_1 symmetry) different C(1)–Si distances for each conformer of each of **1**–**4**, the variation in the C(1)–Si distances is small, with ranges of no more than 1 pm for a given species. Only one distance of this type is therefore shown in each of Tables 2 – 5.

For **1**, agreement between calculations and experimental data is seen for all bonded distances. Calculations at the B3LYP level (see Table 2) show a consistent overestimation of distances in the molecule, although the angles obtained are within 0.3° of the experimental values. Both MP2 and M06-2X level calculations for **1** give closer agreement to experimental data

Table 2. Selected experimental (r_{h1}) and quantum-chemically calculated (r_e) geometric parameters for **1**[a].

Parameter	r_{h1}	r_e B3LYP	r_e M06-2X	r_e MP2
rC(1)–Si(2)	189.4(4)	192.4	189.9	191.2
rSi(2)–C(12)	189.2(2)	189.9	188.9	189.9
rSi(2)–H(14)	149.9(8)	150.1	149.9	150.2
∠Si(2)–C(1)–Si(3)	108.3(1)	107.8	108.1	108.1
∠C(1)–Si(2)–C(12)	114.2(3)	114.1	113.2	113.3
∠C(1)–Si(2)–C(13)	114.2(3)	114.3	112.9	113.1
∠C(1)–Si(2)–H(14)	107.6(4)	107.4	108.0	107.8
∠C(10)–Si(4)–C(11)	106.9(10)	106.6	106.6	106.8
∠C(10)–Si(4)–H(15)	106.7(8)	106.9	107.8	107.7
ϕH(14)–Si(2)–C(1)–Si(4)	−74.9(21)	−71.5	−75.7	−74.6
ϕH(15)–Si(4)–C(1)–Si(2)	161.6(5)	162.1	163.4	161.6
ϕH(55)–Si(43)–C(42)–Si(44)	46.6(26)	49.6	47.0	47.5
ϕH(57)–Si(44)–C(42)–Si(43)	46.4(16)	47.7	46.1	46.6
ϕH(56)–Si(45)–C(42)–Si(46)	39.4(10)	39.6	40.1	39.4
ϕH(58)–Si(46)–C(42)–Si(45)	−79.8(11)	−79.5	−78.9	−79.7
ϕH(96)–Si(84)–C(83)–Si(85)	39.6(29)	42.6	39.8	40.3
ϕH(98)–Si(85)–C(83)–Si(84)	45.1(14)	46.3	44.8	45.3
ϕH(97)–Si(86)–C(83)–Si(87)	159.9(11)	159.7	160.8	160.0
ϕH(99)–Si(87)–C(83)–Si(86)	−75.9(8)	−75.2	−75.9	−75.9
ϕH(137)–Si(125)–C(124)–Si(126)	46.8(6)	47.4	46.9	46.9
ϕH(139)–Si(126)–C(124)–Si(125)	41.9(11)	41.8	42.4	41.9
ϕH(138)–Si(127)–C(124)–Si(128)	40.8(19)	41.6	40.5	41.0
ϕH(140)–Si(128)–C(124)–Si(127)	161.6(13)	162.6	161.7	161.7
ϕH(178)–Si(166)–C(165)–Si(168)	−76.8(15)	−74.7	−75.7	−76.3
ϕH(219)–Si(207)–C(206)–Si(208)	41.0(32)	44.2	41.3	42.0
ϕH(221)–Si(208)–C(206)–Si(207)	162.0(23)	164.1	161.6	162.2
ϕH(220)–Si(209)–C(206)–Si(210)	41.6(17)	40.7	42.5	41.7
ϕH(222)–Si(210)–C(206)–Si(209)	−81.5(16)	−80.5	−80.2	−81.3
ϕH(260)–Si(248)–C(247)–Si(249)	42.7(12)	43.2	43.6	42.8
ϕH(262)–Si(249)–C(247)–Si(248)	160.6(12)	161.5	160.3	160.6
ϕH(261)–Si(250)–C(247)–Si(251)	−77.1(7)	−76.5	−76.9	−77.1
ϕH(263)–Si(251)–C(247)–Si(250)	37.2(15)	36.9	38.1	37.3
ϕH(301)–Si(289)–C(288)–Si(290)	37.2(19)	36.8	38.4	37.3
ϕH(303)–Si(290)–C(288)–Si(289)	164.9(16)	166.1	164.9	165.0
ϕH(342)–Si(330)–C(329)–Si(332)	−76.9(8)	−76.3	−76.9	−76.9
ϕH(344)–Si(332)–C(329)–Si(330)	39.7(12)	39.8	40.6	39.8

[a] Distances (r) are in pm, angles (∠) and dihedral angles (ϕ) are in degrees. Atom numbering is given in Fig. 1. r_e values were calculated using the aug-cc-pVDZ basis set for each respective theory. The estimated standard deviations shown in parentheses represent 1σ.

for bonded distances, but predict angles that lie further from experiment. The experimentally determined dihedral angles are consistently closer to MP2 values than for the other two levels of theory, and MP2 provides overall the best prediction of the structure.

For **1**, MP2 consistently overestimates bonded distances, though by less than 1 %, with the largest discrepancy for the C(1)–Si(2/3/4/5) distance. For this species it is notable that the experimental data show no significant variations between the C(1)–Si(2/3/4/5) distances and those in the HMe$_2$Si groups. For **2**, **3**, and **4** theory shows slight variations between the C–Si

bond lengths in these different environments, with the difference increasing with the size of atom X.

For **2**, **3** and **4** bonded distances, angles, and dihedral angles calculated at the MP2 level were more consistently in agreement with experimental values than were the M06-2X and B3LYP levels of theory. The only exception to this occurs for bonded distances and bond angles to atom X. All levels of theory considerably overestimate these distances, and show variations in angles from experimental by as much as 4°. These deviations from the experimental values are due to insufficiently large basis sets to fully describe these atoms

Table 3. Selected experimental (r_{h1}) and quantum-chemically calculated (r_e) geometric parameters for **2**[a].

Parameter	r_{h1}	r_e B3LYP	r_e M06-2X	r_e MP2
rC(1)–Si(2)	189.3(2)	190.9	187.9	189.6
rSi(2)–C(12)	186.5(2)	187.9	186.6	187.7
rSi(2)–F(14)	160.6(1)	167.5	166.4	167.9
∠Si(2)–C(1)–Si(3)	109.5(3)	108.9	108.6	108.7
∠C(1)–Si(2)–C(12)	116.1(10)	116.4	115.2	115.6
∠C(1)–Si(2)–C(13)	112.9(12)	115.7	113.7	114.1
∠C(1)–Si(2)–F(14)	104.9(6)	104.3	104.6	104.7
∠C(10)–Si(4)–C(11)	109.1(10)	108.9	110.6	110.6
∠C(10)–Si(4)–F(15)	107.3(7)	105.7	107.1	106.8
ϕF(14)–Si(2)–C(1)–Si(3)	81.9(39)	79.7	83.8	83.2
ϕF(16)–Si(3)–C(1)–Si(2)	−167.2(10)	−166.4	−167.4	−167.2
ϕF(15)–Si(4)–C(1)–Si(2)	−153.2(20)	−151.3	−152.1	−152.4
ϕF(17)–Si(5)–C(1)–Si(2)	−39.2(29)	−40.8	−38.2	−39.4
ϕF(55)–Si(43)–C(42)–Si(44)	84.7(26)	86.4	85.3	85.8
ϕF(57)–Si(44)–C(42)–Si(43)	−40.9(33)	−41.4	−39.9	−40.2
ϕF(56)–Si(45)–C(42)–Si(43)	−166.0(46)	−166.4	−165.9	−166.1
ϕF(58)–Si(46)–C(42)–Si(43)	71.2(46)	71.5	72.7	71.9
ϕF(96)–Si(84)–C(83)–Si(85)	77.7(62)	73.4	80.0	79.8
ϕF(98)–Si(85)–C(83)–Si(84)	−163.8(46)	−162.2	−167.0	−163.8
ϕF(137)–Si(125)–C(124)–Si(126)	84.8(26)	87.3	87.2	85.7
ϕF(139)–Si(126)–C(124)–Si(125)	−41.9(17)	−42.2	−41.3	−41.3
ϕF(178)–Si(166)–C(165)–Si(167)	77.9(63)	73.4	79.3	77.3
ϕF(180)–Si(167)–C(165)–Si(166)	73.4(14)	74.0	72.9	73.4
ϕF(219)–Si(207)–C(206)–Si(208)	81.5(19)	80.5	82.5	81.7
ϕF(221)–Si(208)–C(206)–Si(207)	−170.6(23)	−170.1	−171.1	−170.7
ϕF(220)–Si(209)–C(206)–Si(207)	80.3(7)	81.1	80.4	80.3
ϕF(222)–Si(210)–C(206)–Si(207)	−36.7(23)	−38.7	−36.3	−36.8
ϕF(260)–Si(248)–C(247)–Si(249)	80.5(24)	78.1	80.5	80.6
ϕF(262)–Si(249)–C(247)–Si(248)	−161.8(20)	−161.5	−161.5	−161.7
ϕF(261)–Si(250)–C(247)–Si(248)	−157.6(25)	−157.4	−156.7	−157.5
ϕF(263)–Si(251)–C(247)–Si(248)	71.4(38)	71.5	71.6	71.4

[a] Distances (r) are in pm, angles (∠) and dihedral angles (ϕ) are in degrees. Atom numbering is given in Fig. 1. r_e values were calculated using the aug-cc-pVDZ basis set for each respective theory. The estimated standard deviations shown in parentheses represent 1σ.

Table 4. Selected experimental (r_{h1}) and quantum-chemically calculated (r_e) geometric parameters for **3**[a].

Parameter	r_{h1}	r_e B3LYP	r_e M06-2X	r_e MP2
rC(1)–Si(2)	192.0(4)	194.1	191.1	191.9
rSi(2)–C(12)	189.1(4)	188.0	186.9	187.9
rSi(2)–Cl(14)	209.1(2)	215.5	213.8	214.4
∠Si(2)–C(1)–Si(3)	110.3(4)	109.4	109.6	109.6
∠C(1)–Si(2)–C(12)	115.3(4)	116.8	116.7	116.4
∠C(1)–Si(2)–C(13)	113.8(4)	115.2	114.5	114.8
∠C(1)–Si(2)–Cl(14)	107.4(5)	107.6	106.8	106.2
∠C(10)–Si(4)–C(11)	107.0(20)	108.4	109.3	109.1
∠C(10)–Si(4)–Cl(15)	107.0(8)	104.1	104.6	104.7
ϕCl(14)–Si(2)–C(1)–Si(3)	39.9(4)	40.2	40.1	40.2
ϕCl(16)–Si(3)–C(1)–Si(2)	159.1(5)	159.2	159.3	159.4
ϕCl(15)–Si(4)–C(1)–Si(2)	−74.9(11)	−73.3	−73.1	−73.5
ϕCl(17)–Si(5)–C(1)–Si(2)	34.7(5)	35.9	35.8	35.8
ϕCl(56)–Si(45)–C(42)–Si(46)	−75.3(6)	−75.0	−74.7	−75.1
ϕCl(58)–Si(46)–C(42)–Si(44)	165.2(7)	165.6	165.8	165.6

[a] Distances (r) are in pm, angles (∠) and dihedral angles (ϕ) are in degrees. Atom numbering is given in Fig. 1. r_e values were calculated using the aug-cc-pVDZ basis set for each respective theory. The estimated standard deviations shown in parentheses represent 1σ.

Table 5. Selected experimental (r_{h1}) and theoretical (r_e) geometric parameters for **4**[a].

Parameter	r_{h1}	r_e B3LYP	r_e M06-2X	r_e MP2
rC(1)–Si(2)	191.1(5)	194.9	191.9	192.2
rSi(2)–C(12)	186.2(3)	188.3	187.1	188.0
rSi(2)–Br(14)	227.6(1)	231.6	230.8	230.0
∠Si(2)–C(1)–Si(3)	108.4(2)	109.2	109.4	109.4
∠C(1)–Si(2)–C(12)	118.3(5)	116.4	116.7	116.8
∠C(1)–Si(2)–C(13)	116.4(5)	114.9	114.4	114.8
∠C(1)–Si(2)–Br(14)	107.6(3)	109.8	108.7	107.2
∠C(10)–Si(4)–C(11)	109.0(10)	108.3	109.2	109.1
∠C(10)–Si(4)–Br(15)	102.2(3)	103.5	104.0	104.1
ϕBr(14)–Si(2)–C(1)–Si(3)	39.6(8)	40.4	40.2	39.5
ϕBr(16)–Si(3)–C(1)–Si(2)	158.7(6)	159.2	159.3	158.7
ϕBr(15)–Si(4)–C(1)–Si(2)	−72.7(11)	−73.3	−72.6	−72.9
ϕBr(17)–Si(5)–C(1)–Si(2)	35.0(14)	36.4	35.6	34.8
ϕBr(55)–Si(43)–C(42)–Si(45)	−80.6(11)	−80.5	−81.3	−81.2
ϕBr(56)–Si(45)–C(42)–Si(43)	166.4(8)	166.3	166.4	166.3

[a] Distances (r) are in pm, angles (∠) and dihedral angles (ϕ) are in degrees. Atom numbering is given in Fig. 1. r_e values were calculated using the aug-cc-pVDZ(-PP) basis set for each respective theory. The estimated standard deviations shown in parentheses represent 1σ.

(restrictions in available computational time made this necessary). This is further justified below.

For species **2**–**4** the increasing size of the halogen atom leads to the basis sets being used becoming insufficient for full descriptions. Table 6 shows the change in Si–Cl bond length upon moving from the aug-cc-pVDZ through to the aug-cc-pV5Z basis set when calculating the structure of the much simpler H$_3$SiCl molecule. In order to achieve this set of calculations the level of theory used was also limited to HF. These calculations show clearly that lack of basis set convergence must be at least part of the cause of the deviations between experiment and theory described earlier.

Studies of similar compounds {(Me$_2$HSi)$_3$CSiH$_3$ [34] and (Me$_3$Si)$_3$CSiCl$_3$ [35]} have been carried out using GED, and comparisons can be drawn with the structures presented in this paper. All four species from this work, plus the two literature studies, have Si–C bonds in common. The C(1)–Si(2/3/4/5) bonds present in species **1**–**4** increase in length when the size of atom X increases.

The GED structure of **1** can be directly compared with the structure of (Me$_2$HSi)$_3$CSiH$_3$, for

Table 6. Comparison of Si–Cl bond lengths in H$_3$SiCl calculated using HF theory with increasing basis set size[a].

Parameter	aug-cc-pVDZ	aug-cc-pVTZ	aug-cc-pVQZ	aug-cc-pV5Z
rSi–Cl	209.6	206.9	206.3	205.9

[a] Distances (r) are in pm.

which eleven conformers were modelled for the refinement [34]. Both contain Me$_2$HSi groups, although (Me$_2$HSi)$_3$CSiH$_3$ has two distinct types of central C–Si distances (those to the Me$_2$HSi groups, and that to SiH$_3$), with these distances having values of approximately 190 and 188 pm, respectively. Unsurprisingly, the C(1)–Si(2) distance for **1** [189.4(4) pm] agrees well with those determined for the Me$_2$HSi groups in (Me$_2$HSi)$_3$CSiH$_3$ [34]. In that species the angles between two silicon atoms connected through the central carbon take values between 108.1 and 111.7° depending on the orientation of the arms. For **1** the comparable angle [Si(2)–C(1)–Si(3)] is at the lower end of this range (108.3°) as the lack of a smaller SiH$_3$ substituent in **1** precludes the larger angles for steric reasons.

Molecule **3** from this study can be compared with (Me$_3$Si)$_3$CSiCl$_3$ in the literature [35], as both display chlorinated substituents, albeit in different environments. Despite similarities between the Me$_3$Si substituents in that species and Me$_2$ClSi in **3**, the lack of the halogen atoms bonded directly to the central carbon atom does alter the chemical environment. The central C–Si distance to the SiCl$_3$ substituent in (Me$_3$Si)$_3$CSiCl$_3$ is 189.1(8) pm, while the central C–Si distance in **3** is very similar at 189.1(4) pm. In (Me$_3$Si)$_3$CSiCl$_3$ both the central C–Si distance for the trimethylsilyl arms, 191.4(8) pm, and the Si–C distance to the methyl groups, 187.8(6) pm, are shorter than their comparable bonds in **3**, at 192.0(4) and 189.1(4) pm, respectively. This can be explained by the

lack of electron-withdrawing halogen atoms, which act to weaken the other bonds to silicon. The Si–Cl distance in the SiCl$_3$ group is also shorter than that in the Me$_2$ClSi group in **3** by almost 6 pm. This is presumably due to the accumulative electron-withdrawing effect of three chlorine atoms drawing more electron density towards themselves.

Within the molecules studied here a noticeable difference can be found when contrasting the central C–Si distances with the silicon-to-methyl carbon distances. The electron-withdrawing nature of the halogen atoms in **2**–**4** cause disparity between these distances within the molecule, with the largest difference found in the Br derivative. This compares favourably with the study of (XMe$_2$Si)$_2$C(SiMe$_3$)$_2$ (X = H, Cl, Br) [36], where the central C–Si distance is consistently longer than that of the methyl carbon to the silicon distance when X = Cl, Br.

Solution-phase dynamic structures

The ^{1}H NMR spectrum of C(SiBrMe$_2$)$_4$ (**4**) shows, as would be expected, a single broad resonance at room temperature (see Fig. S9 in the Supporting Information). However, on lowering the temperature a much more complicated spectrum emerges (Fig. S9), and at 213 K the spectrum (see Fig. 4) is consistent with

the presence of two different conformers. Four smaller peaks (α, β, γ, and δ) may be assigned to a C_2 conformer, and the eight larger peaks (A–H) are commensurate with the eight different methyl-group proton environments associated with a C_1-symmetric conformer. Integration of all signals leads to the conclusion that the C_1 conformer is the most abundant and makes up *ca.* 85 % of the conformer mixture, while the C_2 conformer gives rise to the remaining 15 % of the conformer mixture. Similarly, the ^{29}Si{^{1}H} NMR spectrum is a singlet at room temperature but at low temperature the spectrum (see Fig. 4) shows two smaller signals (1 and 2) associated with the C_2 conformer ^{1}H signals, and four larger signals (I–IV) associated with the C_1-symmetric conformer. Full details of the multinuclear NMR studies of the C(SiXMe$_2$)$_4$ (X = H, Cl, Br, I) compounds are provided in the Supporting Information.

The ^{1}H and ^{29}Si{^{1}H} NMR spectra for C(SiClMe$_2$)$_4$ (**3**), show similar, though less well resolved, features to the spectra for the analogous bromide (**4**). Again, sharp singlets at room temperature give rise to much more complicated spectra at low temperature (see Fig. S5) that are consistent with the presence of a less abundant C_2 and a more abundant C_1 conformer, as shown in Fig. 5. The conformers are labelled as for Fig. 4.
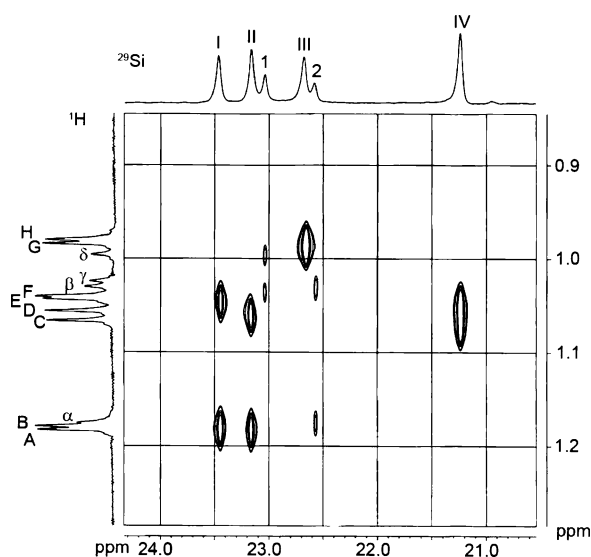

Fig. 4. 2D ^{1}H/^{29}Si NMR correlation spectrum of C(SiBr-Me$_2$)$_4$ (**4**) in CDCl$_3$/CD$_2$Cl$_2$ at 213 K. The labelling scheme is explained in detail in the Supporting Information.
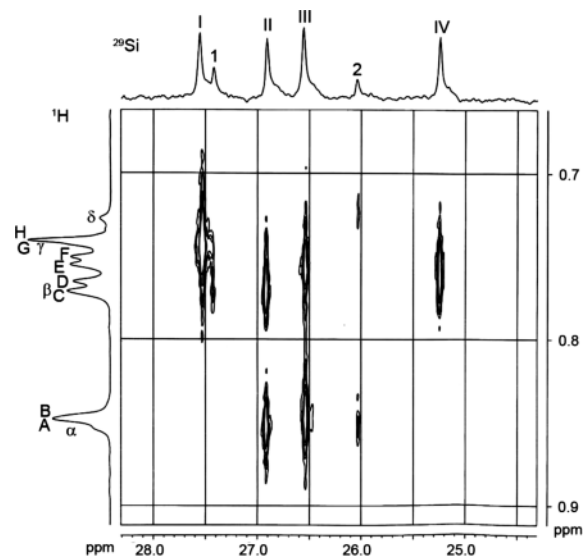

Fig. 5. 2D ^{1}H/^{29}Si NMR shift correlation spectrum of C(SiClMe$_2$)$_4$ (**3**) in CDCl$_3$/CD$_2$Cl$_2$ at 201 K. The labelling scheme is explained in detail in the Supporting Information.
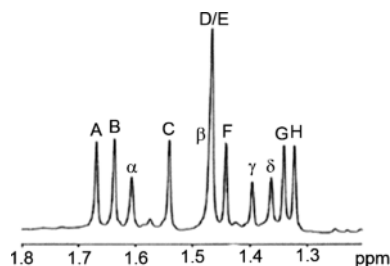
Fig. 6. 360 MHz ^{1}H NMR spectrum of C(SiIMe$_2$)$_4$ (**5**) at 223 K. The labelling scheme is explained in detail in the Supporting Information.

The NMR studies agree well with the single-molecule *ab initio* calculations showing the two lowest energy conformations possessing C_1 and C_2 symmetry, with the relative proportions of the two conformers at the temperature of experiment being *ca.* 82 and 18 % for the C_1 and C_2 conformer, respectively. Such proportions were also used to fit the GED data and, despite GED being performed in the gas phase rather than in solution, the similarities in relative abundances are not unexpected.

Although it was not possible to determine the gas-phase structure of C(SiIMe$_2$)$_4$ (**5**), the solution ^{1}H NMR spectrum has been investigated. The ^{1}H NMR spectrum for **5** shows a broad signal at room temperature which, on lowering the temperature, rapidly splits into twelve signals as shown in Fig. 6. This spectrum shows two sets of peaks (A–H) and (α–δ), as did the spectra for the analogous chlorine and bromine compounds, and it is thus reasonable to assume that similar C_1 and C_2 conformers are present for the iodide as well. Further details of the NMR spectra including saturation transfer experiments are given in the Supporting Information (Figs. S13 and S14).

The ^{1}H and ^{29}Si NMR spectra of the much less bulky C(SiHMe$_2$)$_4$ showed no significant changes when recorded over the range of 333 to 213 K, and no evidence for restricted rotation or the presence of different conformers was observed. For details see the Supporting Information.

Supporting information

Additional details relating to the GED experiments (Table S1); energies relating to all calculated conformers for each species (Tables S2–4); details from the GED models and refinements (Tables S5–8), amplitudes of vibration and curvilinear distance corrections (Tables S9–12); least-squares correlation matrices (Tables S13–16); final GED co-ordinates (Tables S17–20); calculated coordinates and energies (Tables S21–24); plots of molecular-scattering intensity curves and corresponding radial distribution curves (Figs. S1–4); details of NMR spectroscopic studies (Tables S25–27; Figs. S5–16). This material (337 pages) is available online: DOI: 10.5560/ZNB.2014-4147.

[1] C. Eaborn, *J. Chem. Soc., Dalton Trans.* **2001**, 3397.

[2] C. Eaborn, J. D. Smith, *J. Chem. Soc., Dalton Trans.* **2001**, 1541.

[3] P. D. Lickiss in *Comprehensive Organic Functional Group Transformations*, Vol. 6, (Eds.: A. R. Katritzky, O. Meth-Cohn, C. W. Rees), Pergamon, Oxford, **1995**, p. 377.

[4] P. D. Lickiss in *Comprehensive Organic Functional Group Transformations II*, Vol. 6, (Eds.: A. R. Katritzky, R. J. K. Taylor), Elsevier, Oxford, **2005**, p. 381.

[5] R. L. Merker, M. J. Scott, *J. Org. Chem.* **1964**, *29*, 953.

[6] C. Eaborn, P. D. Lickiss, *J. Organomet. Chem.* **1985**, *294*, 305.

[7] A. Kowalewska, P. D. Lickiss, R. Lucas, W. A. Stańczyk, *J. Organomet. Chem.* **2000**, *597*, 111.

[8] P. Kulpinski, P. D. Lickiss, W. A. Stańczyk, *Bull. Pol. Acad. Sci. Chem.* **1992**, *40*, 21.

[9] S.-L. Liu, M.-M. Ma, *J. Organomet. Chem.* **1970**, *24*, 89.

[10] C. Eaborn, A. I. Mansour, *J. Chem. Soc., Perkin Trans. 2* **1985**, 729.

[11] A. I. Al-Mansour, S. S. Al-Showiman, I. M. Al-Najjar, *Inorg. Chim. Acta* **1987**, *134*, 275.

[12] C. Eaborn, P. B. Hitchcock, P. D. Lickiss, *J. Organomet. Chem.* **1984**, *264*, 119.

[13] S. S. Al-Juaid, C. Eaborn, P. B. Hitchcock, P. D. Lickiss, *J. Organomet. Chem.* **1988**, *353*, 297.

[14] R. L. Merker, M. J. Scott, *J. Org. Chem.* **1963**, *28*, 2717.

[15] A. Kowalewska, W. A. Stańczyk, R. Eckberg, *Appl. Catal. A* **2005**, *287*, 54.

[16] M. Ishikawa, M. Kumada, H. Sakurai, *J. Organomet. Chem.* **1970**, *23*, 63.

[17] H. Sakurai, T. Watanabe, M. Kumada, *J. Organomet. Chem.* **1967**, *9*, 11.

[18] X. J. Helluy, J. Kümmerlen, A. Sebald, *Organometallics* **1998**, *17*, 5003.

[19] A. E. Aliev, K. D. M. Harris, D. C. Apperley, R. K. Harris, *J. Solid State Chem.* **1994**, *110*, 314.

[20] A. E. Aliev, K. D. M. Harris, *Mendeleev Commun.* **1993**, 153.

[21] B. Wrackmeyer, H. Zhou, *Spectrochim. Acta A* **1991**, *47*, 849.

[22] J. M. Dereppe, J. H. Magill, *J. Phys. Chem.* **1972**, *76*, 4037.

[23] H. W. Lerner, M. Bolte, *Acta Crystallogr. E* **2005**, *61*, o2326.

[24] R. E. Dinnebier, S. Carlson, S. van Smaalen, *Acta Crystallogr. B* **2000**, *56*, 310.

[25] R. E. Dinnebier, W. A. Dollase, X. Helluy, J. Kümmerlen, A. Sebald, M. U. Schmidt, S. Pagola, P. W. Stephens, S. van Smaalen, *Acta Crystallogr. B* **1999**, *55*, 1014.

[26] B. Beagley, R. G. Pritchard, J. O. Titiloye, *J. Mol. Struct.* **1989**, *212*, 323.

[27] B. Beagley, R. G. Pritchard, J. O. Titiloye, *J. Mol. Struct.* **1988**, *176*, 81.

[28] D. Iroff, K. Mislow, *J. Am. Chem. Soc.* **1978**, *100*, 2121.

[29] H. Bürger, U. Goetze, W. Sawodny, *Spectrochim. Acta A* **1970**, *26*, 685.

[30] C. Eaborn, P. B. Hitchcock, P. D. Lickiss, A. Pidcock, K. D. Safa, *J. Chem. Soc., Dalton Trans.* **1984**, 2015.

[31] A. G. Avent, P. D. Lickiss, A. Pidcock, *J. Organomet. Chem.* **1988**, *341*, 281.

[32] A. G. Avent, S. G. Bott, J. A. Ladd, P. D. Lickiss, A. Pidcock, *J. Organomet. Chem.* **1992**, *427*, 9.

[33] S. L. Masters, D. W. H. Rankin, D. B. Cordes, K. Bätz, P. D. Lickiss, N. M. Boag, A. D. Redhouse, S. M. Whittaker, *Dalton Trans.* **2010**, *39*, 9353.

[34] C. A. Morrison, D. W. H. Rankin, H. E. Robertson, P. D. Lickiss, P. C. Masangane, *J. Chem. Soc., Dalton Trans.* **1999**, 2293.

[35] D. G. Anderson, D. W. H. Rankin, H. E. Robertson, A. H. Cowley, M. Pakulski, *J. Mol. Struct.* **1989**, *196*, 21.

[36] D. A. Wann, M. S. Robinson, K. Bätz, S. L. Masters, A. G. Avent, P. D. Lickiss, manuscript in preparation.

[37] M. J. Frisch, G. W. Trucks, H. B. Schlegel, G. E. Scuseria, M. A. Robb, J. R. Cheeseman, G. Scalmani, V. Barone, B. Mennucci, G. A. Petersson, H. Nakatsuji, M. Caricato, X. Li, H. P. Hratchian, A. F. Izmaylov, J. Bloino, G. Zheng, J. L. Sonnenberg, M. Hada, M. Ehara, K. Toyota, R. Fukuda, J. Hasegawa, M. Ishida, T. Nakajima, Y. Honda, O. Kitao, H. Nakai, T. Vreven, J. A. Montgomery, Jr., J. E. Peralta, F. Ogliaro, M. Bearpark, J. J. Heyd, E. Brothers, K. N. Kudin, V. N. Staroverov, R. Kobayashi, J. Normand, K. Raghavachari, A. Rendell, J. C. Burant, S. S. Iyengar, J. Tomasi, M. Cossi, N. Rega, J. M. Millam, M. Klene, J. E. Knox, J. B. Cross, V. Bakken, C. Adamo, J. Jaramillo, R. Gomperts, R. E. Stratmann, O. Yazyev, A. J. Austin, R. Cammi, C. Pomelli, J. W. Ochterski, R. L. Martin, K. Morokuma, V. G. Zakrzewski, G. A. Voth, P. Salvador, J. J. Dannenberg, S. Dapprich, A. D. Daniels, Ö. Farkas, J. B. Foresman, J. V. Ortiz, J. Cioslowski, D. J. Fox, GAUSSIAN 09 (revision A.1), Gaussian, Inc., Wallingford CT (USA) **2009**.

[38] Edinburgh Compute and Data Facility (ECDF); http://www.ecdf.ed.ac.uk/.

[39] EPSRC-funded NSCCS; http://www.nsccs.ac.uk/.

[40] A. Becke, *J. Chem. Phys.* **1993**, *98*, 5648.

[41] C. Lee, W. Yang, R. Parr, *Phys. Rev. B* **1988**, *37*, 785.

[42] B. Miehlich, A. Savin, H. Stoll, H. Preuss, *Chem. Phys. Lett.* **1989**, *157*, 200.

[43] Y. Zhao, D. G. Truhlar, *Theor. Chem. Acc.* **2008**, *120*, 215.

[44] J. Binkley, J. A. Pople, W. J. Hehre, *J. Am. Chem. Soc.* **1980**, *102*, 939.

[45] M. Gordon, J. Binkley, J. A. Pople, W. J. Pietro, W. J. Hehre, *J. Am. Chem. Soc.* **1982**, *104*, 2797.

[46] R. Kendall, T. H. Dunning, R. Harrison, *J. Chem. Phys.* **1992**, *96*, 6796.

[47] A. Wilson, T. van Mourik, T. H. Dunning, *J. Mol. Struct.* **1996**, *388*, 339.

[48] D. E. Woon, T. H. Dunning, *J. Chem. Phys.* **1993**, *98*, 1358.

[49] K. A. Peterson, D. Figgen, E. Goll, H. Stoll, M. Dolg, *J. Chem. Phys.* **2003**, *119*, 11113.

[50] C. Møller, M. Plesset, *Phys. Rev.* **1934**, *46*, 618.

[51] V. A. Sipachev, *J. Mol. Struct. (THEOCHEM)* **1985**, *121*, 143.

[52] V. A. Sipachev, *J. Mol. Struct.* **2001**, *567*, 67.

[53] C. M. Huntley, G. S. Laurenson, D. W. H. Rankin, *J. Chem. Soc., Dalton Trans.* **1980**, 954.

[54] H. Fleischer, D. A. Wann, S. L. Hinchley, K. B. Borisenko, J. R. Lewis, R. J. Mawhorter, H. E. Robertson, D. W. H. Rankin, *Dalton Trans.* **2005**, 3221.

[55] S. L. Hinchley, H. E. Robertson, K. B. Borisenko, A. R. Turner, B. F. Johnston, D. W. H. Rankin, M. Ahmadian, J. N. Jones, A. H. Cowley, *Dalton Trans.* **2004**, 2469.

[56] A. W. Ross, M. Fink, R. Hilderbrand in *International Tables for Crystallography*, Vol. C, (Ed.: A. J. C. Wilson), Kluwer Academic Publishers, Dordrecht, **1992**, p. 245.

[57] P. D. Lickiss, D. Phil. Thesis, University of Sussex, Falmer, Brighton, **1983**.

[58] N. W. Mitzel, B. A. Smart, A. J. Blake, H. E. Robertson, D. W. H. Rankin, *J. Phys. Chem.* **1996**, *100*, 9339.

[59] A. J. Blake, P. T. Brain, H. McNab, J. Miller, C. A. Morrison, S. Parsons, D. W. H. Rankin, H. E. Robertson, B. A. Smart, *J. Phys Chem.* **1996**, *100*, 12280.

[60] N. W. Mitzel, D. W. H. Rankin, *Dalton Trans.* **2003**, 3650.

[61] W. C. Hamilton, *Acta Crystallogr.* **1965**, *18*, 502.

[62] S. L. Masters, S. J. Atkinson, M. Hölbling, K. Hassler, *Struct. Chem.* **2013**, *24*, 1201.

Abbreviations

ALT	Andersen-Lowe Thermostat
AO	Atomic Orbital
AT	Andersen Thermostat
B3LYP	Becke, 3-parameter, Lee-Yang-Parr
CASSCF	Complete Active Space Self Consistent Field
CC	Coupled Cluster
CCD	Charge-Coupled Device
CPMD	Car-Parrinello Molecular Dynamics
DFT	Density Functional Theory
DZ/TZ/QZ/5Z	Double Zeta/Triple Zeta/Quadruple Zeta/Quintuple Zeta basis set sizes
ECP	Effective Core Potential
ED	Electron Diffraction
EDSTRACT	Custom extraction software written for and used in this work
FWHM	Full Width at Half Maximum
GED	Gas Electron Diffraction
GGA	Generalised Gradient Approximation
HF	Hartree-Fock theory

ICT	Intermolecular Charge Transfer
LANL2DZ	Los Alamos National Laboratory 2-Double-Zeta
LDA	Local Density Approximation
MD	Molecular Dynamics
MIC	Molecular Intensity Curve
MO	Molecular Orbital
MOCED	Molecular Orbital Constrained Electron Diffraction
MP	Møller-Plesset perturbation theory
MP2/3/4	2nd/3rd/4th order Møller-Plesset perturbation series
NCI	Noncovalent interactions
NMR	Nuclear Magnetic Resonance
PID	Proportional-Integral-Derivative (controller)
PIMD	Path Integral Molecular Dynamics
RDC	Radial Distribution Curve
RF	Radio Frequency
SARACEN	Structural Analysis Restrained by *ab initio* Calculations for ElectroN diffraction
SE	Schrödinger Equation
SS	Stainless Steel
STRADIVARIUS	STructure Analysis using DIffraction and VARIoUS other data
TD-DFT	Time-Dependent Density Functional Theory

TRED	Time-Resolved Electron Diffraction
UED	Ultrafast Electron Diffraction
xpkg	Extraction software used for data collected using the former Edinburgh ED apparatus
$\angle$	Symbol for angle
R_D	Goodness-of-fit (ignoring correlation between parameters)
R_G	Goodness-of-fit (including correlation between parameters)
r_e	True equilibrium distance
r_a	Raw distance from GED data
r_g	GED distance including vibrational averaged correction
r_{h0}	GED distance with perpendicular corrections from ASYM
r_{h1}	GED distance with perpendicular corrections from SHRINK
$r_{a3,1}$	GED distance including perpendicular corrections calculated from the third derivative of the energy, used to account for anharmonicity

References

[1] J. Yoo, E. K. Brechin, A. Yamaguchi, M. Nakano, J. C. Huffman, A. L. Maniero, L. C. Brunel, K. Awaga, H. Ishimoto, G. Christou and D. N. Hendrickson, *Inorg. Chem.*, 2000, **39**, 3615–3623.

[2] I. Hargittai, in *Stereochemical Applications of Gas-Phase Electron Diffraction. Part A*, ed. I. Hargittai and M. Hargittai, VCH Publishers, Inc., 1988, pp. XV–XVIII.

[3] T. Young, *Philosophical Transactions of the Royal Society of London*, 1802, **92**, 12–48.

[4] L. de Broglie, *C. R. Hebd. Acad. Sci.*, 1922, **175**, 811–813.

[5] C. Davisson and L. H. Germer, *Phys. Rev.*, 1927, **30**, 705–741.

[6] W. H. Bragg and W. L. Bragg, *Proc. R. Soc. Lond. A*, 1913, **88**, 428–438.

[7] P. Debye, *Ann. Phys.*, 1915, **46**, 809–823.

[8] H. Mark and R. Wierl, *Naturwissenschaften*, 1928, **95**, 778–786.

[9] H. Fleischer, D. A. Wann, S. L. Hinchley, K. B. Borisenko, J. R. Lewis, R. J. Mawhorter, H. E. Robertson and D. W. H. Rankin, *Dalton Trans.*, 2005, 3221–3228.

[10] L. Pauling and L. O. Brockway, *J. Chem. Phys.*, 1934, **2**, 867–881.

[11] S. A. Hayes, *Ph.D. thesis*, The University of Edinburgh, 2008.

[12] C. Finbak, *Avhandl. Nor. Videnskaps-Akad. Oslo, I, Mat.-Naturv. Klasse*, 1937.

[13] P. Debye, *Phys. Z.*, 1939, **40**, 404.

[14] L. O. Brockway and L. S. Bartell, *Rev. Sci. Instrum.*, 1954, **25**, 569–575.

[15] J. Karle and I. L. Karle, *J. Chem. Phys.*, 1947, **15**, 764–765.

[16] S. A. Hayes, R. J. F. Berger, B. Neumann, N. W. Mitzel, J. Bader and B. Hoge, *Dalton Trans.*, 2010, **39**, 5630–5636.

[17] D. A. Wann, R. J. Less, F. Rataboul, P. D. McCaffrey, A. M. Reilly, H. E. Robertson, P. D. Lickiss and D. W. H. Rankin, *Organometallics*, 2008, **27**, 4183–4187.

[18] J. D. Ewbank, L. Schäfer, D. W. Paul, O. J. Benston and J. C. Lennox, *Rev. Sci. Instrum.*, 1984, **55**, 1598–1603.

[19] K. Laqua, B. Schrader, D. S. Moore and T. Vo-Dinh, in *Detect. Radiat.*, IUPAC recommendations, 1995.

[20] P. A. Shaffer, V. Schomaker and L. Pauling, *J. Chem. Phys.*, 1946, **14**, 659–664.

[21] J. Karle and I. L. Karle, *J. Chem. Phys.*, 1950, **18**, 957–962.

[22] R. A. Bonham and L. S. Bartell, *J. Chem. Phys.*, 1959, **31**, 702–708.

[23] L. S. Bartell, D. A. Kohl, B. L. Carroll and R. M. Gavin Jr., *J. Chem. Phys.*, 1965, **42**, 3079–3084.

[24] V. J. Klimkowski, J. D. Ewbank, C. van Alsenoy, J. N. Scarsdale and L. Schäfer, *J. Am. Chem. Soc.*, 1982, **104**, 1476–1480.

[25] N. W. Mitzel and D. W. H. Rankin, *Dalton Trans.*, 2003, 3650–3662.

[26] D. A. Wann, S. Young, K. Bätz, S. L. Masters, A. G. Avent, D. W. H. Rankin and P. D. Lickiss, *Z. Naturforsch. B*, 2014, **69**, 1321–1332.

[27] Y. V. Vishnevskiy, *J. Mol. Struct.*, 2007, **871**, 24–32.

[28] H. M. Seip, in *Molecular Structure by Diffraction Methods*, ed. G. A. Sim and L. E. Sutton, The Chemical Society, 1973, vol. 1, ch. 1, pp. 7–58.

[29] P. D. McCaffrey, *Ph.D. thesis*, The University of Edinburgh, 2007.

[30] L. S. Bartell, in *Stereochemical Applications of Gas-Phase Electron Diffraction. Part A*, ed. I. Hargittai and M. Hargittai, VCH Publishers, Inc., 1988, pp. 55–83.

[31] V. Schomaker and R. Glauber, *Nature*, 1952, **170**, 290–291.

[32] K. Kuchitsu and L. S. Bartell, *J. Chem. Phys.*, 1961, **35**, 1945–1949.

[33] B. Andersen, H. M. Seip, T. G. Strand and R. Stølevnik, *Acta Chem. Scand.*, 1969, **23**, 3224–3234.

[34] S. L. Hinchley, H. E. Robertson, K. B. Borisenko, A. R. Turner, B. F. Johnston, D. W. H. Rankin, M. Ahmadian, J. N. Jones and A. H. Cowley, *Dalton Trans.*, 2004, 2469–2476.

[35] D. A. Wann, F. Blockhuys, C. van Alsenoy, H. E. Robertson, H.-J. Himmel, C. Y. Tang, A. R. Cowley, A. J. Downs and D. W. H. Rankin, *Dalton Trans.*, 2007, 1687–1696.

[36] E. M. Brown, P. D. McCaffrey, D. A. Wann and D. W. H. Rankin, *Phys. Chem. Chem. Phys.*, 2008, **10**, 738–742.

[37] P. B. Liescheski and D. W. H. Rankin, *J. Mol. Struct.*, 1989, **196**, 1–19.

[38] E. Schrödinger, *Phys. Rev.*, 1926, **28**, 1049–1070.

[39] F. Jensen, *Introduction to Computational Chemistry*, John Wiley & Sons, Ltd., Chichester, U.K., 2nd edn., 2007.

[40] R. H. A. Eade and M. A. Robb, *Chem. Phys. Lett.*, 1981, **83**, 362–368.

[41] C. Møller and M. Plesset, *Phys. Rev.*, 1934, **46**, 618–622.

[42] M. Head-Gordon, J. A. Pople and M. J. Frisch, *Chem. Phys. Lett.*, 1988, **153**, 503–506.

[43] J. A. Pople, R. Seeger and R. Krishnan, *Int. J. Quantum Chem.*, 1977, **11**, 149–163.

[44] R. Krishnan and J. A. Pople, *Int. J. Quantum Chem.*, 1978, **14**, 91–100.

[45] R. Ditchfield, W. J. Hehre and J. A. Pople, *J. Chem. Phys.*, 1971, **54**, 724–728.

[46] V. A. Rassolov, M. A. Ratner, J. A. Pople, P. C. Redfern and L. A. Curtiss, *J. Comput. Chem.*, 2001, **22**, 976–984.

[47] R. Krishnan, J. S. Binkley, R. Seeger and J. A. Pople, *J. Chem. Phys.*, 1980, **72**, 650–654.

[48] A. D. McLean and G. S. Chandler, *J. Chem. Phys.*, 1980, **72**, 5639–5648.

[49] T. H. Dunning Jr., *J. Chem. Phys.*, 1989, **90**, 1007–1023.

[50] R. A. Kendall, T. H. Dunning Jr. and R. J. Harrison, *J. Chem. Phys.*, 1992, **96**, 6796–6806.

[51] D. E. Woon and T. H. Dunning Jr., *J. Chem. Phys.*, 1993, **98**, 1358–1371.

[52] K. A. Peterson, D. E. Woon and T. H. Dunning Jr., *J. Chem. Phys.*, 1994, **100**, 7410–7415.

[53] W. Kohn and L. J. Sham, *Phys. Rev.*, 1965, **140**, A1133–A1138.

[54] D. C. Langreth and M. J. Mehl, *Phys. Rev. B*, 1983, **28**, 1809–1834.

[55] J. Perdew, J. Chevary, S. Vosko, K. Jackson, M. Pederson, D. Singh and C. Fiolhais, *Phys. Rev. B*, 1993, **48**, 4978–4978.

[56] E. Runge and E. K. U. Gross, *Phys. Rev. Lett.*, 1984, **52**, 997–1000.

[57] A. D. Becke, *J. Chem. Phys.*, 1993, **98**, 5648–5652.

[58] C. Lee, W. Yang and R. G. Parr, *Phys. Rev. B*, 1988, **37**, 785–789.

[59] B. Miehlich, A. Savin, H. Stoll and H. Preuss, *Chem. Phys. Lett.*, 1989, **157**, 200–206.

[60] B. J. Alder and T. E. Wainwright, *J. Chem. Phys.*, 1959, **31**, 459–466.

[61] M. J. Frisch, G. W. Trucks, H. B. Schlegel, G. E. Scuseria, M. A. Robb, J. R. Cheeseman, G. Scalmani, V. Barone, B. Mennucci, G. A. Petersson, H. Nakatsuji, M. Caricato, X. Li, H. P. Hratchian, A. F. Izmaylov, J. Bloino, G. Zheng, J. L. Sonnenberg, M. Hada, M. Ehara, K. Toyota, R. Fukuda, J. Hasegawa, M. Ishida, T. Nakajima, Y. Honda, O. Kitao, H. Nakai, T. Vreven, J. A. Montgomery, Jr., J. E. Peralta, F. Ogliaro, M. Bearpark, J. J. Heyd, E. Brothers, K. N. Kudin, V. N. Staroverov, R. Kobayashi, J. Normand, K. Raghavachari, A. Rendell, J. C. Burant, S. S. Iyengar, J. Tomasi, M. Cossi, N. Rega, J. M. Millam, M. Klene, J. E. Knox, J. B. Cross, V. Bakken, C. Adamo, J. Jaramillo, R. Gomperts, R. E. Stratmann, O. Yazyev, A. J. Austin, R. Cammi, C. Pomelli, J. W. Ochterski, R. L. Martin, K. Morokuma, V. G. Zakrzewski, G. A. Voth, P. Salvador, J. J. Dannenberg, S. Dapprich, A. D. Daniels, . Farkas, J. B. Foresman, J. V. Ortiz, J. Cioslowski and D. J. Fox, *Gaussian 09 Revision D.01*, Gaussian Inc. Wallingford CT 2009.

[62] Y. Morino, S. J. Cyvin, K. Kuchitsu and T. Iijima, *J. Chem. Phys.*, 1962, **36**, 1109.

[63] O. Bastiansen and M. Trætteberg, *Acta Crystallogr.*, 1960, **13**, 1108.

[64] D. A. Wann, A. V. Zakharov, A. M. Reilly, P. D. McCaffrey and D. W. H. Rankin, *J. Phys. Chem. A*, 2009, **113**, 9511–9520.

[65] R. Campargue, *J. Phys. Chem.*, 1984, **88**, 4466–4474.

[66] G. Sciaini and R. J. D. Miller, *Rep. Prog. Phys.*, 2011, **74**, 1–36.

[67] M. S. Robinson, *Ph.D. thesis*, University of York, 2015.

[68] R. J. F. Berger, M. Hoffmann, S. A. Hayes and N. W. Mitzel, *Z. Naturforsch. B*, 2009, **64**, 1259–1268.

[69] C. M. Huntley, G. S. Laurenson and D. W. H. Rankin, *J. Chem. Soc., Dalton Trans.*, 1980, 954–957.

[70] S. L. Masters, G. V. Girichev and S. A. Shylkov, *Dalton Trans.*, 2013, **42**, 3581–3586.

[71] L. S. Khaikin, O. E. Grikina, A. V. Golubinskii and L. V. Vilkov, *Dokl. Phys. Chem.*, 2003, **390**, 791–795.

[72] B. Raoult, *Rev. Sci. Instrum.*, 1973, **44**, 430–434.

[73] G. D. Stein, *J. Chem. Phys.*, 1973, **58**, 1999.

[74] S. S. Kim and G. D. Stein, *Rev. Sci. Instrum.*, 1982, **53**, 838–844.

[75] M. Maier-Borst, D. Cameron, M. Rokni and J. Parks, *Phys. Rev. A*, 1999, **59**, R3162–R3165.

[76] D. Schooss, N. B. Blom, J. H. Parks, B. v. Issendorf, H. Haberland and M. M. Kappes, *Nano Lett.*, 2005, **5**, 1972–1977.

[77] M. N. Blom, D. Schooss, J. Stairs and M. M. Kappes, *J. Chem. Phys.*, 2006, **124**, 1–10.

[78] C. Hensley, J. Yang and M. Centurion, *Phys. Rev. Lett.*, 2012, **109**, 1–5.

[79] A. A. Ischenko, V. V. Golubkov, V. P. Spiridonov, A. V. Zgurskii, A. S. Akhmanov, M. G. Vabischevich and V. N. Bagratashvili, *Appl. Phys. B-Photo*, 1983, **32**, 161–163.

[80] J. D. Ewbank, W. L. Faust, J. Y. Luo, J. T. English, D. L. Monts, D. W. Paul, Q. Dou and L. Schäfer, *Rev. Sci. Instrum.*, 1992, **63**, 3352–3358.

[81] J. C. Williamson, M. Dantus, S. B. Kim and A. H. Zewail, *Chem. Phys. Lett.*, 1992, **196**, 529–534.

[82] T. S. Rose, M. J. Rosker and A. H. Zewail, *J. Chem. Phys.*, 1988, **88**, 6672–6673.

[83] J. R. Dwyer, C. T. Hebeisen, R. Ernstorfer, M. Harb, V. B. Deyirmenjian, R. E. Jordan and R. J. D. Miller, *Philos. Trans. A. Math. Phys. Eng. Sci.*, 2006, **364**, 741–778.

[84] J. C. Williamson and A. H. Zewail, *Proc. Nat. Acad. Sci.*, 1991, **88**, 5021–5025.

[85] J. C. Williamson, J. Cao, H. Ihee, H. Frey and A. H. Zewail, *Nature*, 1997, **386**, 159–162.

[86] J. C. Williamson and A. H. Zewail, *Chem. Phys. Lett.*, 1993, **209**, 10–16.

[87] R. Srinivasan, V. A. Lobastov, C.-Y. Ruan and A. H. Zewail, *Helv. Chim. Acta*, 2003, **86**, 1761–1799.

[88] R. S. Fender, *Ph.D. thesis*, The University of Edinburgh, 1996.

[89] P. Papathomas, *Ph.D. thesis*, The University of Edinburgh, 1998.

[90] R. A. Bonham and M. Fink, *High energy electron scattering*, Van Nostrand Reinhold, New York, NY, 1974.

[91] L. S. Bartell, R. K. Heenan and M. Nagashima, *J. Chem. Phys.*, 1983, **78**, 236–242.

[92] R. Campargue, *Rev. Sci. Instrum.*, 1964, **35**, 111.

[93] A. J. Downs, M. J. Goode, G. S. McGrady, I. A. Steer, D. W. H. Rankin and H. E. Robertson, *J. Chem. Soc., Dalton Trans.*, 1988, 451–456.

[94] C. E. Knapp, D. A. Wann, A. Bil, J. T. Schirlin, H. E. Robertson, P. F. McMillan, D. W. H. Rankin and C. J. Carmalt, *Inorg. Chem.*, 2012, **51**, 3324–3331.

[95] M. Hargittai, *Struct. Chem.*, 2005, **16**, 33–40.

[96] S. Hayes, *Discussion of extraction code adaptation*, Personal communication, 2013.

[97] A. Ross, M. Fink and R. Hilderbrandt, in *International Tables for Crystallography, Vol. C*, ed. A. J. C. Wilson, Kluwer Academic Publishers, Dordrecht, The Netherlands, 1992, p. 245.

[98] K. Uesugi, M. Hoshino and N. Yagi, *J. Synchrotron Radiat.*, 2011, **18**, 217–223.

[99] S. Gundersen, S. Samdal, T. G. Strand and H. V. Volden, *J. Mol. Struct.*, 2007, **832**, 164–171.

[100] J. de Vries, *LENSDISTORT*, 2012.

[101] V. Sipachev, *J. Mol. Struct. THEOCHEM*, 1985, **22**, 143–151.

[102] D. Marx and M. Parrinello, *J. Chem. Phys.*, 1996, **104**, 4077–4082.

[103] M. E. Tuckerman, D. Marx, M. L. Klein and M. Parrinello, *J. Chem. Phys.*, 1996, **104**, 5579.

[104] M. Barbatti, M. Ruckenbauer, F. Plasser, J. Pittner, G. Granucci, M. Persico and H. Lischka, *WIRES Comput. Mol. Sci.*, 2014, **4**, 26–33.

[105] M. Barbatti, J. Pittner, M. Pederzoli, U. Werner, R. Mitrić, V. Bonačić-Koutecký and H. Lischka, *Chem. Phys.*, 2010, **375**, 26–34.

[106] A. M. Reilly, *Ph.D. thesis*, The University of Edinburgh, 2009.

[107] H. C. Andersen, *J. Chem. Phys.*, 1980, **72**, 2384–2393.

[108] S. Nosé, *J. Chem. Phys.*, 1984, **81**, 511–516.

[109] W. G. Hoover, *Phys. Rev. A*, 1985, **31**, 1695–1697.

[110] D. Marx and J. Hutter, *Ab initio molecular dynamics: theory and implementation*, John von Neumann Institute for Computing, 2000, vol. 1, pp. 301–449.

[111] W. Andreoni and A. Curioni, *Parallel Comput.*, 2000, **26**, 819–842.

[112] E. A. Koopman and C. P. Lowe, *J. Chem. Phys.*, 2006, **124**, 1–5.

[113] C. P. Lowe, *Europhys. Lett.*, 2007, **47**, 145–151.

[114] S. D. Stoyanov and R. D. Groot, *J. Chem. Phys.*, 2005, **122**, 1–8.

[115] A. Gourdon, J. Launay and M. Bujoli-Doeuff, *J. Photochem. Photobiol. A*, 1993, **71**, 13–25.

[116] M. Park, C. H. Kim and T. Joo, *J. Phys. Chem. A*, 2013, **117**, 370–377.

[117] M. A. Kochman, A. Tajti, C. A. Morrison and R. J. D. Miller, *J. Chem. Theory Comput.*, 2015, **11**, 1118–1128.

[118] D. Rappoport and F. Furche, *J. Am. Chem. Soc.*, 2004, **126**, 1277–1284.

[119] R. Peverati and D. G. Truhlar, *Phys. Chem. Chem. Phys.*, 2012, **14**, 16187–16191.

[120] S. Grimme, *J. Chem. Phys.*, 2006, **124**, 1–16.

[121] A. Heine, R. Herbst-Irmer, D. Stalke, W. Kühnle and K. A. Zachariasse, *Acta Crystallogr. B*, 1994, **50**, 363–373.

[122] O. Kajimoto, H. Yokoyama, Y. Ooshima and Y. Endo, *Chem. Phys. Lett.*, 1991, **179**, 455–459.

[123] S. Grimme, *J. Comput. Chem.*, 2006, **27**, 1787–1799.

[124] M. S. Robinson, *Discussion of phosphor use in TRED experiments*, Personal communication, 2013.

[125] M. S. Gordon and M. W. Schmidt, *Theory and Applications of Computational Chemistry*, Elsevier, 2005, pp. 1167–1189.

[126] M. Schmidt, K. K. Baldridge, J. A. Boatz, S. T. Elbert, M. S. Gordon, J. H. Jensen, S. Koseki, N. Matsunaga, K. A. Nguyen, S. Su, T. L. Windus, M. Dupuis and J. A. Montgomery Jr., *J. Comput. Chem.*, 1993, **14**, 1347–1363.

[127] D. S. Tikhonov, *Molecular dynamics simulation using GAMESS US*, Personal communication, 2015.

[128] C. Kitchen, *M.Chem. project report*, The University of Edinburgh, 2008.

[129] P. A. Madden and M. Wilson, *Chem. Soc. Rev.*, 1996, **25**, 339–350.